Diffraction Analysis with UWB Validation for ToA Ranging in the Proximity of Human Body and Metallic Objects

A Dissertation Submitted to the Faculty

of

WORCESTER POLYTECHNIC INSTITUTE

In partial fulfillment of the requirements for the

Degree of Doctor of Philosophy

in

Electrical and Computer Engineering

by

Fardad Askarzadeh

July 2017

APPROVED:

Professor Kaveh Pahlavan, Major Dissertation Advisor

Professor John A. McNeill ECE Department Head

To My Wife

Abstract

The time-of-arrival (ToA)-based localization technique performs superior in line-of-sight (LoS) conditions, and its accuracy degrades drastically in proximity of micro-metals and human body, when LoS conditions are not met. This calls for modeling and formulation of Direct Path (DP) to help with mitigation of ranging error. However, the current propagation tools and models are mainly designed for telecommunication applications via focus on delay spread of wireless channel profile, whereas ToA-based localization strive for modeling of DP component. This thesis provides a mitigation to the limitation of existing propagation tools and models to computationally capture the effects of micro-metals and human body on ToA-based indoor localization. Solutions for each computational technique are validated by empirical measurements using Ultra-Wide-Band (UWB) signals. Finite-Difference-Time-Domain (FDTD) numerical method is used to estimate the ranging errors, and a combination of Uniform-Theory-of-Diffraction (UTD) ray theory and geometrical ray optics properties are utilized to model the path-loss and the ToA of the DP obstructed by micro-metals. Analytical UTD ray theory and geometrical ray optics properties are exploited to model the path-loss and the ToA of the first path obstructed by the human body for the scattering scenarios. The proposed scattering solution expanded to analytically model the path-loss and ToA of the DP obstructed by human body in angular motion for the radiation scenarios.

Acknowledgement

I am grateful that I am finally able to fulfill this long journey with all its ups and downs. I wish to express my sincere gratitude to my research advisor, Professor Kaveh Pahlavan, for his continuous guidance and instituting me with necessary amenities to overcome the challenges and in order to make the right choice in my study. Not only Professor Pahlavan is my academic mentor and a role model but also, a second father that showed me the way of life. He thought me no matter who you are, and what you do, at the end what counts is to be a good human being and a citizen to your society. I recall the first time I met Professor Pahlavan, he mentioned to me; "To do PhD research is like going on a trip to a city that you have never been there. You grab a map with a destination in mind, but the beauty and excitement of city may lead you to a better place beyond your imagination" , and suggested I should never "anticipate", which was a big lesson for me. I am extremely grateful and indebted to Professor Sergey Makarov for his expert, sincere and valuable encouragement, creative and comprehensive academic advices coupled with arrangement of critical simulation tools (i.e. 2D FDTD MATLAB) until this work come to existence. I would like to express my deepest thanks and sincere appreciation to members of my committee Dr. Yishuang Geng and Professor Yousef Mahmoud for their help and guidance on this dissertation, and take this opportunity to record my sincere thanks to all my colleagues that I had the pleasure of working

with in CWINS lab at WPI including Dr. Mohammad Heidari, Dr. Frit Akgul, Dr. Yunxing Ye, Dr. Guanqun Bao and my very good friends Mr. Bader Alkandari and Mr. Umair Khan for their endless helps, supports and guidance throughout this journey. I would like to place a record, my sense of gratitude to one and only, my wife as this accomplishment would not be conceivable without her endless love, support and encouragement in our life. I would like to express my gratefulness to my dear parents for supporting me in every step of my life and my grandmother whose memories for ever shall live with me.

Contents

List of Figures

List of Abbreviations

Abbreviation	Meaning
AoA	Angle of Arrival
BAN	Body Area Network
CWINS	Center of Wireless Information Networks
DARPA	Defense Advanced Research Project Agency
DDP	Detectable Direct Path
DME	Distance Measurement Error
DP	Direct Path
EM	Electromagnetics
FDTD	Finite Difference Time Domain
FEM	Finite Element Method
GO	Geometrical Optic
GTD	Geometrical Theory of Diffraction
HFSS	High Frequency Structural Simulator
IEEE	Institute of Electrical and Electronics Engineers
LoS	Line of Sight
MoM	Method of Moment
NDDP	None Detectable Direct Path
NIST	National Institute of Standards
NLoS	None Line of Sight
OLoS	Obstructed Line of Sight
PO	Physical Optics
PG	Path Gain
PL	Path Loss
RB	Reflection Boundary
RS	Reflection Signal
RSS	Receive Signal Strength
ToA	Time of Arrival
TE	Transverse Electric
TM	Transverse Magnetic
UDP	Undetectable Direct Path
UTD	Uniform Theory of Diffraction
SB	Shadow Boundary
SBR	Shooting and Bouncing Rays
RP	Reference Point
RT	Ray Tracing
UWB	Ultra-Wide Band
VNA	Vector Analyzer
WLAN	Wireless LAN

Chapter 1 Introduction

The immense applicability of indoor localization and Body Area Networks (BAN) have drawn special attention by the community with hope of unveiling challenges and alleviation of complexities associated to the applications in this area to contribute to the humanitarian safety and improvements to the day-to-day life of every individual. Required positioning applications to protect valuable lives of firefighters in an indoor area that is sabotaged by wild fires, army forces engaged in dangerous indoor battle grounds, miners working in dark and tight underground tunnels, tracking activities associated to a patient's or elderly's in a hospital or nursing room, and localizing diagnostic apparatus (i.e. endoscopy capsule) inside the human body [1][2] are just a small subset of those applications.

To put all this into perspective, while back when Defense-Advanced-Research-Project-Agency (DARPA) initiated an interest in indoor localization technology for all the known good reasons, millions of dollars were invested in this area, and the original assumption was to adopt the existing GPS technology in the indoor environments. CWINS lab at WPI at the heart of this activity, was the leading organization to call out on challenges associate to the un-predicable characterization of wireless profile channel for indoor localization [3] , and since then has pioneered variety of empirical models, later expanded into Human Body localization, to overcome some complexities and difficulties associated to these localization area. The current difficulties and challenges involved with indoor localization techniques are related to the unforeseen propagation behaviors in indoor environment due to scattered objects, where as in human body localization, those difficulties are associated to the complex geometry of human body parts and considerable variety of organ tissues. In such circumstances, the existing procedures and mathematical models will face inaccuracies that calls for new modeling approaches that is the concentration of this dissertation. The study presented in this dissertation is related to Time-of-Arrival (ToA)-based indoor and human body localization. We will elaborate on particular challenges associated to this technique for each of localization cases, and present novel solutions - based on applicability of electromagnetics (EM) numerical computational methods and analytical Uniform-Theory-of-Diffractions (UTD) approaches - to improve the accuracy of ToA positioning technique. In the remainder of this chapter, the background and motivation are discussed followed by our novel contributions and outline of the dissertation. The background and motivation associated to this dissertation will be discussed in the next section.

1.1 Background and Motivation

Recently, with advancements in signal processing and communication domains various research studies focused their attention to the problem of indoor localization. The indoor localization problem is considered a challenging and difficult problem to formulate and model mainly due to the ever-changing characteristics of the wireless channel [4]. Results of multitude of research studies has reported that ToA-based techniques perform superior in line-of-sight (LoS) conditions compared with received signal strength (RSS) and angle-of-arrival (AoA) techniques [3][5][6][7]. This is due to the fact that location bearing metrics obtained from LoS measurement are more accurate than RSS and AoA metrics. The ToA of the direct path (DP) can then be related to the distance of the antenna pair. In 2-D scenarios three accurate distance measurements from known reference points (RPs) are enough to precisely determine the location of the mobile terminal [3]. However, the accuracy of the ToA-based technique degrades drastically when LoS conditions are not met [8][9] , which is confirmed in various measurement campaigns [3][10].

In such scenarios, mitigation of the ranging error plays a vital role in improving the accuracy of the system. This necessitates the use of modeling and estimation of ranging error in non-line-of-sight (NLoS) conditions. The most realistic approach to model the typical values of ranging error in such environment is to conduct a physical measurement in such scenario [10][11] for empirical analysis.

Results of measurements reported in [3][14] illustrate that ranging estimates are greatly affected by the scattered objects around the transmitter and the receiver. As a result, it is difficult to associate the paths observed by measurements to those paths bounced from scattered objects and it is extremely difficult to differentiate the effects of micro-metals from other objects. To be specific, measurements conducted in the third floor of Atwater building in WPI revealed undetectable-direct-path (UDP) conditions that were associated to metallic chambers, elevator along the corridor, cabinets and doors. This initiated a new era in analysis of effect of micro-metals on ToA-based techniques as prior to that, the main emphasis of community was on understanding the effect of macro level metallic objects.

Similar to effect of micro-metals, the human body is not an ideal medium for RF wave transmission either. It is partially conductive and consists of materials of different dielectric constants, thickness, and characteristic impedance. Therefore, depending on the frequency of operation, the human body can exhibit high power absorption, central frequency shift, and radiation pattern disruption. The absorption effects vary in magnitude with both frequency of the applied field and the characteristics of the tissue, and shadowing should be considered for stationary and non-stationary position of body. The empirical procedures conducted by [15] indeed confirms the effect of human body on ToA-based localization systems, and in particular focuses on analysis of effect of angular motion of human torso on ranging errors. As part of the study, the paths observed from the measurement are a testimony to the UDP conditions that were caused by human body obstructing the DP component at each specific angle.

Therefore, a controlled simulation environment allows a more in-depth understanding of the problem. Unfortunately the existing models and simulation tools for propagation in general are designed for telecommunication applications with a focus on delay spread of wireless channel profile whereas; in ToA-based localization the focus should be the DP component. From those tools and computational methods we can refer to Ray Tracing (RT), Finite-Difference-Time-Domain (FDTD) method and Analytical UTD Ray Theory.

The RT algorithm functions based on fundamental image [16] and Shooting and Bouncing Ray (SBR) [17] techniques. A 2D RT simulation technique was originally developed [12] to analyze the behavior of wireless channels in small indoor areas using the two dimensional reflection and transmission model to trace rays by means of the ray shooting technique [4]. This model offered a low-cost means of propagation analysis for small indoor areas used for wireless local area network (WLAN) applications. Diffraction did not play a major role in most indoor radio propagation scenarios since the diffraction effect would influence propagation significantly only in locations such as corridors when the LoS path is blocked and the received signal involves multiple reflections and transmissions. However, this is not a likely situation for indoor WLAN applications, where terminals are typically used in reasonably open indoor areas. Later, a 3D ray tracing simulation [13] based on a typical residential area was developed to again analyze the behavior of wireless channel in macrocellular high-rise urban canyons with antennas installed above roof level. This simulation was based on the model that reflections and sharp edge diffraction were the main mechanism for simulation of signal propagation.

The FDTD method is probably the most straightforward and widely used method for numerical solution of Maxwell's equations, and belongs to the general class of grid-based differential time-domain numerical modeling methods. A more computationally efficient form of traditional FDTD method used for communication application has also been applied previously to indoor areas, showing significant improvement in accuracy over the rectangular FDTD algorithm. The computational time needed for this method was comparable to available three-dimensional ray-tracing algorithm at that time. A point-to-point comparison between predicted and measured power in all locations for two-dimensional and three-dimensional ray-tracing and for the FDTD models showed that both ray-tracing models and the FDTD model were all in good agreement with the measurements. However, ray-tracing provides a more accurate estimate of the power based on the standard deviation calculated against the measurements [4].

The UTD ray theory is ray-based asymptotic technique that includes diffraction phenomena and exhibits uniform properties in lit, transition and shadow regions. The Bertoni [18] is one of major contributors to the radio propagation and modern wireless systems, who he has utilized analytical UTD ray theory in outdoor and large urban canyons for telecommunication applications. The effort included diffraction by the tip of the houses, large buildings, hills, trees and jungles. The [19] has also utilized UTD ray theory for human body where Ghaddar and et. al. analyze effect of human body in indoor areas intersecting the LoS to capture the shadowing effect.

With respect to the modeling of DP component and ToA-based localization, there are two studies mostly focused on ToA-based human body localization. First is the studies conducted by [20] , leveraging numerical methods inside human body based on applicability of HFSS [21] and Finite-Element-Method (FEM), and the second one is the analytical UTD Ray Theory approach conducted by Zhao and et. al. [22] in a restricted manner limited to the geometry of human body, positioning of antenna pair in respect to the human body and etc.

This highlights the need for modeling and estimation of DP component and ranging error in proximity of micro-metals and human body that is the focus of this dissertation. The contribution of this dissertation will be discussed in the next section.

1.2 Contributions of the Thesis

This thesis provides a mitigation to the limitation of existing propagation tools and models to computationally capture the effects of micro-metals and human body on ToA-based indoor localization. Solutions for each computational technique are validated by empirical measurements using Ultra-Wide-Band (UWB) signals.

Figure 1.1 elaborates on the contribution of the thesis related to the two problem areas of ToA-based indoor and human body localization. There are four solutions proposed to the aforementioned problem areas. Electromagnetics (EM) computational method, and a combination of analytical UTD and geometrical procedures offered to model the effects of micro-metals on ToA-based indoor localization. Analytical UTD ray theory and geometrical procedures are used to model the effects of human body on ToA-based human body systems for scattering and radiation scenarios. Precisely, FDTD numerical method is used to estimate the ranging errors [23], and a combination of UTD ray theory and geometrical ray optics properties [24] are utilized to model the path-loss and the ToA of the DP obstructed by micro-metals [25]. Analytical UTD ray theory and geometrical ray optics properties are exploited to model the path-loss and the ToA of the first path obstructed by the human body for the scattering scenarios [26]. The proposed scattering solution expanded to analytically model the path-loss and ToA of the DP obstructed by human body in angular motion for the radiation scenarios [27].

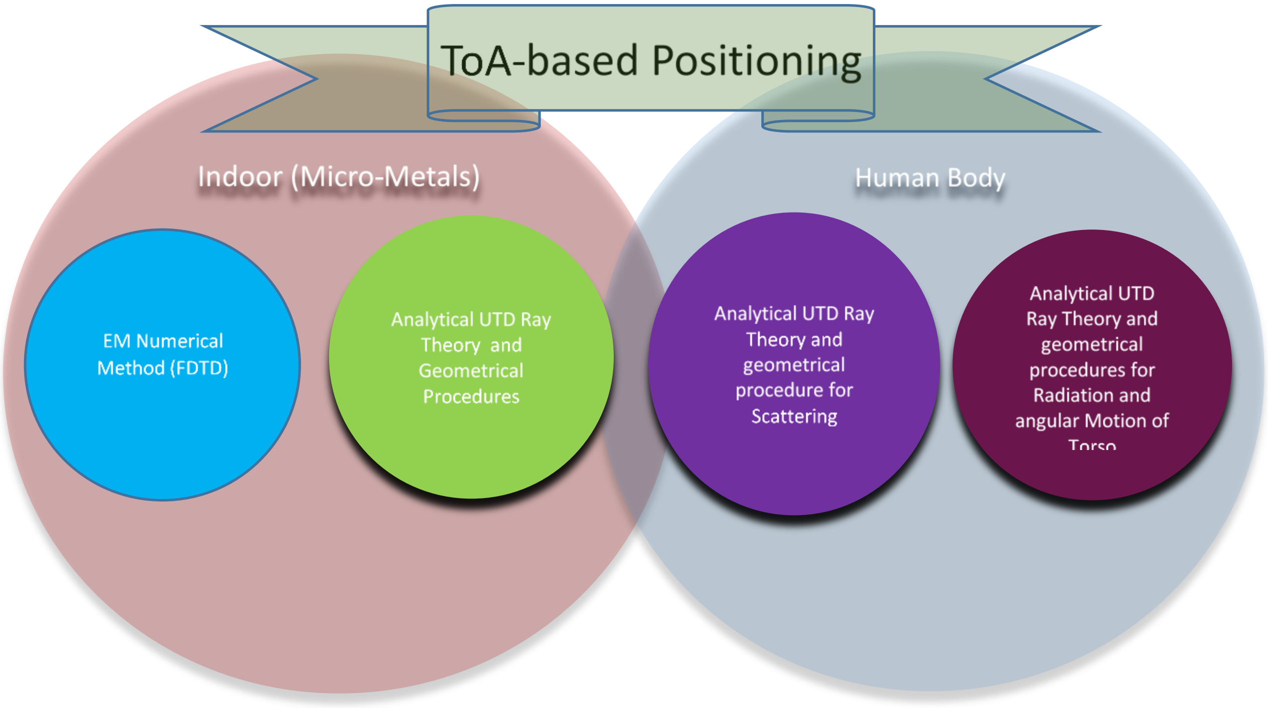

Figure 1.1 High-level contribution of the dissertation

The outline of the dissertation will be discussed in the next section.

1.3 Outline of the Dissertation

The remainder of this dissertation is organized as following; Chapter 2 provides an overview of ToA-based indoor and human body localization systems unfolding the actual techniques and challenges involved with that approach. The chapter continues with brief description of empirical measurement and computational methods associated with modeling the DP.

Both Chapter 3 and Chapter 4 focus on the effects of micro-metals on ToA-based indoor localization systems. Chapter 3 explores applicability of FDTD computational method by recitation of FDTD technique, and unveiling the measurement setup and the simulation domain specific to the experimental scenarios. The validation of simulated ranging error with the measurement is presented at the end of the chapter. Chapter 4 investigates applicability of analytical UTD ray theory and geometrical ray optics. It provides an overview of measurement setup and formulation of UTD conductor screen path-loss and geometrical ray optics formulation of ToA followed by validation of analytical path-loss, ToA and DME with the measurement. Both Chapter 5 and Chapter 6 focus on the effects of human body on ToA-based indoor localization systems. Chapter 5 investigates applicability of analytical UTD ray theory and geometrical ray optics for scattring by the human body. The chapter starts off by covering measurement setup and formulation of UTD ray theory path-loss models and geometrical ray optics formulation of ToA followed by the validation of those proposed models with the measurement. In Chapter 6 , we investigate applicability of analytical UTD ray theory and geometrical ray optics for radiation scenarios by the human body in angular motion, which are validated with the measurement. Appropriate modifications are proposed to the model to help gapping the short falls around instabilities observed in the analytical results. The last section of this chapter illustrates a 3D model to count for variable positioning of transmitter and angular motion of receiver at the same time.

Finally, Chapter 7 concludes the dissertation and provides feedback on the future directions.

Chapter 2 Background on ToA-based Localization Systems

2.1 Introduction

The emerging technology of “internet of things” helps information remain local thru connection of lots of devices, which operates based on short distance communication and precise localization. Their communication employs high data rate and precise localization helps to overcome the interference and minimize the noise (i.e. beamforming). The precise localization needs ToA-base technique, and for ToA-based ranging the strength and ToA of DP are important.

A classic indoor localization system entails base stations referred to as anchors (RPs) along with mobile terminals for tracking purposes. The based station architecturally is attached to an engine node capable of leveraging a variety of positioning algorithm while tracking each terminal. The system could benefit from a variety of ranging matrices in order to acquire the positioning data such as: RSS, ToA, AoA and etc. Due to implementation nature of RSS and ToA that tracks the ranging figures, those are considered as ranging matrices. The positioning algorithm for those techniques would require at least three ranging estimates from different

RPs to locate the mobile terminal. In the case of AoA however, two estimates from the RPs would help with a satisfactory localization.

In particular and in case of ToA-based indoor localization system, the positioning algorithm operates based on the time an impulse with the speed of light travels between the terminal and each of the RPs to determine the prevailing separation. The operational requirement for this technique is rather simple; the time difference between an emanating impulse from the transmitter antenna and the very first received pulse arriving at the receiver antenna correlates to the ToA , and detectable first path is referred to DP for both indoor localization and BAN [28][29].

In the introduction section of this dissertation, we discussed the accuracy of the ToA-based indoor localization technique degrades drastically when LoS conditions are not met [8][9] , which is confirmed by the various measurement campaigns [3][10]. It is known the existence of macro/micro level metallic objects (i.e. chamber, doors, and cabinets), walls and influence of individual human bodies in the vicinity of antenna pair results severe ranging errors caused by multi-path reflection, blockage and severe attenuation of DP. In case of multi-path reflections, followed by the first impulse response, there are consecutive pulses arriving at the destination that are manifested by the reflection of emanating impulse from the screening objects in the environment. In addition, the blockage of DP component by the metallic objects and its diffraction by the sharp edges are the condition that leads to large degradation of DP power and severe Distance-Measurement-Error (DME) of the first path that is confirmed by [10][30]. Specific to multipath scenario, a superposition of DP with the received multipath pulses at the receiver side results in shifting of the expected first path resulting in ranging errors that are confirmed by empirical procedure provided in [31][32].

In such scenarios, mitigation of the ranging error plays a vital role in improving the accuracy of the system. This necessitates the use of modeling and estimation of ranging error in non-line-of-sight (NLoS) conditions. The most realistic approach to model the typical values of ranging error in such environment is to conduct a physical measurement in such scenarios [10][11][29][31][32][33] for any empirical procedures and developing statistical models.

Specific to human body ToA-based localization systems, [34][35][36] in particular explores empirical procedures in the proximity of a human body in angular motion, and [37] explores applicability of angular-based statistical models with a focus on the first path around the body in the pursue of better understanding of the DP behavior in the proximity of human body. The result of statistical models offered for ToA-based indoor and human body ToA-based are a testomony to the fact; inacurrencies invovled with ToA estimates are directly associated to the specifics of environment (i.e. screening objects, geometry of human body part) [10][11][34][35][37] and the bandwith, SNR and power of the signal [33][34][35] .

While the empirical procedures have utilized the community modeling capabilities for the ToA-based localization systems, it has proclaimed itself as a tedius and time-consuming procedure to conduct. Therefore, researchers have examined variety of approaches to avoid the physical measurement. The first approach was to use RT and estimate the ranging error [12][13]. This initial versions have utilized 2D and 3D features with a focus on the delay spread of the wireless channel profile for telecommunication purposes. In telecommunications, the delay spread of the wireless channel profile is important while ToA-based localization applications strive for modeling of the DP component, which is directly related to the ranging error. The early version of ToA-based empirical procedures conducted by [38] leverage this 2D RT software version. The model offered use the results of measurement-calibrated ray-tracing software to develop a statistical model for the DME and to relate that to the bandwidth of the sensor.

The full-wave EM computational methods has also been recognized as an alternative computational solution to analyze the delay spread of the wireless channel profile. In particular applications based on traditional rectangular FDTD algorithm and a more computationally efficient method were used to model the indoor propagation problems but their focus were mainly on the telecommunication applications rather than localization. A number of research projects also have been carried out using one or more computational techniques to model Body Area Network channels. Among these, the most popular were FDTD, used by the National Institute of Standards and Technology (NIST) [39], and Method-of-Moments (MoM) used by the IEEE P802.15 working group [40]. Both of these projects involved the modeling of the power delay profile of the human body channel for medical communication purposes, and not for TOA-based localization.

The Khan et. al. in [41] are the very first in the community that have used EM numerical methods for human body ToA-based localization purposed and have leveraged the applicability of a full-wave simulator HFSS on a 3D human body domain to analyze the DP phenomenon for 900 MHz with 100 MHz bandwidth.

In the past, analytical procedures based on applicability of UTD ray theory were employed for communication purposes in large urban canyon areas with hills, forest , high rises [18] , which localization was not the real goal. In an effort to estimate ranging errors in the proximity of human body, [22][42] have further explored applicability of UTD ray theory for coupling and scattering scenario’s respectively, that are tight to very limited conditions and in some cases their validation approach is questionable.

Considering the importance of modeling and estimate of the DP component for ToA-based indoor and human body localization, we will provide a brief background on the ToA techniques in this chapter. The challenges associate to ToA-based technique are discussed , where the main focus of chapter will be on blockage , diffraction , and the severe attenuation of DP in proximity of micro-metals and human body. Empirical measurements, Ray Tracing, EM computational methods and UTD Ray Theory are discussed as possible computational methods to help with modeling and estimation of DP component.

The remainder of this chapter is organized as following; section 2.2 provides an overview of ToA-based localization technique. Section 2.3 discusses the challenges invovled with ToA-based localization technique . In Section 2.4 we discuss empiricial measurement campain for ToA-based technique and finally section 2.5 elabrates on computational methods invovled with ToA-based technique.

2.2 ToA Based Techniques

In order to discuss the ToA-based indoor localization, we will start off by explaining the multipath channel impulse response model represented by equation (2.1) [4][43][45]:

$$h(\tau) = \sum_{k=1}^{L_p} \alpha_k \delta(\tau - \tau_k) \tag{2.1}$$

, where L_p is the number of multipath components, and $\alpha_k = |\alpha_k| e^{j\varphi_k}$ and τ_k are amplitude and propagation delay of the k^{th} path at the receiver, respectively. The first peak of received signal in a LoS condition is called the detectable-DP (DDP), which its value is a function of bandwidth and the occurrence of undetectable-direct-path (UDP) conditions.

The ToA-based localization technique is one that relies on ranging estimates that are directly derived based on the time DP pulse travels from the transmitter to the receiver with the well-known speed of light. As a matter of fact, the single important entity of having an accurate estimation in a multipath environment is the ToA of the first path (or DP) in a LOS condition. A ToA sensor estimates the distance from a reference point based a following basic equation (2.2):

$$\widehat{d}_w = c\widehat{\tau}_{1,w} \tag{2.2}$$

, where c is the speed of light and $\tau_{1,w}$ is an estimate of the ToA of the direct path for a specific system bandwidth. The studies conducted by [46][47][48][49] confirms the Ultra-wide-band (UWB) measurement provide the widest bandwidth which leads to more accurate resolution of DP. Consequently, associate to each $\tau_{1,w}$ there is a distance error that is defined as:

$$\varepsilon_{d,w} = \widehat{d}_w - d \tag{2.3}$$

, where d is the actual distance between the sensor and target object.

The fact the accuracy of ToA systems has bandwidth dependency, would necessitate the need of complex receivers compare to other positioning systems involved with different positioning algorithm. Another important aspect of accurate ranging estimate using a ToA system is taking advantage of clock synchronization between the transmitter and the receiver that usually happens through frequent exchange of synchronization tokens between the mobile terminal and RPs. While at least three RPs needed for accurate positioning, a fourth RP maybe used to legitimize the timing between various terminals in the system [50].

It is worth mentioning, beside the estimation of ToA, the computational tools that are involved with simulation of DP (i.e. RT algorithm operating based on reflection and transmission methods) take advantage of actual distance (d) in order to calculate the distance power. To calculate the distance power between the transmitter and the receiver, we use the average RSS and a distance-power relationship to determine the $\widehat{d}$. If we define the DME as the difference between the measured and actual values of distance, $\varepsilon_d = \widehat{d} - d$, the "error" in RSS systems would be independent of the bandwidth of the system. The power is calculated by based on the common principle behind all RSS-based statistical presented in equation (2.4):

$$RSS_d = 10\log_{10} P_r = 10\log_{10} P_t - 10\alpha\log_{10} d + X \qquad (2.4)$$

The model is referred to as lognormal, where P_t is the transmitted power, d is the distance between the transmitter and the receiver, and α is the distance-power gradient of the environment. The random variable X is a lognormal distributed random variable representing shadowing effects.

Based on different values of α and X, the lognormal model can be employed for a variety of indoor localization that are discussed in details by [51]. In the case of propagation in the proximity of human body, the environmental variations and body movements will have direct influence on the path loss resulting in a different mean value for a given distance. This phenomenon is called shadowing, and it represents the path loss variation around the mean. As an extension to this model, Yazdandoost et.al. in [39] introduce variety of statistical path-loss models for medical device implants, and a series of RSS-based techniques [52][53][54][55] are utilized by CWINS lab at WPI to help with localization accuracy of wireless capsule endoscopy.

In the next section of this chapter we will discuss challenges involved with ToA-based localization technique and expand the discussion to diffraction phenomenon in the proximity of micro-metals and human body.

2.3 Challenges for ToA techniques

The indoor radio channel suffers from severe multipath propagation and heavy shadow fading conditions so that measurements for localization are far from accurate in many instances. In general, measurements for indoor ToA-based technique provide very unreliable results as their estimates are susceptible to large errors due to undesirable multipath conditions.

The classification of multipath channel response is comprehensively analyzed in [10] and divided into DDP, none-detectable-direct-path (NDDP) and UDP.

- DDP: In a LoS condition, A DDP class is one that DP is the strongest path and easily detectable at the receiver side.

- NDDP: In a Obstructed-Light-of-Sight (OLoS) condition, The NDDP class relates to scenarios the DP is blocked by a rather dielectric object (i.e. window wood frames) resulting in attenuation of DP. In this case the DP is no longer the strongest but still detectable by the ToA-based localization system.
- UDP: In a OLoS condition, The UDP class depicted by relates to the scenario DP is blocked by metallic object or human body; or aggregated with other existing multipath resulting in large attenuation of DP. In this scenario, the DP power experience severe power loss to extend it falls below the ToA-based localization threshold, where it is no longer detectable by the antenna receiver.

To accurately estimate ToA in indoor areas, we need to resort to different frequencies of operation and more complex signaling formats and signal processing techniques that can resolve the problems. The behavior of a ToA sensor in indoor multipath propagation is highly sensitive to the bandwidth of the sensor. The UWB systems, which exploit bandwidths in excess of 1GHz, have attracted considerable attentions as a means of measuring accurate ToA for indoor geolocation applications [46][47][48][49]. However, as in other ToA systems, UWB systems cannot completely avoid UDP problems [56].

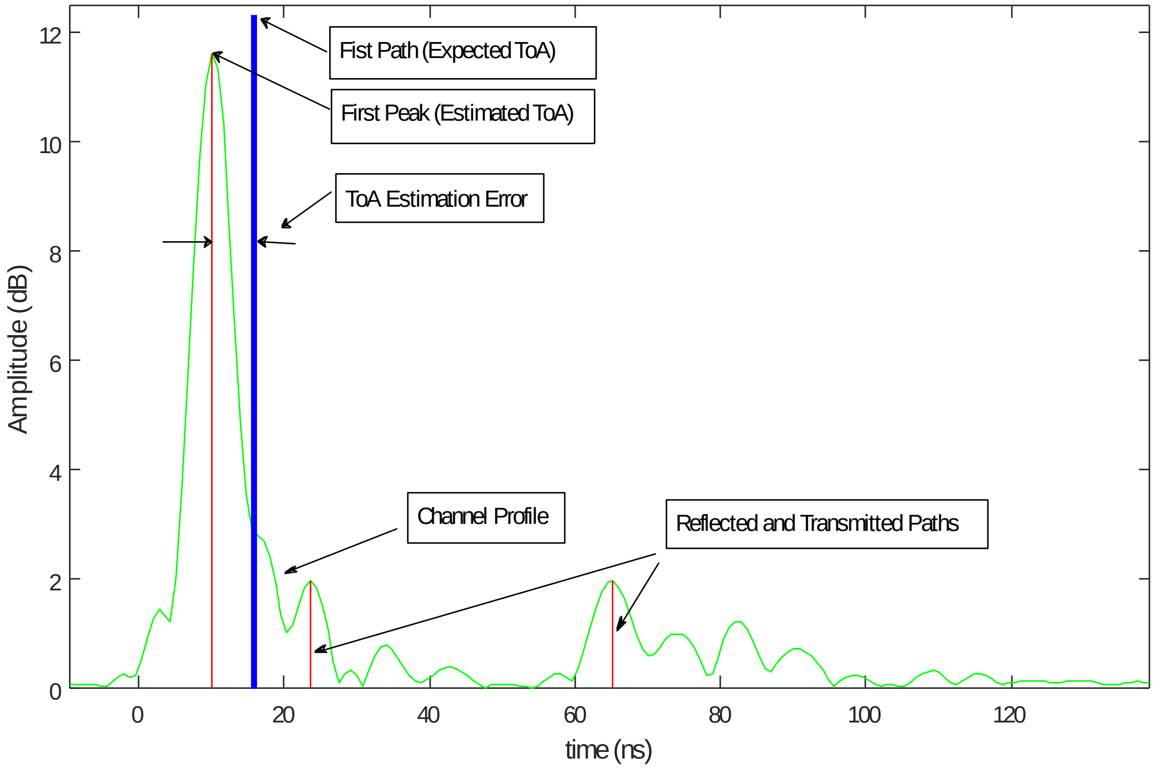

Figure 2.1 Parameters involved in wideband TOA measurement using arrival of the first path directly connecting the transmitter and the receiver.

Figure 2.1 shows the basic concepts involved in wideband TOA measurements using the arrival time of the first path in a typical indoor multipath environment [57][58]. In this figure, the DP is represented by the first path, which is also the strongest path. Location of this path is the expected value of the ToA. Other paths with a number of reflections and transitions arrive after the DP with lower amplitudes. These paths would have been observed at the receiver if the bandwidth of the system were infinite. In practice, bandwidth is limited, and the received signal comprise a number of pulses whose amplitudes and arrival times are the same as impulses but they are shaped pulse. The superposition of all these pulse shapes forms the received signal, which we refer to as the channel profile. A common practice is to estimate the location of the DP as the location of the peak of the first path that, is the estimated ToA. In a single path environment, the actual expected and the estimated direct paths are the same. In multipath conditions, however, the peak of the channel profile gets shifted from the expected ToA, resulting in a ToA estimation error caused by the multipath condition. We refer to the distance error caused by erroneous estimate of the ToA as the DME, which can be calculated using equation (2.3) as discussed in the previous section. For a given multipath condition we expect that as we increase the bandwidth the distance measurement error becomes smaller.

As a mobile terminal moves away from a base station the strength of the DP and the total received signal power decay exponentially. The scenario is categorized as OLoS condition as the DP drops below the threshold while other paths are still

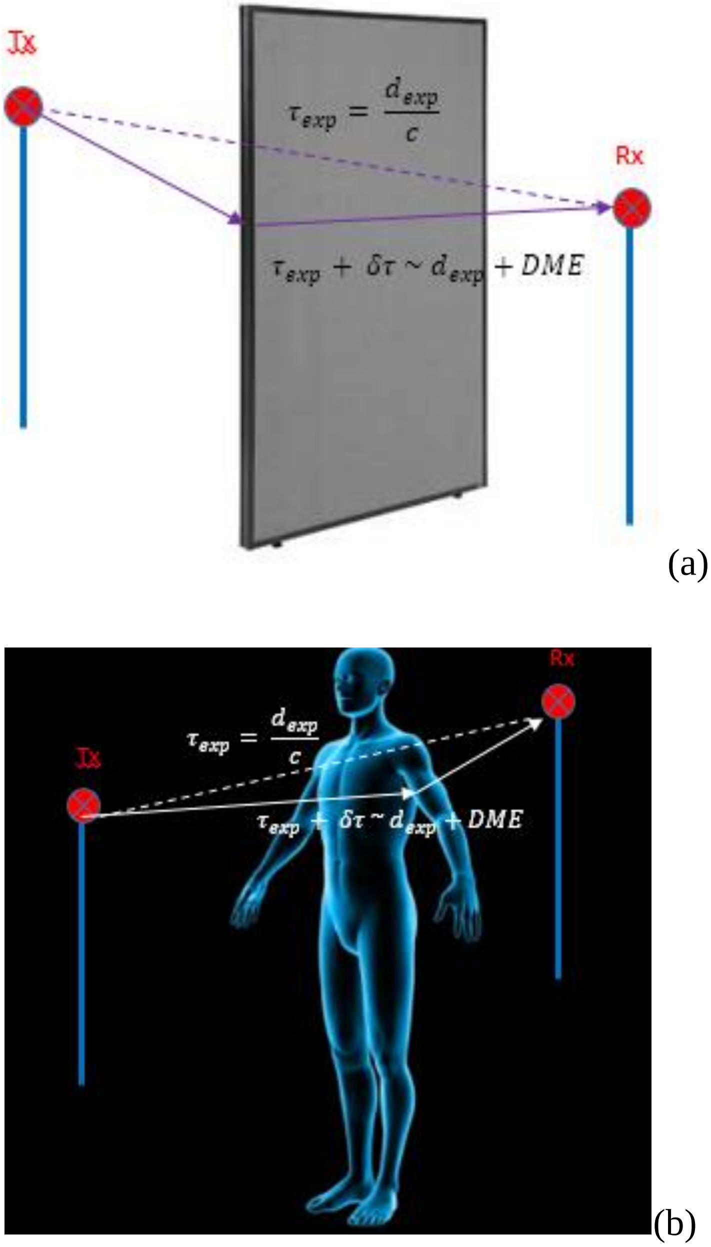

Figure 2.2 Challenges involved with ToA-ranging: blockage of DP by (a) metallic object or (b) human body.

detectable. In this situation the receiver considers the first detectable path in the wireless channel profile to be the DP resulting in substantial ranging error associated to the wideband ToA-based empirical procedures. We refer to this situation the UDP condition [56].

Alternatively, one major challenge with ToA-ranging associates to blockage of DP by the metallic objects or human body. Figure 2.2 depicts a scenario the transmitter and the receiver are positioned within the certain vicinity of each other. In this situation, the ToA of the DP (τ_{exp}) collates to the direct distance between the antenna pair (d_{exp}). Once a metallic object or human body is placed in between the antenna pair, it blocks the DP, and what is received at the receiver antenna are diffracted paths. Those diffracted paths are attenuated version of expected DP, which arrive at $\tau_{exp} + \delta\tau$, and correlate to $d_{exp} + DME$. This is a classic UDP condition and behavior of signal for this condition are consequently shown in Figure 2.3. In this figure the left hand signal resembles the DP at the transmitter at time $= 0$. While we are expecting DP path signal to arrive at the receiver side at τ_{exp} (~ d_{exp}), with negligible power attenuation, upon blockage of DP by a metallic object or human body , an attenuated version of expected DP (signal in the middle) will

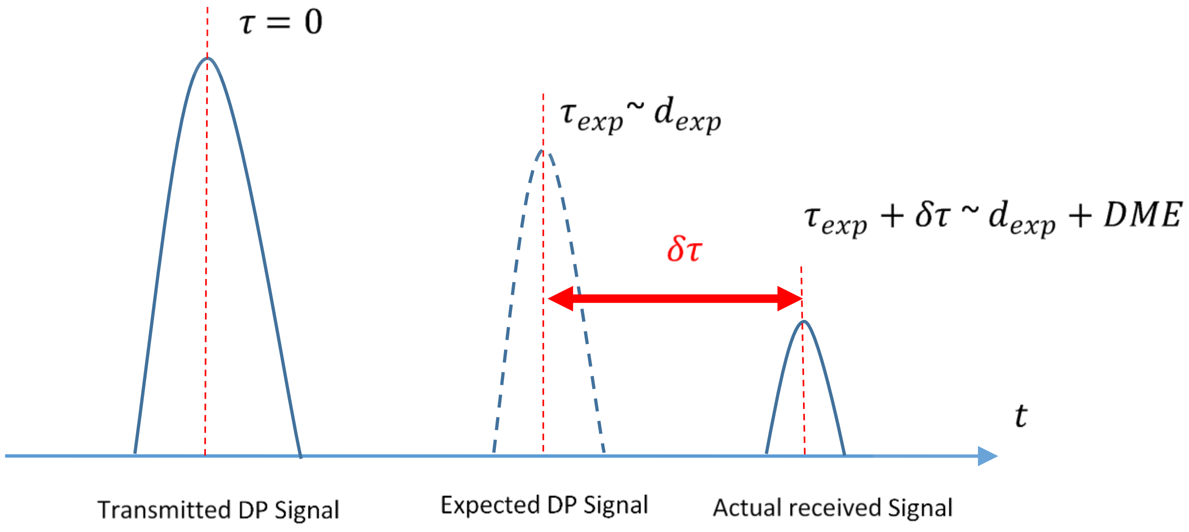

Figure 2.3 Challenges with ToA-ranging: Behavior of expected and actual DP signal.

2.3.1 Diffraction in Proximity of Metallic Objects

In the previous section we discussed in addition to the multipath condition, blockage of DP by a conductor (metallic) object and its diffraction by the sharp edges of that conductor object, would result in severe power attenuation of the DP and therefore leading to a UDP condition. We elaborated during empirical procedures the ranging estimates are considerably influenced by the surrounding objects in the proximity of a pair of transmitting and receiving radio devices. To be specific it is difficult to associate the paths observed in the measurement to those reflected by the scattered objects and specifically extremely challenging to distinguish the effect of micro-metals.

Understanding the diffraction phenomenon plays a vital role on analysis of DP component in the proximity of micro-metals, and it is worth to spend some time to describe this phenomenon. Upon the incidence of a propagated plane wave to a metallic-object (metallic door), that part of wave that hits the edges, gets diffracted and continues traveling behind the object as a cylindrical wave. This diffraction phenomenon is shown in

Figure 2.4-I.

Figure 2.4-I schematically depicts a dipole antenna (which is the type of antenna we sometimes use for our wideband measurements) away from a metallic plane object (a metallic door in our measurement case).

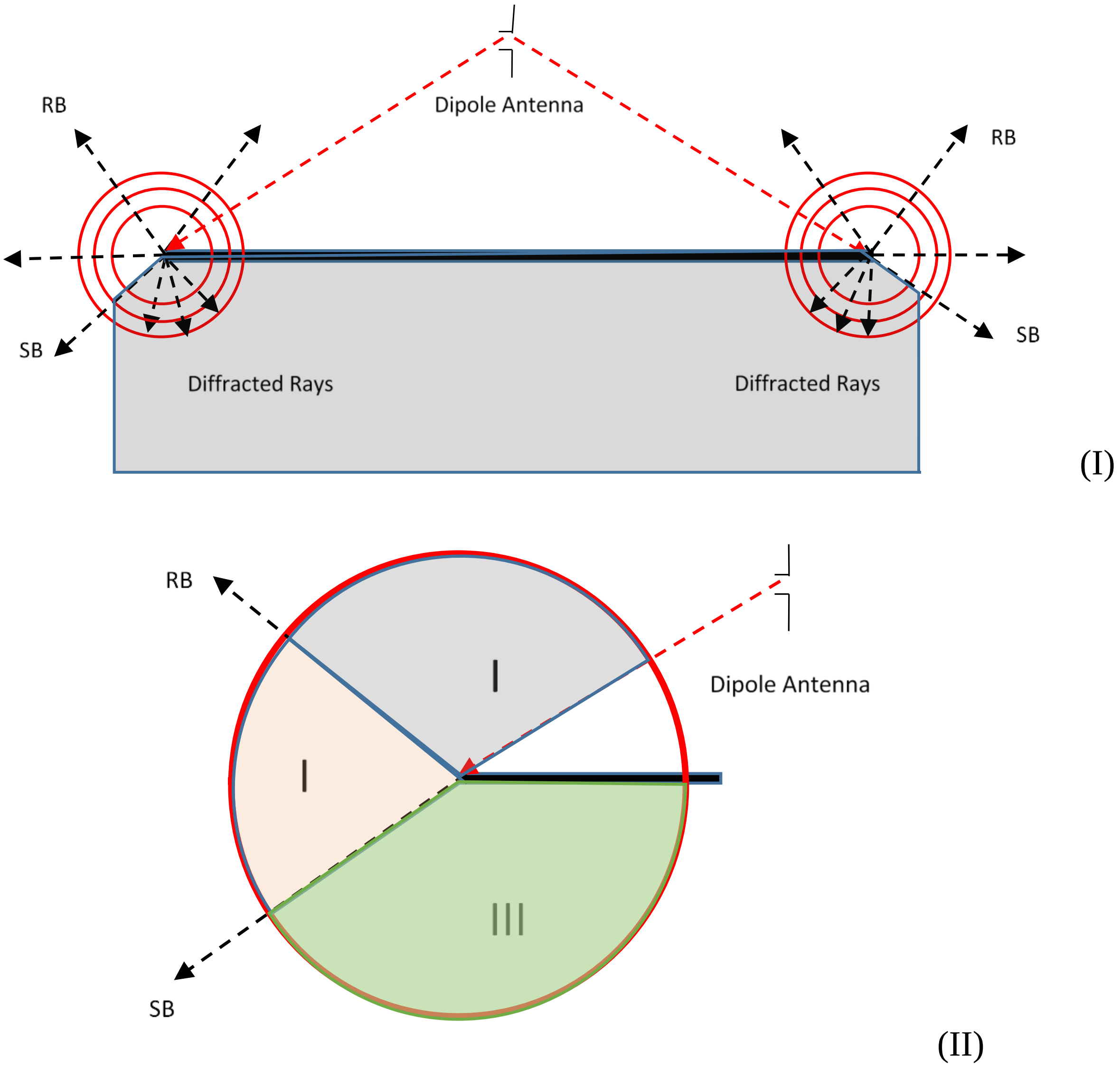

Figure 2.4 I) Geometrical optics approximation for a dipole antenna above a metallic plane ground II) Problem formulization in term of tm to z-axis field.

At the same time, in terms of geometrical optics or GO (used in ray tracing), the total field is considered to be a combination of rays emanating from the dipole and then reflected from the metal surface according to the Snell’s law. According to geometrical optics the field everywhere within the reflection boundary (RB) in

Figure 2.4-II is a combination of the incident (line-of-sight or LOS signal) and the reflected signal (RS). The field everywhere outside the reflection boundary but still inside the shadow boundary (SB) is the LOS signal from the dipole. The field below the shadow boundary is zero.

Ray tracing is using both diffraction theory and GO i.e. the Geometrical Theory of Diffraction (GTD), which is mostly related to 2D problems. In the first half of the last century there was relatively little work on high frequency diffraction. However all that changed in 1953 when Keller introduced the Geometrical Theory of Diffraction (GTD) as an extension of geometrical optics to include diffracted rays [59][60][61]. This theory introduces diffracted rays in addition to the usual geometric optical rays (used in Ray Tracing). Unlike geometric optics, the diffracted rays can *enter* the *shadow* regions. This is a very important concept, because it makes it possible to calculate the high frequency radiation from antennas and scatterers of a quite general shape and to understand the various radiation mechanisms involved. Also, the GTD motivated the asymptotic treatment of the numerous canonical problems to determine the fields diffracted from edges, vertices and smooth curved surfaces [62].

Physical Optics (PO) is a division of optics that analyzes interference, diffraction, polarization or in general any properties, in which the approximation of Geometrical-Theory-of-Optics (GTD) is not valid. The terms “physical optics approximation” applies to the computational methods amid Geometrical Optics, which ignores effect of electromagnetic waves, and full electromagnetics, which is pure theory. The term “physical” implies the real focus is on the physical than geometric or ray optics and in reality not a physical theory. The term “approximation” applies to using ray optics to estimate the field on a surface and integrating the field over surface to calculate the transmitted or scattered field. In Optics, it is referred to customary procedure of estimating diffraction effects. The physical optics approximation t allows us to find the currents on metal surfaces through the incident field, and then recalculate the secondary radiation by that current, like the diffraction mechanism. In terms of the primary or incident wave, the surface current density on a metal conductor reads.

$$\vec{J}_{surface} \approx 2\hat{n} \times \vec{H}_i \tag{2.5}$$

In this equation, $\vec{J}_{surface}$ is the surface current $\hat{n} \times \vec{H}_i$ and is the magnetics field orthogonal to the conducting surface. Both the GTD and PO become very involved when the number of scatterers (micro-metal objects) increases. Nevertheless, the ray tracing can still be developed for very large structures, and more important drawback of ray tracing is that it not capable of modeling *resonant* micro-metal objects.

2.3.2 Diffraction in Proximity of Human Body

In the case of the BAN and the human body ToA-based localization systems, we often deal with scenarios that either one or both of the sensors are mounted on the surface of human body or in the proximity of subject matter. The statistical models discussed in [63] illuminate to the fact that blockage of the DP by the human body leads to classical EM diffraction phenomenon called creeping waves over the human body. This creeping waves phenomena exhibit an exponential decay of power, which depends on the loss in the dielectric and where the conductivity is higher. The large projection of path-loss for the penetrating propagation through the human tissue leads to believe the penetrating portion will not survive the human body. For example the path-loss projection from the sternum to the spine is to be as high as 90 dB at 400 MHz , and as a result we can concluded the contribution of penetration compare to the creeping portion is much less and could be even neglected. This is the typical OLoS scenario that leads to the UDP condition in proximity of human body. This behavior is also confirmed by the statistical models provided in [64] , which demonstrates 6 – 8 $^{dB}/_{cm}$ attenuation for penetrating wideband RF signals within the human body.

Upon blockage of the DP by the human body, the creeping waves start traveling in different directions over the head or around the body [15][63]. The shortest creeping wave path to the receiver is called the first peak and the statistical modeling provided in [37] confirms the first peak exhibits large path-loss as the angle between transmitter and receiver increases.

To elaborate on an NLoS condition related to the human body ToA-based localization systems, let’s consider two Body-to-Body and Body-to-external scenarios associated to the surface sensor mounted on the human body [25]. Each experiment can be further divided into the LoS and NLoS conditions. In the LoS scenario, there is a direct unobstructed path between the transmitter and the receiver, and in the NLoS scenarios the body blocks the signal from direct connection path between the transmitter and the receiver. Figure 2.5 shows the results of two measurement experiments for body surface to body surface for LoS and body NLoS conditions, using Ultra Wideband (UWB) frequencies. In LoS experiment, we can clearly see the direct path which is also the strongest path. Considerable changes in multipath profiles necessitates for separation of LoS and NLoS channel models for these scenarios application.

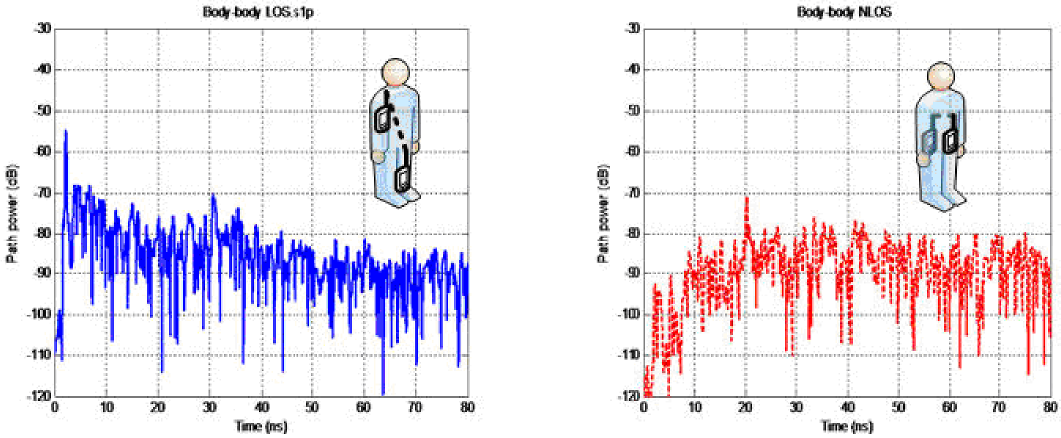

LOS – Body-to-Body

NLOS – Body-to-Body

Figure 2.5 Channel impulse response in for different orientations of the body at UWB Frequencies.

2.4 Empirical Measurement of ToA

In the early days of indoor wireless networking development, all wideband measurements were aimed at telecommunication applications, where the interests center mainly around signal coverage and rms delay spread analysis using frequency domain measurement [4][11][65][66]. The main objective of the indoor channel measurements is to establish a realistic foundation for the evaluation of indoor channel models. Measurements targeted for indoor geolocation application were initially carried out in Center for Wireless information Networks (CWINS), and they were conducted primarily for empirical procedure to study the distance measurement error behavior for different indoor environments [10][38].

The most commonly used measurement technique for TOA-based localization is employment of 40 GHz Agilent E83633B vector analyzer (VNA) used to sweep a specific frequency spectrum with specific sampling points (i.e. 3 – 8 GHz with 1601 sampling points) as depicted in Figure 2.6. After passing through a 30-dB amplifier, the output is connected to the transmitter antenna (Skycross SMT-3TO10M) by a cable. The receiver is connected to an attenuator and then, through a low noise amplifier (LNA), to the receiver port of the network analyzer. The transfer function of the channel is measured through VNA $S21$ S-parameters. The antennas are two UWB cone antennas and the analyzer has a sensitivity of -100dBm. The measurements are further calibrated to remove the effects of the lossy cables, power amplifiers and other system imperfections. The measured frequency-domain data are passed through a Hanning window to further suppress the unwanted side lobes. Then the IFT is applied to estimate the time-domain channel profile. A threshold is used to characterize the channel profile according to the power of the direct LoS path.

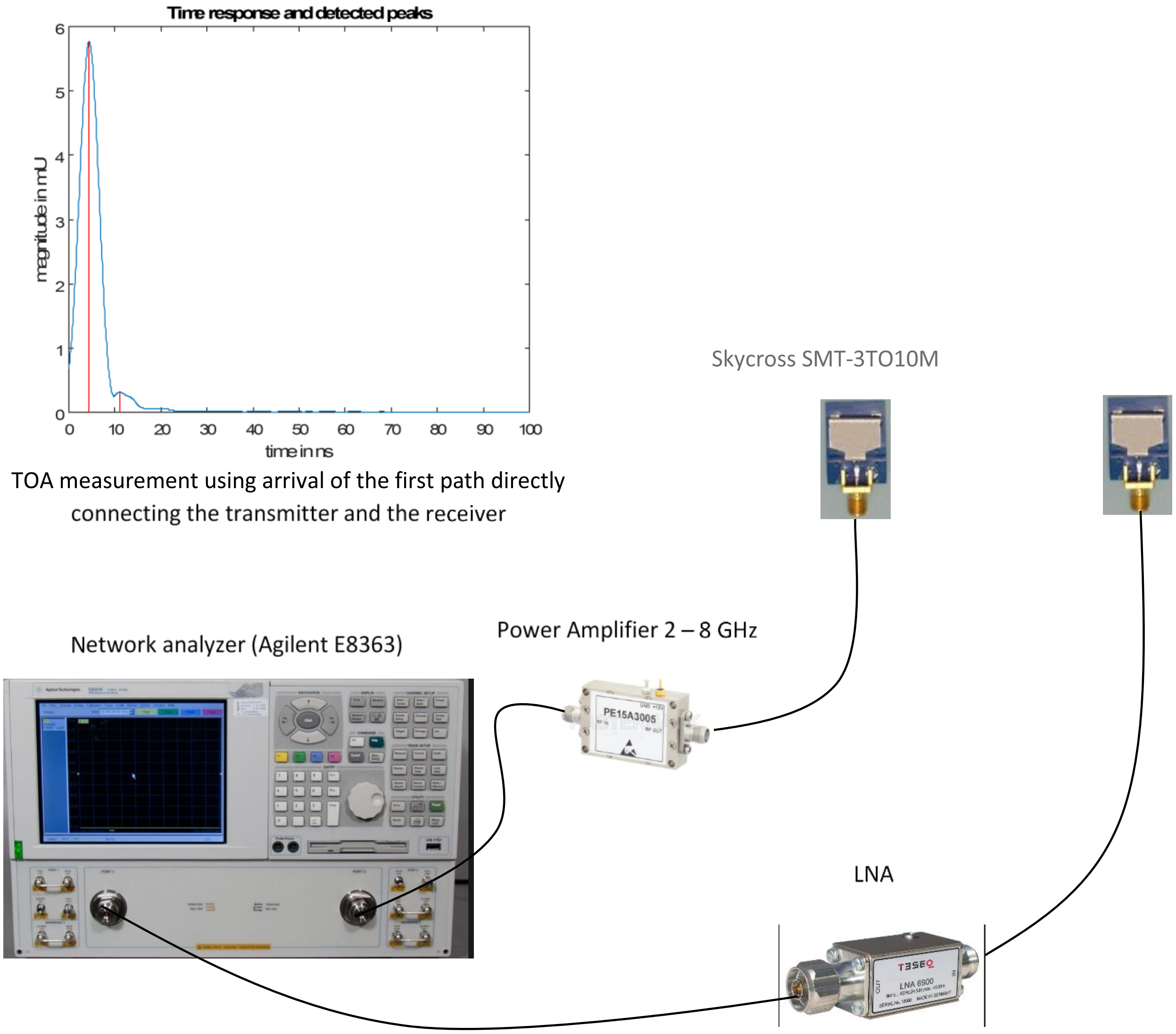

Figure 2.6 Measurement system used for UWB ranging measurements.

Estimating the time-domain power-delay profile requires estimating the relative amplitudes and delays of the arriving multipath components. Distinguishing between actual paths and measurement system noise required the implementation of a noise threshold. Since the noise floor of the measurement system is -100 dBm and the Hanning window has side lobes of -31dB relative to the peak of the profile, a threshold is selected according to the larger of the two values. Then, the first path having power greater than the noise threshold is the first detected path. The same measurement configuration, excluding the power amplifier, also applies to wideband measurement campaigns.

2.5 Computational Methods for Estimation of ToA

In the previous sections, we discussed ToA-based localization technique strive for modeling of DP in a NLoS. We discussed the most realistic approach to model ranging errors are empirical procedures, however conducting measurements are time-consuming and tedious. In this section we will review a series of computational techniques that will be used in this thesis for the modeling and estimation of DP in ToA-based indoor and human body localization.

2.5.1 Ray Tracing Algorithm

The Ray Tracing algorithm is an optimal tool for modeling radio propagation without incurring the labor cost of conducting empirical measurements. The RT techniques are approximations to the direct solution of electromagnetic wave propagation equations. As a ray meets a wall, two paths emerge, one reflected and the other transmitted through the wall. There are two general approaches that can be employed to calculate these paths. The first uses optical images of the transmitter and receiver. In this approach, reflections of the transmitted signal by various reflecting objects in the floor plan are described by images of the transmitter, and these images are used with images of the receiver to find all the paths to the receiver. The second method for determining the reflected and transmitted paths is through the application of ray-shooting techniques. A pincushion of rays is sent out from the transmitter, and the progress of each ray is traced through the environment until the ray has either intersected the receiver or has lost enough power that its contribution to the received signal is negligible. The time of arrival, intensity, phase and direction of arrival are recorded for each ray that intersects the receiver. Once every ray has been traced to completion, the channel impulse response is formed. The user interface of a typical 2D RT software package is shown in Figure 2.7.

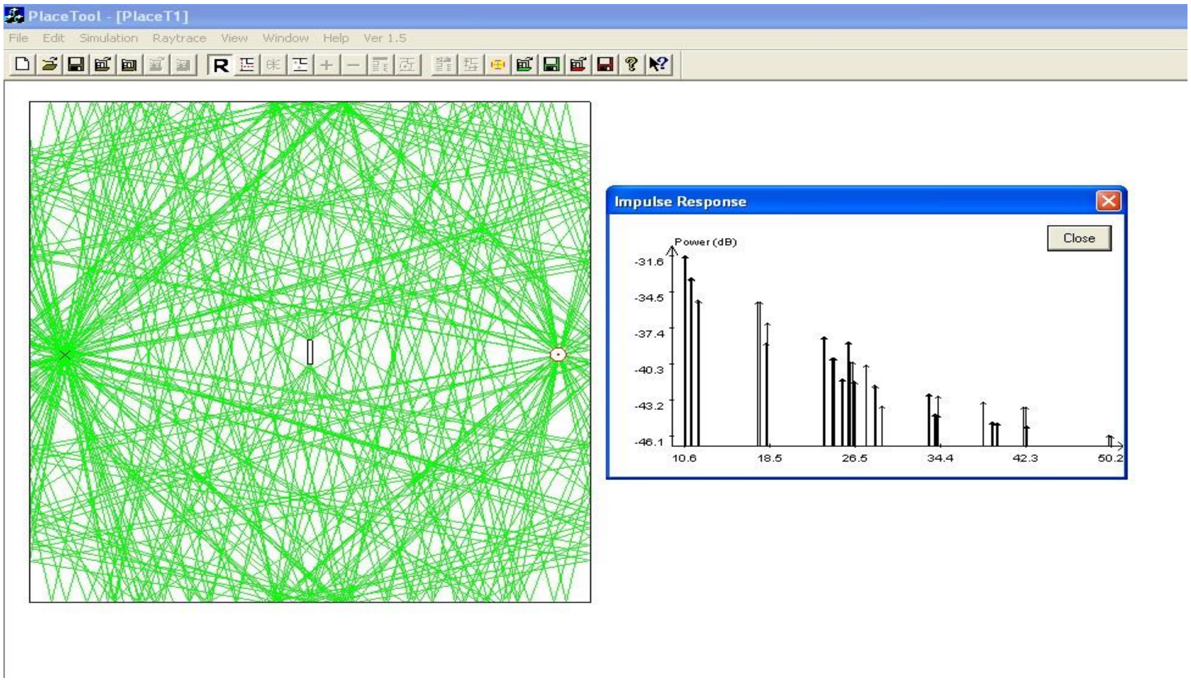

Figure 2.7 Typical user interface of a 2D Ray-Tracing software.

In this figure, the transmitter is represented by the red dot in the graph on the left screenshot in **Figure 2.7**, and the receiver is represented by the cross mark. The small bar in the center represents the overhead view of a metallic door. The channel impulse response is shown in the graph on the right screenshot. The same MATLAB code used to extract and process measurement data and is also used to process the RT simulation result. The dielectric constant of the walls and micro-metals in the graph can be adjusted to match the real environment. Specific to this simulation scenario, the power of the DP between the Tx and Rx would be significantly reduced by the metallic door, and since during the DME estimate and the selection of the first path the effect of diffraction has not been included in the current RT software, we will erroneously consider the reflected path from the outer walls as the direct path and thus the model suffer large positive ranging errors.

Figure 2.8 illustrates an increase in separation of transmitter and receiver in the simulation environment helps with discrepancy of DP and the reflected paths by the walls. In another word, larger distance between antenna pair, closer neighboring and less distinction between the length of the DP and reflected path decreases, which leads to the reduction of the DME. The simulation results captured in Figure 2.8 confirms this kind of error.

Figure 2.9 depicts a flow diagram of procedures involved with generating a channel profile for ToA-based localization systems. The RT algorithm, operating based on image or Shooting and Bouncing Rays techniques, computes the channel impulse response (Figure 2.9 – a,b) that is passed through a raised cosine low-pass-filer to create the channel profile including the DP and the rest of multipath (Figure 2.9 – a,b) .

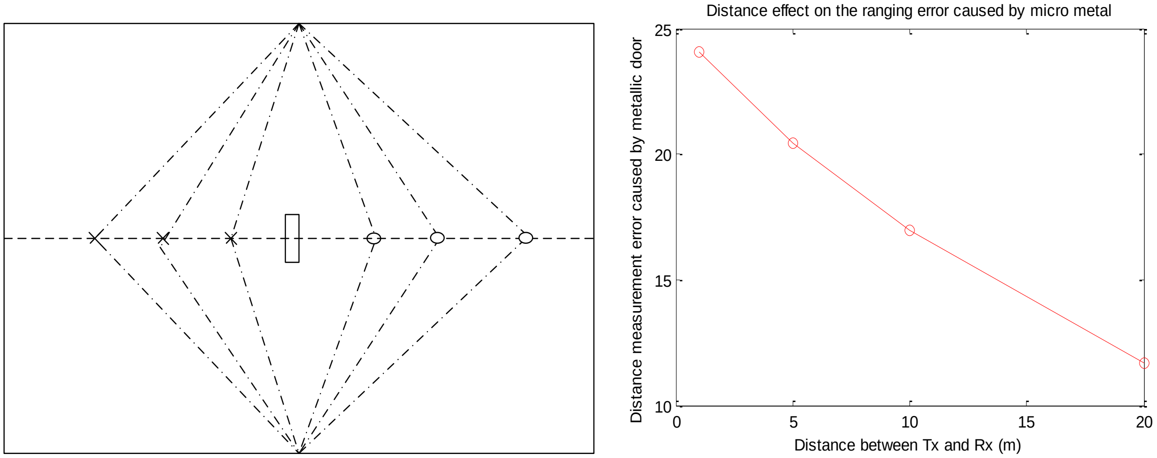

Figure 2.8 RT simulation scenario and ranging error versus distance.

For specific examples provided in Figure 2.9, the bandwidth of raised cosine filter is chosen as 200 MHz, first path ToA of unfiltered radio channel (RT) captures 9.5 ns, and first path ToA of filtered radio channel (Raised Cosine) is calculated for 10.2 ns. The measured distance is computed for 3 m, and DME is calculated for 0.15 m.

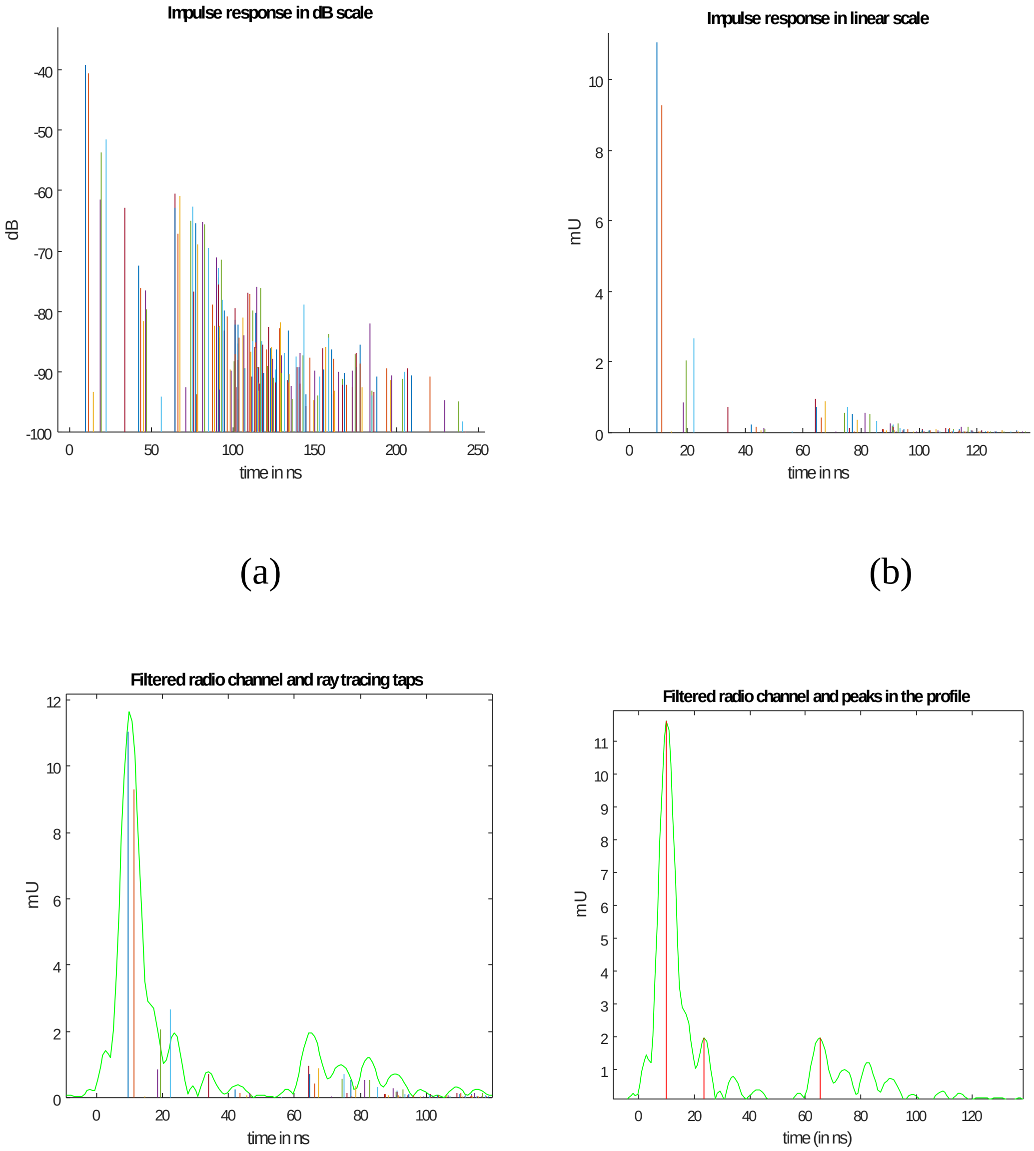

(a)

(b)

(c)

(d)

Figure 2.9 Flow diagram of process for generating RT channel profile.

2.5.2 EM Computational Method

The arrival of high power computers has provided the opportunity to solve Maxwell’s equations in an intense and interesting way. The part of electromagnetics that deals with numerically solving the potentials and field components in time and frequency domain is known as electromagnetics (EM) computational methods. The method provides a relatively fast approach to simulation and modeling of RF propagation in a complex media. The performance of applications that operate based on EM computational methods has improved over the years pertinent to recent enhancement in computational resources (i.e. CPU, memory) and optimization of those computational algorithms [67]. In general there are finite difference (FD) – normally in time domain, finite element method (FEM), and boundary element method (BEM) which are referred to as the method of moment. The FD methods involves discretization of Maxwell’s equations in differential form for field components on a structured grid of points (Figure 2.10 - a). In particular the finite-difference-time-domain (FDTD) perform very efficient as their algorithm require few operation per grid points. As a result of one of the widespread methods in the area of propagation of microwaves. The drawback of FDTD method is the fact they only perform well on uniformed structured grid which calls for boundary approximate to align with the grids [68]. The operational philosophy behind FEM method involves division of computational region into unstructured grids called elements, typically triangle in 2D or tetrahedral in 3D but pyramid, prism and cube are also possible, that can be used for geometrically complex boundaries and structures (Figure 2.10 – b). An element consist of nodes and boundaries and a collection of elements stablish a mesh. The performance related to FEM computation is relatively slower in time domain calculation and it is mainly used for time-harmonic problems and a standard procedure for eddy current calculations [69]. The MoM algorithm operates based on discretization of Maxwell's equations in integral form with surface current and charges as unknown parameters and a result the MoM algorithm performs better for problems that involves simulations with small structural surfaces or open environments (Figure 2.10 – c). Lastly, The MoM method is a good candidate for scattering problems [67].

In the past EM computational method and in particular FDTD has been used to analyze the wireless channel profile for telecommunication purposes. The applicability of EM computational method simulation software in respect to ToA-based indoor and human body localization is based upon the fundamental philosophy

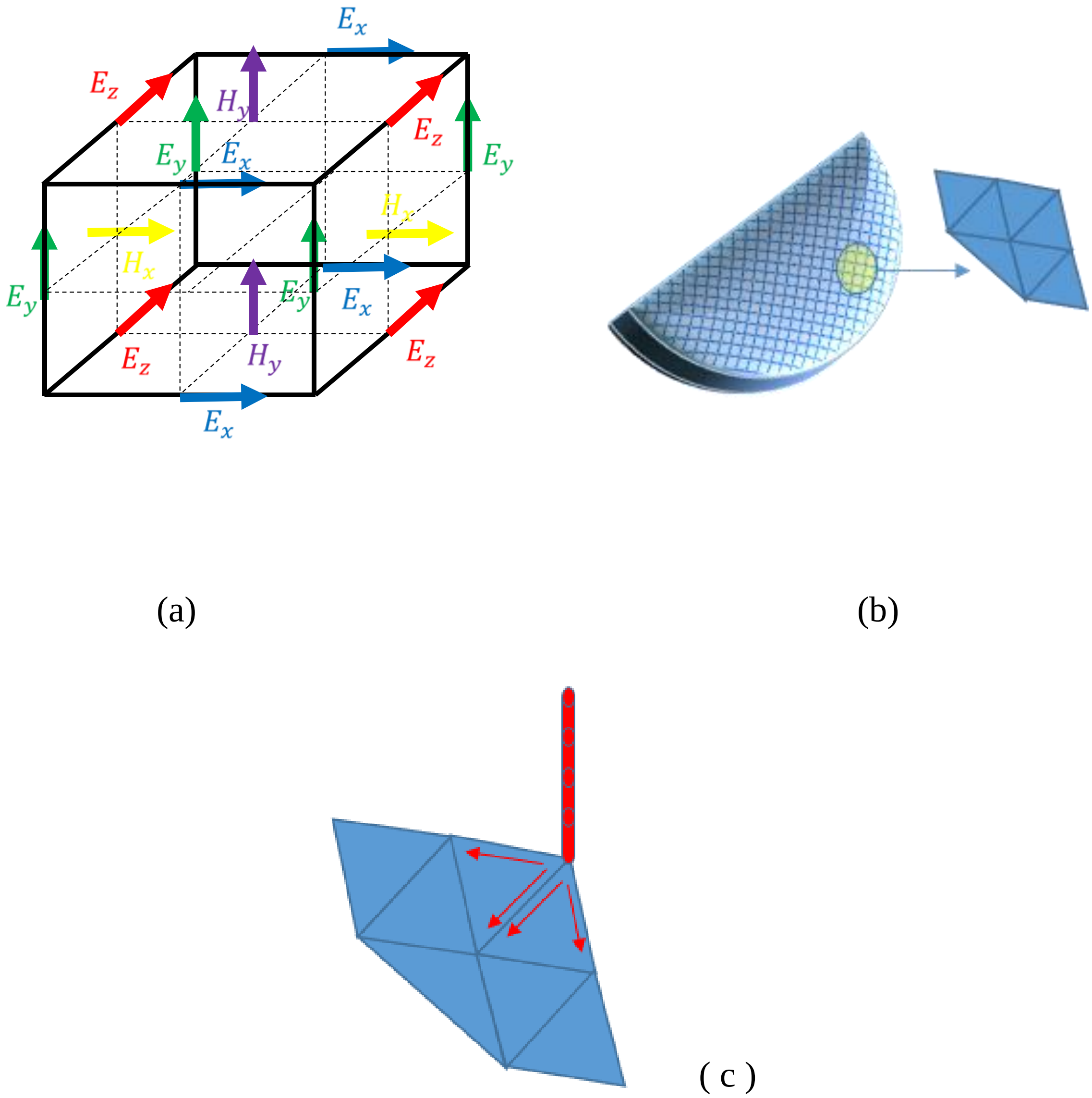

(a)

(b)

(c)

Figure 2.10 (a) FDTD structural grid with electric and magnetic points (b) FEM tetrahedral 3D structure (c) Source and surface discretization for MoM .

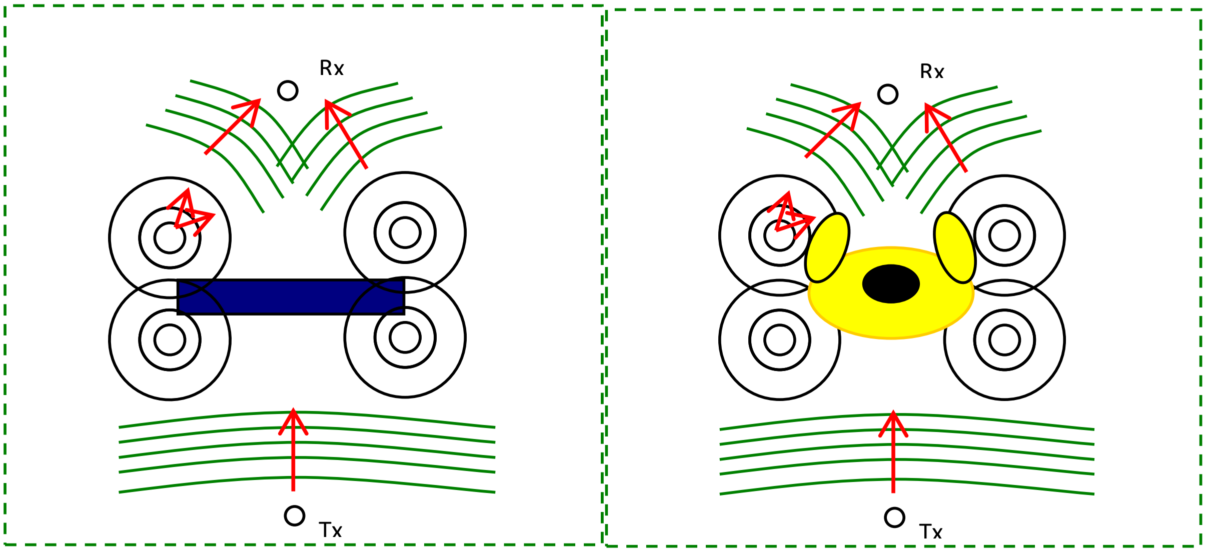

Figure 2.11 (a) Diffraction around micro-metals (door) (b) Diffraction around human body.

of simulation of DP behavior in terms of field point excitation ($\vec{H}$ and $\vec{E}$) , currents and charges between the antenna pair in the simulation environment. A controlled simulation environment will provide an ideal scenario where we can capture the effect of surrounding object (i.e. diffraction in the proximity of micro-metals and human body, Figure 2.11- a, b) excluding the multipath effects from the undesired entities (i.e. reflection from walls) within the simulation environment. The user interface of a typical Ansyst HSSS software package which is FEM solver is provided in Figure 2.12. It depicts a computational domain consists of two dipole antenna in the proximity of metallic door.

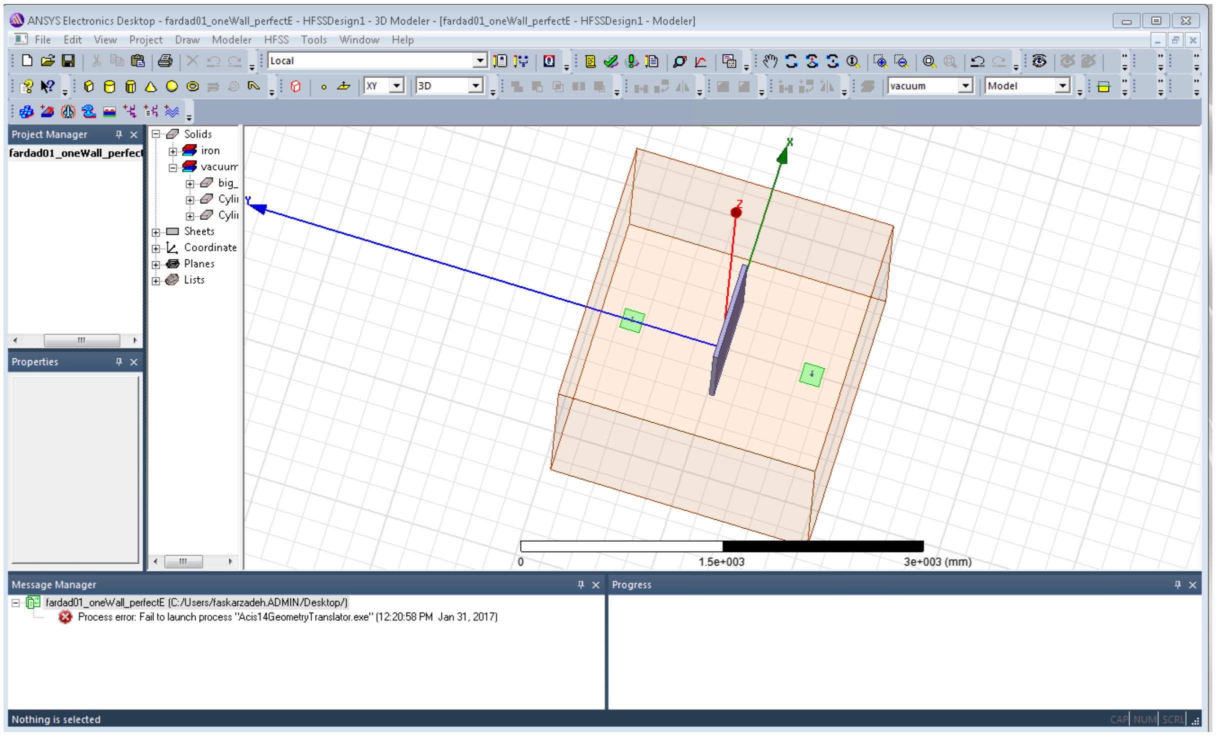

```
fardad01_oneWall_perfectE (C:/Users/faskarzadeh.ADMIN/Desktop/)
    Process error: Fail to launch process "Acis14GeometryTranslator.exe" (12:20:58 PM  Jan 31, 2017)
```

Figure 2.12 Ansyst HFSS user interface for a propagation scenario antenna pair are located in the proximity of a metallic screen.

2.5.3 Analytical UTD Ray Theory

In 1953 Kirchhoff provided Kirchhoff-Huygens approximation, which claims fields reaching any mathematical surface between a source and a receiver can be thought of as producing secondary point sources on the surface that in turn generate fields [70]. This was the start of what we can refer to as GTD era as an extension of Geometrical-Optics (GO), when the diffraction phenomena is considered in the shadow regions [60][61].

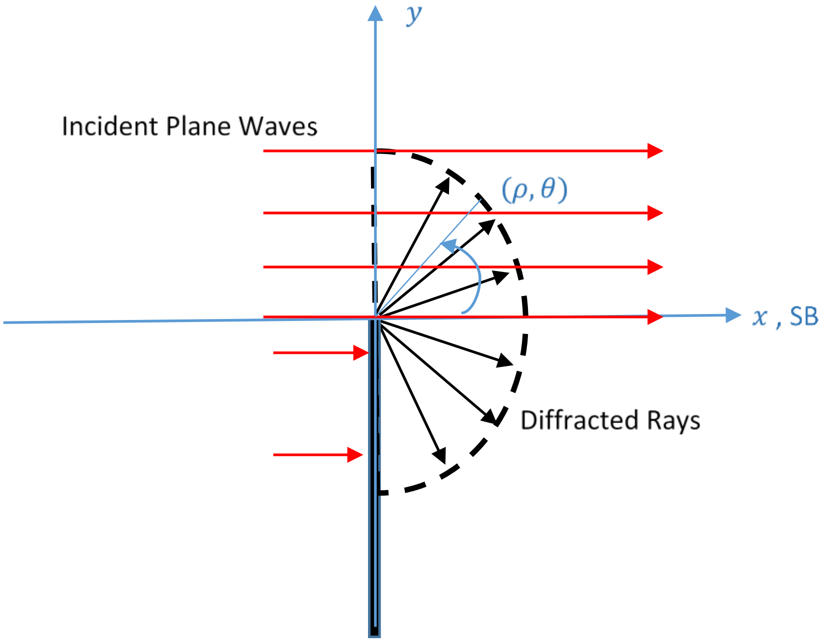

Figure 2.13 Diffraction on plane waves by an edge.

Figure 2.13 depicts a scenario that incident plane waves are diffracted by the conductor edge and start emanating as cylindrical waves both in and outside the shadow region that is reflected by field equation (2.6) at any distance ρ and angle of θ from the Shadow Boundary (SB).

$$E_{GTD} = E_{G0}U(\theta) + E_D \tag{2.6}$$

In this formula, the $U(\theta)$ is simply a unit function that helps with extension of model to GTD. The E_{GO} is the incident plane wave and $E_D$is the field in the shadow region that depends on diffraction coefficient $D(\theta)$.

$$E_{G0} = E_0 e^{-jkx} \tag{2.7}$$

$$E_D = E_0 e^{-j\pi/4} \frac{e^{-jk\rho}}{\sqrt{\rho}} D(\theta) \tag{2.8}$$

Diffraction coefficients for the absorbing screen is the same for both possible polarization of Transverse-Magnetic (TM) or Transverse-Electric (TE) electric fields [71] as the orthogonal polarization will no couple , and scalar Kirchhoff approximation can be used for complex amplitude of diffractions [70][72].

Absorbing screens, which is realistic scenario in many wireless problems, avoids added complexity required to count for polarization [80]. This is contrary to situations a conducting object (micro-metallic or human body) is interfering the propagation field and both TM and TE should be considered in order to compute the diffraction coefficients.

It was the use of Kirchholf-Huygens approximation (evaluation of field distortion) that led to physical signature of Fresnel Zone [70] presented in Figure 2.14. This helps with localization phenomena of propagation in wireless applications and reflects on significant of perturbation of direct wave by scatter object in this zone.

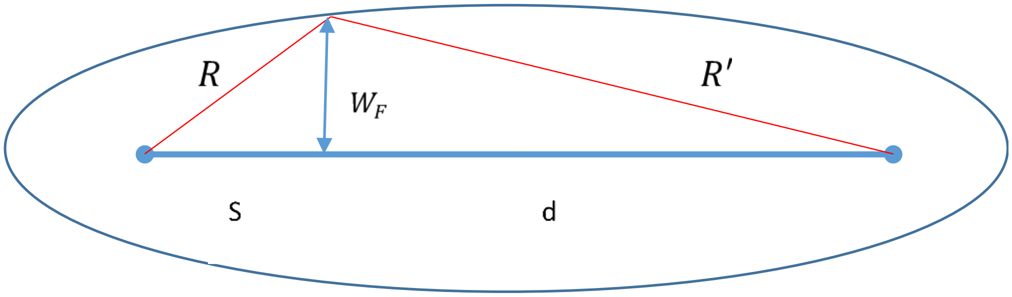

Figure 2.14 Fresnel Zone for localization phenomena of propagation in wireless applications.

The Fresnel zone is represented by equation (2.9), where R and R' are the distance of antenna pair from the nth Fresnel Zone border and λ is the wavelength of the transmitted signal.

$$(R + R') - (s + d) = n\frac{\lambda}{2} \tag{2.9}$$

First Fresnel zone is usually of interest for wireless communication applications as it provides less complexity, and once the problem is solved in this region helps with expanding the approach for the larger zones. In this thesis we use the first Fresnel zone to capture the significant of propagation in modeling and estimation of DP.

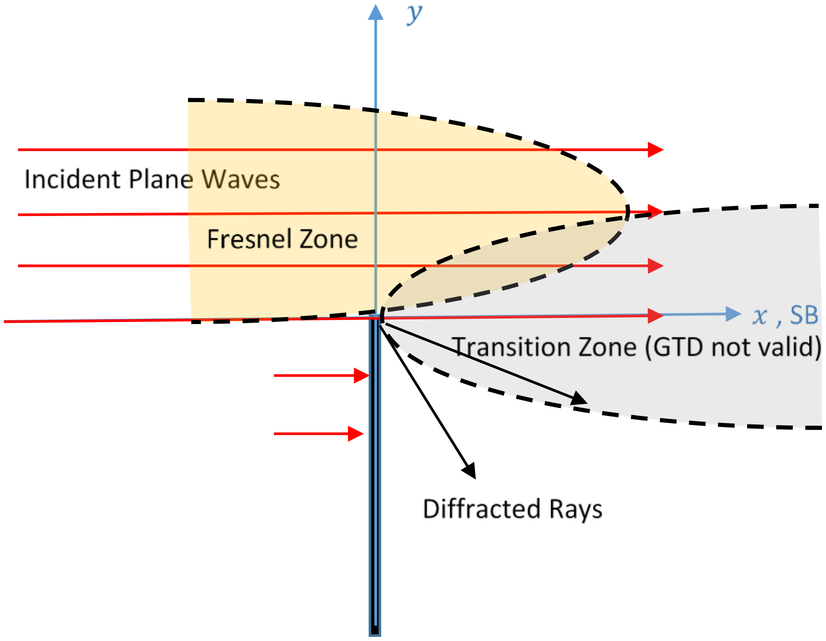

Figure 2.15 Transition zone for localization phenomena diffraction.

The Fresnel zone also applies to the diffracted rays as they are considered a secondary field source emanating from the diffraction point. The variation of field power around the SB of this region is highest from illumination into the deep shadow region [18] , and as a result referred to as transition region. The half-width (W_F) of transition region for a receiver located about the shadow boundary is the same as the width of the first Fresnel zone when the receiver I located on the shadow boundary. W_F for the nth Fresnel zone [73] is shown in equation (2.10).

$$W_F = \sqrt{n \frac{\lambda RR'}{R + R'}} \tag{2.10}$$

The GTD properties that is discussed in equation (2.6) is not valid in the transition zone as it cannot handle the large field discrepancies observed that region. This lead to definition of UTD ray theory [62][80] in equation (2.11) , that is broadly used in this thesis. The $F(S)$ is referred to as transition function, $D_{GTD}\ (\theta)$ is the regular diffraction coefficient outside the transition, which its values in the transition region ($D_{UTD}\ (\theta)$) is defined as following:

$$D_{UTD}\ (\theta) = D_{GTD}\ (\theta)\ F(S) \tag{2.11}$$

The transition function $F(S)$ is further defined in equation (2.12), and its value reaches unity outside the transition zone. The parameter S can be defined appropriately based on the geometry of scatter and the type of UTD model used for the computation.

$$F(S) = 2j\sqrt{S}\, e^{jS} \int_{\sqrt{S}}^{\infty} e^{-ju^2} du \qquad (2.12)$$

The definition of diffraction coefficient heavily relies on the properties of UTD model, and the field polarization in the proximity of conductor objects, where the diffraction happens. In the upcoming chapters of this thesis we discuss in details the UTD models utilized for micro-metals and human body. Out of those, the models used for micro-metals are relatively straight forward and easy to follow based on what is already described in this chapter. However, the UTD models used for human requires some background that will be the subject of this session going forward.

The UTD of diffraction for scattering by a cylinder has evolved from fundamental work provided by Fock [81], Wait [82], Kouyoumjian , Logan and many more [61]. Weston obtained the back-scattered electromagnetic field from a perfectly conducting sphere when the incident field is a plane wave [83] .Pathak introduced UTD for plane wave scattering by a cylinder, and later Pathak et. al. [83] to UTD diffraction of any electromagnetic waves by a smooth convex surface based on applicability of Pekeris and transition region functions (Figure 2.16).

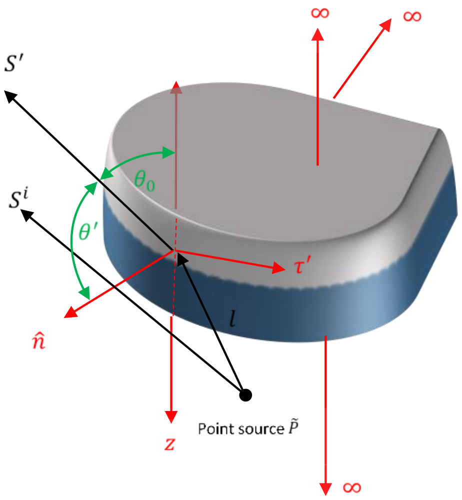

Figure 2.16 Ray path associated with problem of scattering of an obliquely incident plane wave by a smooth convex surface.

The UTD ray theory of smooth convex surfaces are not uniform in a sense different formulation are used, depending on positioning of source and the field points on and off the surface [80]. The different cases are referred to as coupling, radiation and scattering problems. When both the source and the field points are located on the smooth convex surface the coupling is formulated based on Fock functions v and u , and for cases source and field points are near the surface the problem is formulated based on Fock functions F_S, F_h . When one of the source and the field points are on the surface the problem is commonly referred to as radiation and is formulated based on $g, \tilde{g}$ functions. When both the source and the field are off the surface, the problem referred to as scattering and is formulated in term of Pekeris functions. Application of uniform scattering approach provided Pathak et. al. [83] to the line source illuminating a circular cylinder is adequately described by McNamara et. al. in [80] as reflected and diffracted fields (Figure 2.17) , where both fields have an associated coefficient formulated as two parts. The first part describes the Fresnel diffraction, and the second part model the effect of creeping waves on the surface of cylinder. It described the creeping waves adds in phase with diffracted field and they are caused by the generation of the Fock currents on the surface of scatterer [81]. This confirms the fact the scattered field from convex surfaces manifest less attenuation in compare to sharp obstructions dependent on the field polarization and the conductivity of the object.

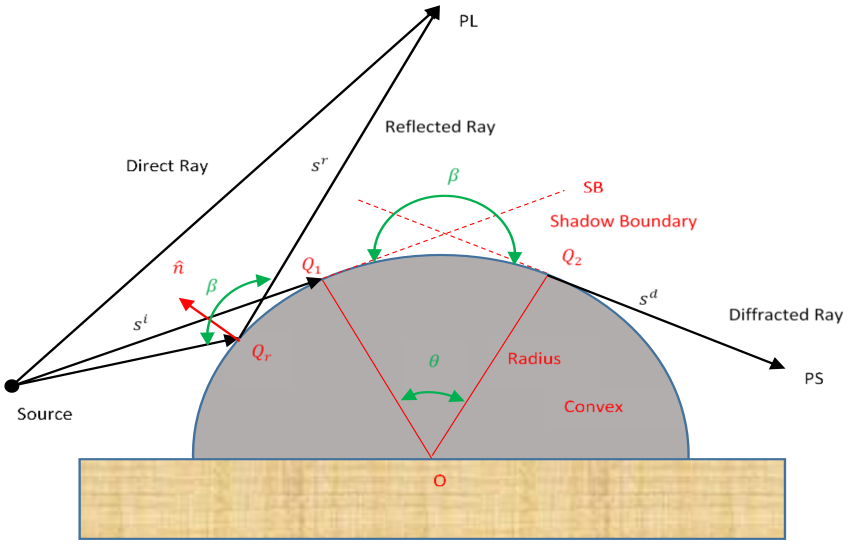

Figure 2.17 Ray nature and path geometry for the case of scattring by single convex surface .

In the next chapter of this thesis we discuss analysis of effects of micro-metals on ToA-based indoor localization. FDTD computational methods is used to model DP, and the computational model is validated with UWB measurement. This is the starting point to computational models offered in this dissertation to model DP in ToA-based indoor and human body localization.

Chapter 3 Analysis of Effects of Micro-metals Using FDTD

3.1 Introduction

Throughout the previous sections we explained how TOA-based techniques can suffer large ranging errors, mainly because of the effects of micro-metals and the human body around the transmitter and receiver. We discussed, experiments that were conducted at CWIN lab in WPI to analyze and compare the results of TOA-based measurements with ray-tracing results. Measurements were made with the receiver placed in the vicinity a macro-metallic object (*i.e.,* metallic chamber in CWINS lab or the elevator along the corridor). The measurement results clearly exhibited a UDP condition due to the blocking of the first path [10]. The large discrepancy that was observed between ray-tracing and measurement results led the research team to examine the possible influences of micro-metallic objects such as doors or windows in those areas. Although introducing metallic objects to the ray-tracing map improved the discrepancies in some cases, it did not significantly affect the result of 2D ray-tracing.

To better understand the effects of micro-metals in ToA-based localization, a series of experiments was conducted to analyze and observe the behavior of the DP in close proximity to a metallic door. This effort strived for a simulation environment which could predict the DP behavior in the present of diffraction and as a result the applicability of full-wave FDTD EM methods as an alternative was investigated - which is the subject of this chapter.

Previously FDTD applications were used to model the indoor propagation problem but its focus is mainly on the telecommunication applications rather than localization. In telecommunications, the delay spread of the wireless channel profile is important while ToA-based localization applications call for modeling of the DP component which is directly related to the ranging error. In communication and modem performance evaluations, the system designer is usually concerned with the overall performance over typical areas or typical buildings, and statistical models usually serve the purpose reasonably well. In other applications such as microcellular or indoor installations, where proper sitting of antennas is an important issue, building-specific radio propagation models offer a more precise tool for determining optimum antenna locations. Building-specific radio propagation models are based on direct solution of the radio propagation equations with boundaries defined by a map of a coverage area or the layout plan of a building. The technique known as RT provides a simple approximation for analysis of radio wave propagation. Another approach is numerical solution of the Maxwell equations using the FDTD technique. Although ray-tracing models can efficiently predict radio propagation characteristics for indoor and outdoor applications, these techniques are only approximations to the direct solution of electromagnetic wave propagation equations. The ideal method of simulating radio propagation is to solve Maxwell's equations numerically. The numerical solution of these differential equations over a designated area requires selection of a number of points at which the solution is to be determined iteratively.

The FDTD method is probably the most straightforward and widely used method for numerical solution of Maxwell's equations. With this method, Maxwell's equations are approximated by a set of finite-difference equations. By placing the electric and magnetic fields on a staggered grid and defining appropriate initial conditions, the FDTD algorithm employs the central differences to approximate both spatial and temporal derivatives, and it solves Maxwell's equations directly. The distribution of electric and magnetic fields over the whole grid is calculated incrementally in time; and when the simulation is finished, the propagation characteristics are known at every location in the area under study.

A more computationally efficient form of traditional FDTD method used for communication application has also been applied previously to indoor areas, showing significant improvement in accuracy over the rectangular FDTD algorithm. The computational time needed for this method was comparable to available three-dimensional ray-tracing algorithm at that time. A point-to-point comparison between predicted and measured power in all locations for two-dimensional and three-dimensional ray-tracing and for the FDTD models showed that both ray-tracing models and the FDTD model were all in good agreement with the measurements. However, ray-tracing provides a more accurate estimate of the power based on the standard deviation calculated against the measurements [4].

In the past, a number of research projects have been carried out using one or more computational techniques to model Body Area Network channels. Among these, the most popular were FDTD, used by the National Institute of Standards and Technology (NIST) [39], and MoM used by the IEEE P802.15 working group [40]. Both of these projects involved the modeling of the power delay profile of the human body channel for medical communication purposes, and not for TOA-based localization. CWIN lab at WPI have followed a 3D human body model based on applicability of a full-wave MoM simulator (HFSS) to analyze the DP phenomenan for 900 MHz with 100 MHz bandwidth [41]. They have also taken avdatanges of Ansoft HFSS sfoware , a FEM solver, to confirm the accuracy of capsule endoscopy localization in human body [52][54][53] . Zhao et al. in [22], have adopted a hybrid sub-band FDTD to validate analyze UWB characteristics of creeping waves around human body.

To achieve our goal of predicting ranging error in proximity of micro-metals, a comparative study is made of the applicability of different commercial EM full-wave software packages, and the 2D FDTD solver developed for our purpose [85].

The research team initially was inclined to utilize Ansoft HFSS and CST FDTD simulation software, however the extensive computational time required in using these packages led the group to use a custom MATLAB 2D FDTD software package [86] designed and developed for academic purposes to expedite the analysis.

We solve three canonic problems of voltage time response identification for an indoor monopole antenna link, with open (free space and door frame) and closed metal door cased in a wall. We then compare the results of the FDTD simulation to the channel profiles obtained from real-time frequency-domain measurements. The measurement setup was designed to match the center frequency of 1GHz via bandwidth of 500 MHz compare to characteristics of the simulation based on 500 MHz frequency so a fair comparison could be performed. The measurement system consisted of a vector network analyzer with two omnidirectional monopole antennas.

The rest of the chapter is organized as following; in sections 3.2 we introduce FDTD computational method, section 3.3 focuses on experimental procedures related to a metallic door and in particular 3.3.1 discusses the measurement campaign and 3.3.2 covers the simulation configurations associated to each experimental scenarios. Section 3.4 discusses comparison of simulation and empirical measurement results, and finally section 3.5 concludes the chapter.

3.2 FDTD Method

In 1966 Yee [87] proposed a technique to solve Maxwell's curl equations using the finite-difference time-domain (FDTD) technique. Yee's method has been used to solve numerous scattering problems for microwave circuits, dielectrics, and electromagnetic absorption in biological tissue at microwave frequencies. Since it is a time-domain method, solutions can cover a wide frequency range with a single simulation run. The FDTD method belongs to the general class of grid-based differential time-domain numerical modeling methods. The time-dependent Maxwell's equations are discretized using central-difference approximations to the space and time partial derivatives. The resulting finite-difference equations are solved in either software or hardware in a leapfrog manner: the electric field vector components in a volume of space are solved at a given instant in time; then the magnetic field vector components in the same spatial volume are solved at the next instant in time; and the process is repeated over and over again until the desired transient or steady-state electromagnetic field behavior is fully evolved.

Let us consider a two-dimensional *transverse magnetic* (TM)-to-z field (Electric and Magnetic fields are perpendicular to the Z-axis) as depicted in Figure

3.1 in proximity of metallic aperture. This figure presents a classic scattering/radiation problem where both the radiating and receiving antennas (dipole or monopole) are vertical. The TM to z field can be illustrated by Maxwell's equation (3.1), (3.2) and (3.3):

$$\frac{\partial E_z}{\partial t} = \frac{1}{\varepsilon}\frac{\partial H_y}{\partial x} - \frac{1}{\varepsilon}\frac{\partial H_x}{\partial y} - \frac{\sigma}{\varepsilon}E_z \tag{3.1}$$

$$\frac{\partial H_x}{\partial t} = -\frac{1}{\mu}\frac{\partial E_z}{\partial y} - \frac{\sigma^*}{\mu}H_x \tag{3.2}$$

$$\frac{\partial H_y}{\partial t} = \frac{1}{\mu}\frac{\partial E_z}{\partial x} - \frac{\sigma^*}{\mu}H_y \tag{3.3}$$

Here *E* and *H* are electric and magnetic fields, respectively; σ and σ^* are the electric and magnetic conductivities (losses), real or artificial. The standard Yee 2-2 FDTD scheme represented in equation (3.4), (3.5) and (3.6) can be implemented [88] to operate on a staggered grid that is shown in Figure 3.2 for $n = 1,2,\ldots,N_t - 1 \quad k = 1,2,\ldots,N_x + 1 \quad m = 1,2,\ldots,N_y + 1$. In the aforementioned equations, E and H are discretized in time and space as the initial excitation travels through the computational area.

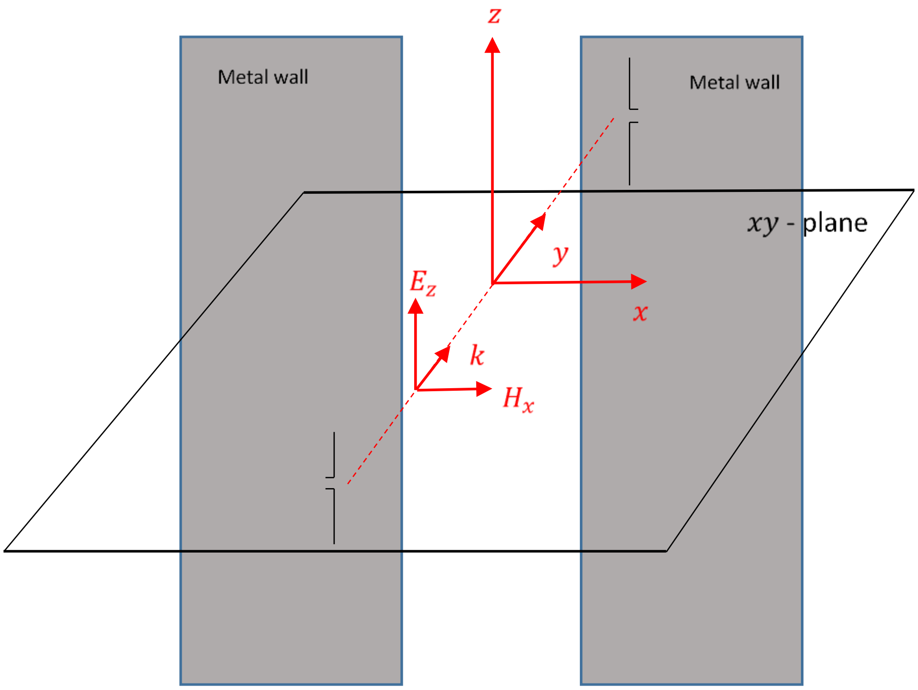

Figure 3.1: Two-dimensional traverse magnetic to Z-field.

$$E_z(t,z) \rightarrow E_z\left((n-1)\cdot\Delta t,\ (k-1)\cdot\Delta x,\ (m-1)\cdot\Delta y\right) = E_{z\,k,m}^{\ n} \tag{3.4}$$

$$H_x(t,z) \rightarrow H_x\left(\left(n-\tfrac{1}{2}\right)\cdot\Delta t,\ (k-1)\cdot\Delta x,\ \left(m-\tfrac{1}{2}\right)\cdot\Delta y\right) = H_{x\,k,m+1/2}^{\ n+1/2} \tag{3.5}$$

$$H_y(t,z) \rightarrow H_y\left(\left(n-\tfrac{1}{2}\right)\cdot\Delta t,\ \left(k-\tfrac{1}{2}\right)\cdot\Delta x,\ (m-1)\cdot\Delta y\right) = H_{y\,k+1/2\,m}^{\ n+1/2} \tag{3.6}$$

In equation (3.4) , (3.5) and (3.6), n represents the imaginary layer number that is calculated in the time domain and shown in Figure 3.2 as layer 0 and 1 (layers of electrical fields separated by Δt). The middle layer is represented as imaginary layer (n = 0.5). On the other hand, m and k represent the position of electrical or magnetic fields along the x or y axis of any of imaginary time domain layers. For example, (k = 1) represents the position of the second electrical field on (n = 0) layer from the t axis and (k = 0.5) represents the position of the first magnetic field on the (n = 0.5) layer from the t axis. Substitution of equation (3.4), (3.5) and (3.6) into the fundamental Maxwell equations that are shown in (3.1), (3.2) and (3.3) results in discrete formulas of (3.7) , (3.8) and (3.9):

$$\frac{E_{z\,k,m}^{\,n+1}-E_{z\,k,m}^{\,n}}{\Delta t}=\frac{1}{\varepsilon_{k,m}}\frac{H_{y_{k+1/2,m}}^{\,n+1/2}-H_{y_{k-1/2,m}}^{\,n+1/2}}{\Delta x}-\frac{1}{\varepsilon_{k,m}}\frac{H_{x\,k,m+1/2}^{\,n+1/2}-H_{x\,k,m-1/2}^{\,n+1/2}}{\Delta y}-\frac{\sigma}{2\varepsilon_{k,m}}(E_{z\,k,m}^{\,n+1}+E_{z\,k,m}^{\,n}) \tag{3.7}$$

$$\frac{H_{x\,k,m+1/2}^{\,n+3/2}-H_{x\,k,m+1/2}^{\,n+1/2}}{\Delta t}=-\frac{1}{\mu_{k,m+1/2}}\frac{E_{z\,k,m+1}^{\,n+1}-E_{z\,k,m}^{\,n+1}}{\Delta y}-\frac{\sigma^{*}}{2\mu_{k,m+1/2}}(H_{x\,k,m+1/2}^{\,n+3/2}+H_{x\,k,m+1/2}^{\,n+1/2}) \tag{3.8}$$

$$\frac{H_{y_{k+1/2,m}}^{\,n+3/2}-H_{y_{k+1/2,m}}^{\,n+1/2}}{\Delta t}=+\frac{1}{\mu_{k+1/2,m}}\frac{E_{z\,k+1,m}^{\,n+1}-E_{z\,k,m}^{\,n+1}}{\Delta x}-\frac{\sigma^{*}}{2\mu_{k+1/2,m}}(H_{y_{k+1/2,m}}^{\,n+3/2}+H_{y_{k+1/2,m}}^{\,n+1/2}) \tag{3.9}$$

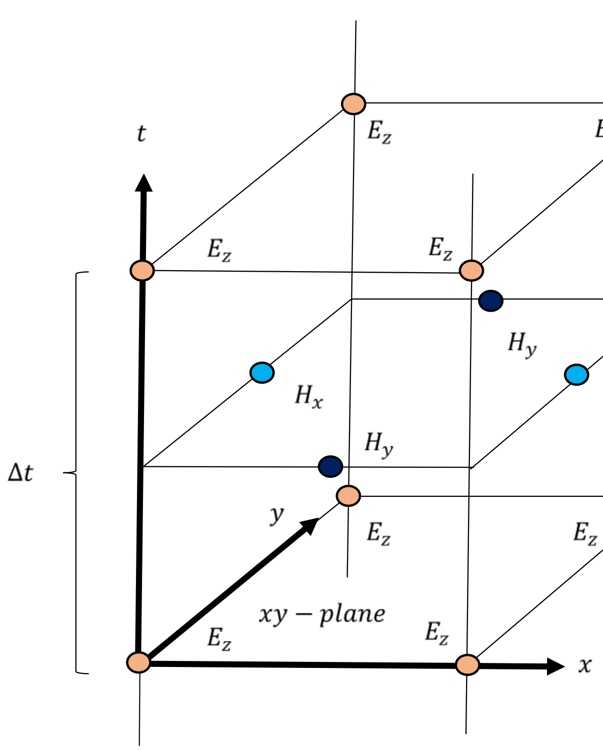

Figure 3.2: Standard YEE 2-2 FDTD scheme on a staggered grid.

These formulas are basically the core engine of any FDTD simulation software. Once we initialize the emanating electric and magnetic fields with the appropriate excitation values, a recursive call to these formulas, in time-domain, will predict electric and magnetic fields at any point within our computation space. From equation (3.7), (3.8) and (3.9) we can clearly see that a 2D version of such a simulation would only calculate electric and magnetic fields for two specific dimensions. To better understand a 2D FDTD simulation, one can visualize the simulation space as an imaginary plane. We can calculate fields, in time-domain, for any points located on this plane from the time an excitation emanates from the transmitter until it impinges upon the edges of the plane and the receiver point.

Metal and dielectric targets (walls, doors, etc.) are treated in a standard fashion [88]. The method can routinely handle electrically large structures on the size up to $200\lambda\times200\lambda$ in MATLAB and is fast. The computation time for the FDTD technique is proportional to the size of the area, and the addition of structural details does not affect the computation significantly. However, the number of nodes used for computation is related exponentially to the size of the area and the frequency of operation. The computational methods can provide the relationship between the layout of a building or an outdoor area and the detailed channel response in a specific location. Therefore, they can provide realistic estimates of the azimuthal distribution of rays received in a multipath environment.

3.3 Diffraction in Proximity of a Metallic Door

The structures shown in Figure 3.3 – a, b are used as an example to illustrate the scenarios that we are going to investigate. There is either an aperture - a door opening in a metal screen – see Figure 3.3 – a, or a metal scatterer - a door in a dielectric screen - see Figure 3.3 – b. A two dimensional (2-D) environment with transmitter Tx and receiver Rx polarized in direction perpendicular to figure are considered. In the latter case, the walls are dielectric with $\varepsilon_r = 12$ approximately.

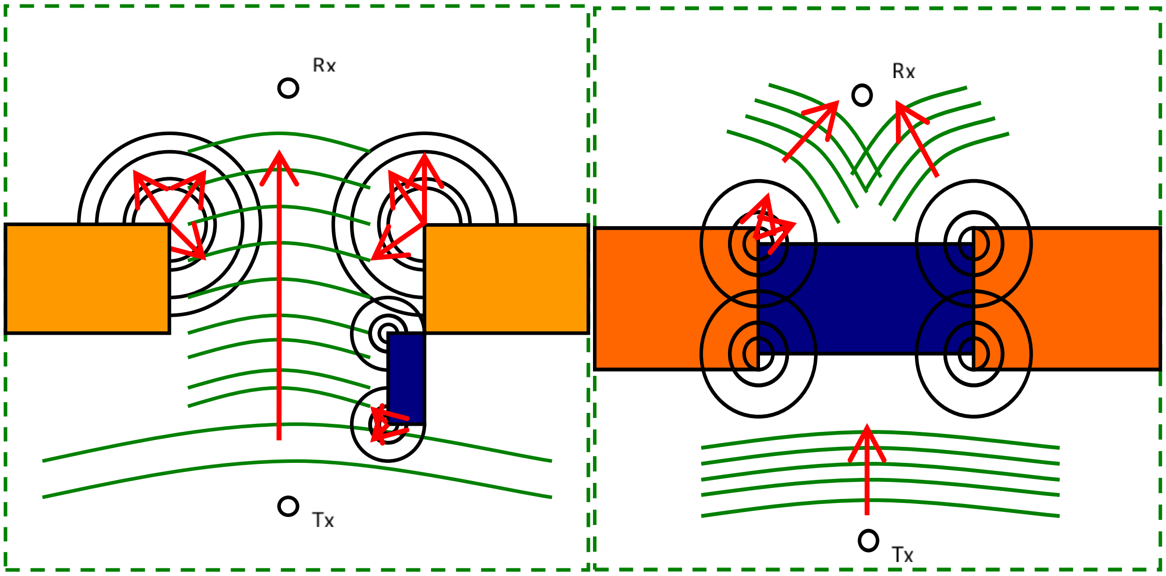

Figure 3.3 (a) Simulation of an open door in a metal screen (b) Simulation of a closed door in a dielectric screen.

3.3.1 Measurement Setup and Scenarios

The measurement set up consists of a dipole antenna pair with TM polarization. Each one of transmitter and receiver antenna are placed 1 m away from surface of a metallic door in dimensions of 1.21 m width, and 44 mm thickness assembled in a door frame for free-space, open-door and closed-door scenarios depicted in Figure 3.4. The measurement is taken by a vector network analyzer (Agilent E8363) operating at 1GHz, and sweeping 500 MHz bandwidth. The transmitter antenna is used as reference node and it is attached to tripod with the same height as receiver. During the measurement, S-parameters S_{21}, the transfer function of the channel, is measured by VNA in frequency domain with 1601 sample points. The receiver signal is transferred to time domain by inverse fast Fourier transform with a Hanning window applied to the time domain received channel profile to limit the sidelobe. The first peak can be detected by setting up proper threshold of the time domain signal strength and the propagation time of the first peak can be easily estimated. To guarantee the accuracy of the first path ToA, undesirable effects of cables, antennas, and other system components are removed through system calibration. The calibration process consist of connecting the test port cables of analyzer to form a thru configuration in order to capture the thru response of the system. The result of measurement provided in Figure 3.5, testifies to the 0.8 m DME when transitioning from a LoS condition in free-space and open-door scenarios to an NLoS and in particular UDP condition in a closed-door scenario. Upon closing the door, the first path will interfere by the conductor surface

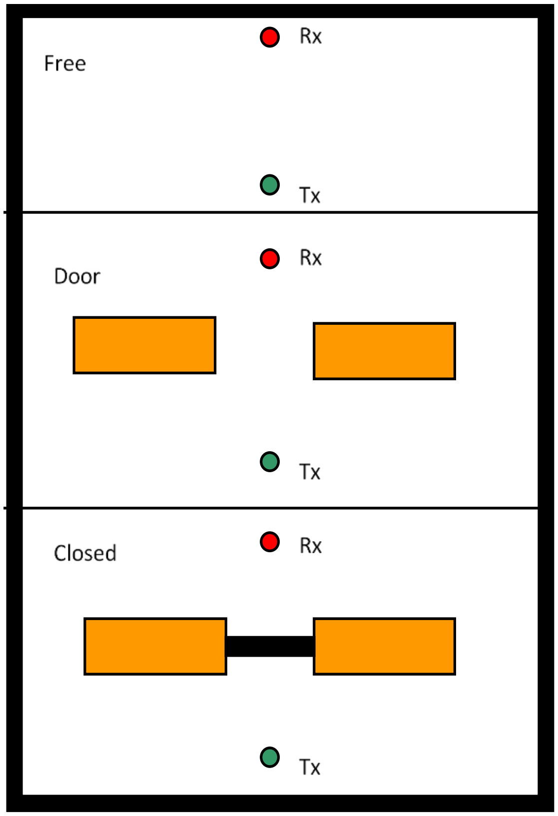

Figure 3.4 2 m antenna separation measurement for free-space, open-door and closed-door scenarios.

of metallic door resulting in blockage of DP and its diffraction by the edge of the door. It is safe to assume the DME that has been observed in the measurement campaign is as a consequence of diffraction phenomena influencing the first path in the proximity of a micro-metals such as this metallic door used in our experiment.

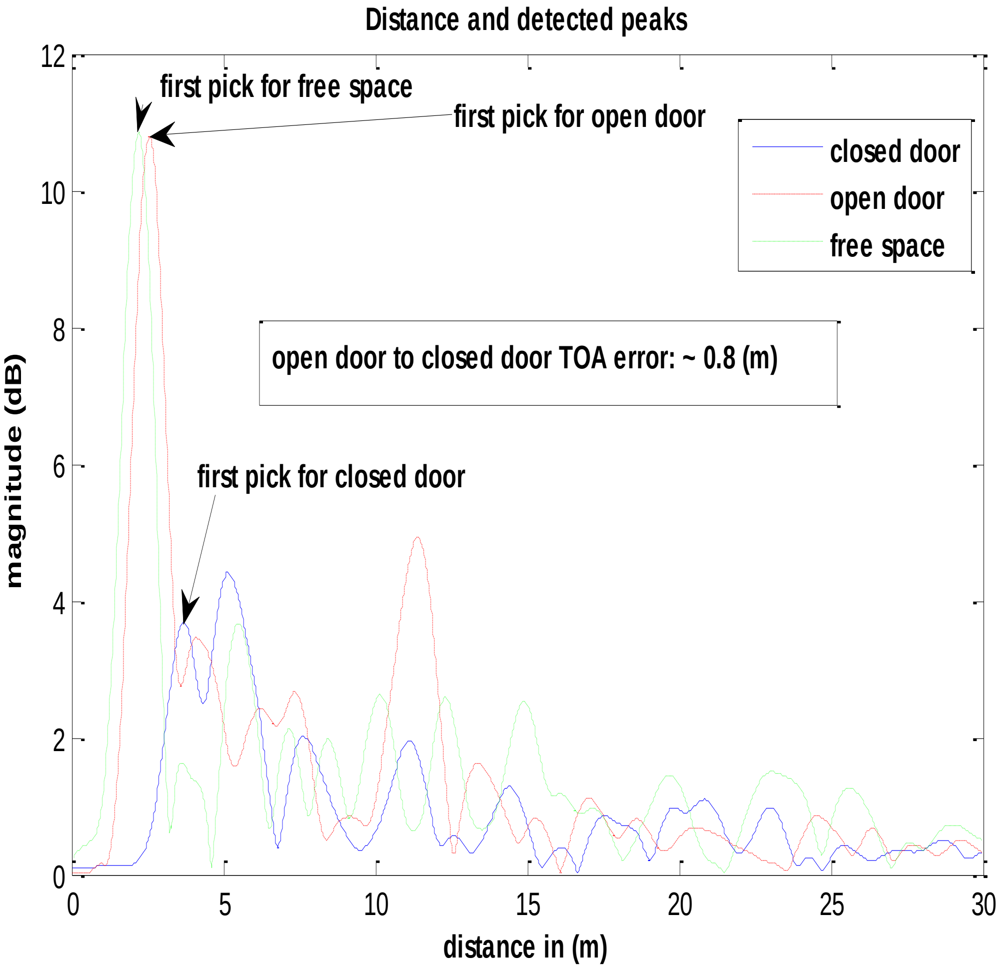

Figure 3.5 measurement results associate to free-space, open-door and closed-door scenarios.

3.3.2 2D FDTD Simulation Scenarios

Having outlined the theory of diffraction phenomena, we can now relate diffraction effect to each of the three scenarios depicted in Figure 3.4. In this part, we explain the simulation setup for each of those scenarios.

The very first scenario that we are going to discuss - which is the simplest one -is the free-space scenario which, transmitter Tx and the receiver Rx are located 2 m away from each other without the effect of the environment (Figure 3.6 and Figure 3.7).The other two scenarios are the ones that we are mainly interested in. There is either an aperture - a door opening in a metal screen, Figure 3.8- or a metal scattered - a metallic door in a dielectric screen - Figure 3.9. These figures present a two dimensional example with the transmitter and receiver polarized in the direction that is perpendicular to the figure plane.

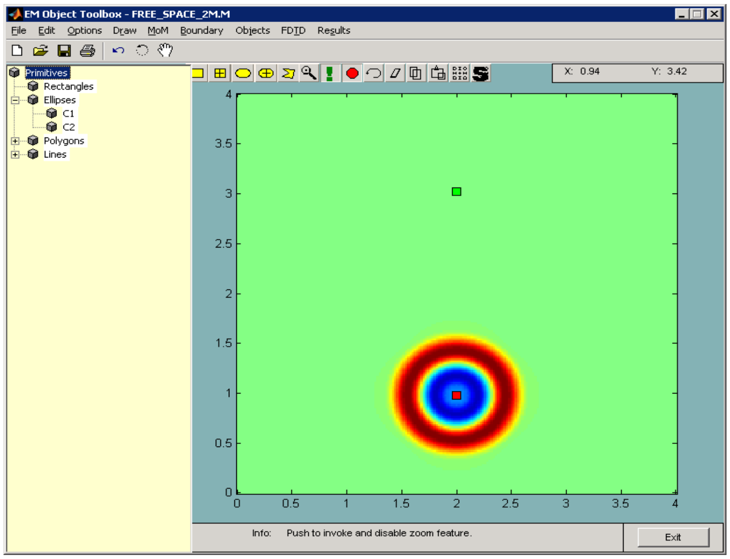

Info: Push to invoke and disable zoom feature.

Figure 3.6 Free space scenario, Initial excitation or 2 m separation of antenna pair.

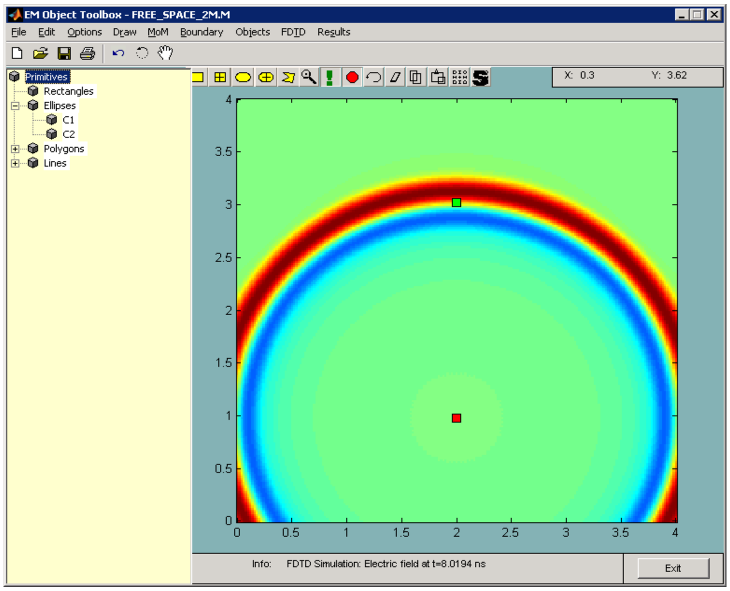

Info: FDTD Simulation: Electric field at t=8.0194 ns

Figure 3.7 Free space scenario, Initial excitation receiving at the Rx for 2 m separation of antenna pair.

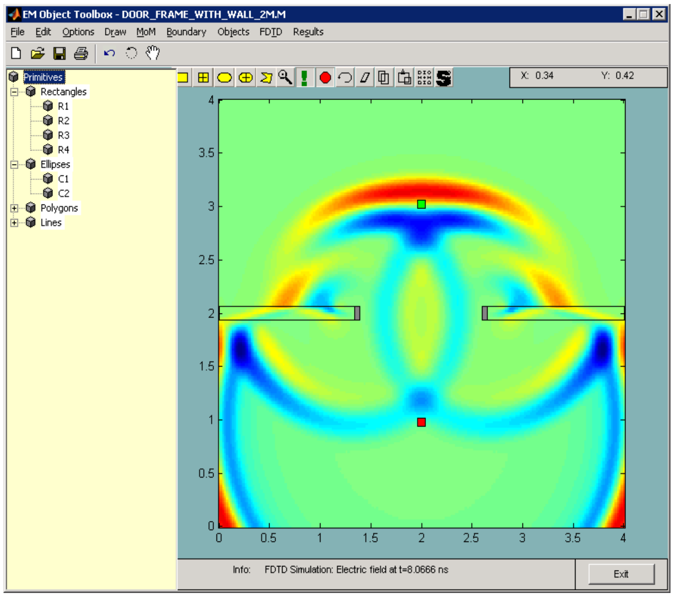

Info: FDTD Simulation: Electric field at t=8.0666 ns

Figure 3.8 Open-door scenario, 2 m separation of antenna pair in proximity of door frame.

In the open-door scenario, the walls are simulated as dielectric material with $\varepsilon_r = 12$ approximately and as shown in Figure 3.8, the signal emanates from the transmitter in free space through the dielectric walls, and is received at the receiver in the presence of the door-frame. On the other hand Figure 3.9 clearly shows the penetration of waves through the walls and the diffractions phenomena that is experienced on the edges of the metallic door in closed door scenario.

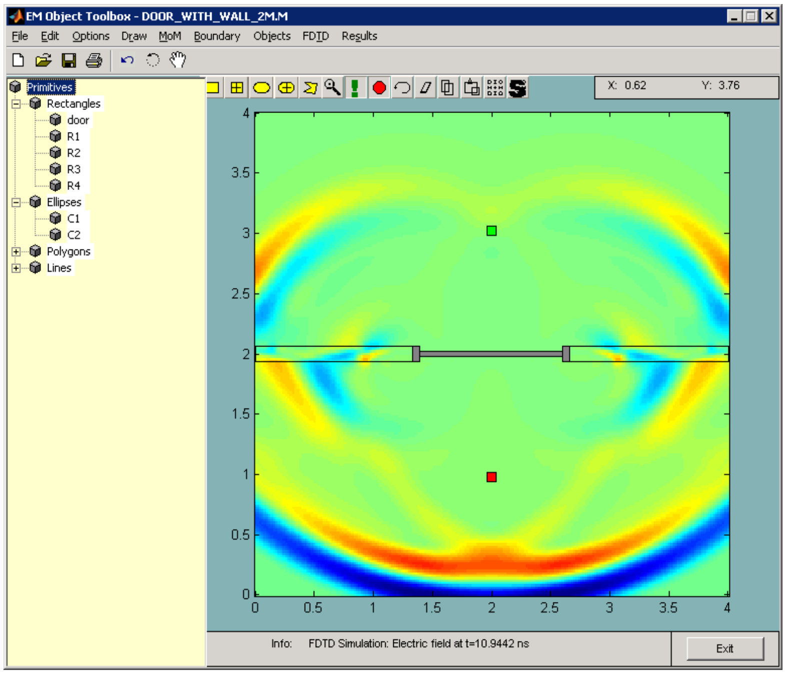

FDTD Simulation: Electric field at t=10.9442 ns

Figure 3.9 Closed-door scenario, 2 m separation of antenna pair in proximity of metallic door.

To set up our simulation environment, we configure the simulation area within relatively small dimensions of 4 m x 4 m with perfectly-matching-layer Layer (PML) walls surrounding the computational region and two antennas (a Transmitter and a Receiver) separated by 2m. The internal material of the box (2D square in our simulation case), are simulated as free space (μ_0, ε_0). To virtualize a door frame with two antennas on each side of it, we configure two walls with metallic sides away from each other by introducing an open space between transmitter and the receiver. The screening walls are simulated with dielectric constant of ($\varepsilon_r = 12$) and thickness of 12 cm. The metallic sides are provided with a thickness of 5 cm. The actual metallic door is simulated in dimensions of 1.21 m width and 44 mm thickness.

Figure 3.6 - Figure 3.9 depict a snapshot of E-field wave propagation from the transmitter to the receiver antenna. In our simulation environment the small red square represents the transmitter (Tx) and the green square represents the receiver (Rx). A PML boundary is used to insure very little reflected energy from the truncated mesh. PML is a layer of artificial highly absorbing material surrounding the computational region. The PML is further terminated with Perfect Electric Conductor (PEC) surface.

3.4 Comparison of Computation with Empirical Results

The purpose in conducting a free-space scenario experiment is to prove the accuracy of our simulation result, while the open-door scenario serves to demonstrate how well the simulation approximates an ideal condition.

Throughout our analysis emanating voltage time response is represented by the first peak and the received voltage time response is represented by the second peak. Using results derived from Figure 3.11 and Figure 3.10, we see that the simulation provides us with a 1.99 m distance between the transmitter (Tx) and receiver (Rx) antennas. Comparing these results with the actual measurements campaign that are derived from Figure 3.5 shows that, the simulation and measurement results are in good agreement. We can clearly see the effect of the environment in our measurement campaign (considering second and third multipath reflections, *etc*.), which are not captured in our simulation results due to the PML condition and the impulse signal nature of the transmitter in our simulation. Such a simulation is an ideal environment since the surrounding walls have little effect on our results.

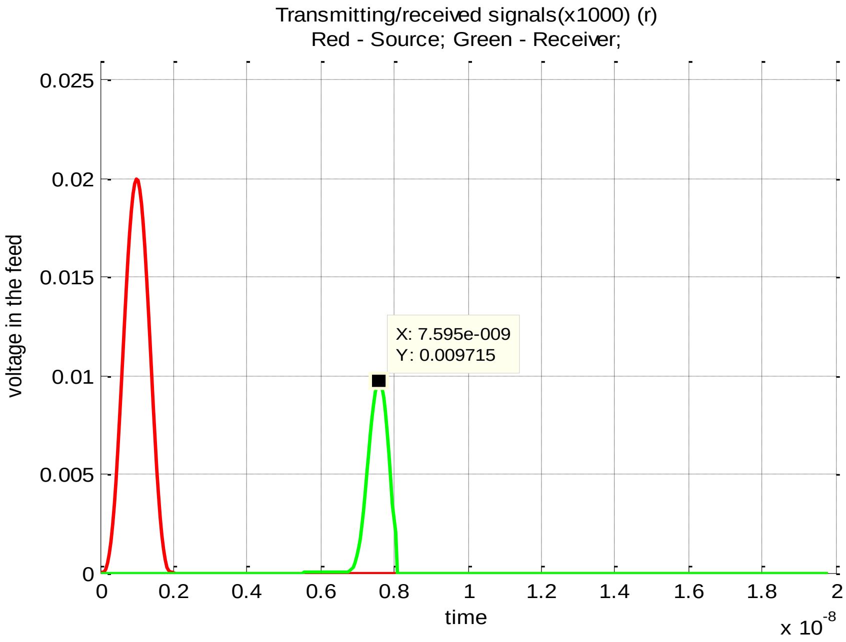

Figure 3.11 Voltage excitation (red) and voltage time-response (green) for free-space simulation.

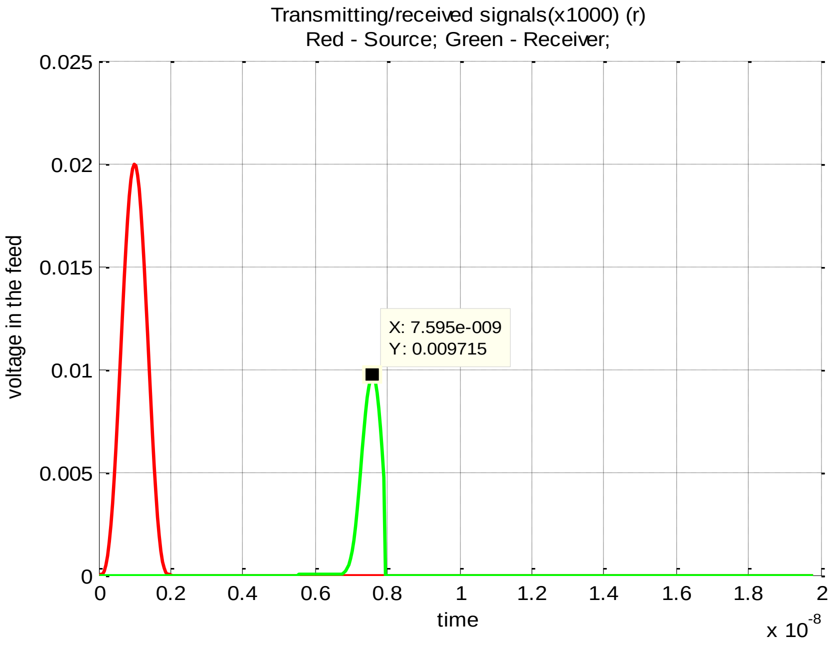

Figure 3.10 Voltage excitation (red) and voltage time-response (green) for open-door-frame door simulation.

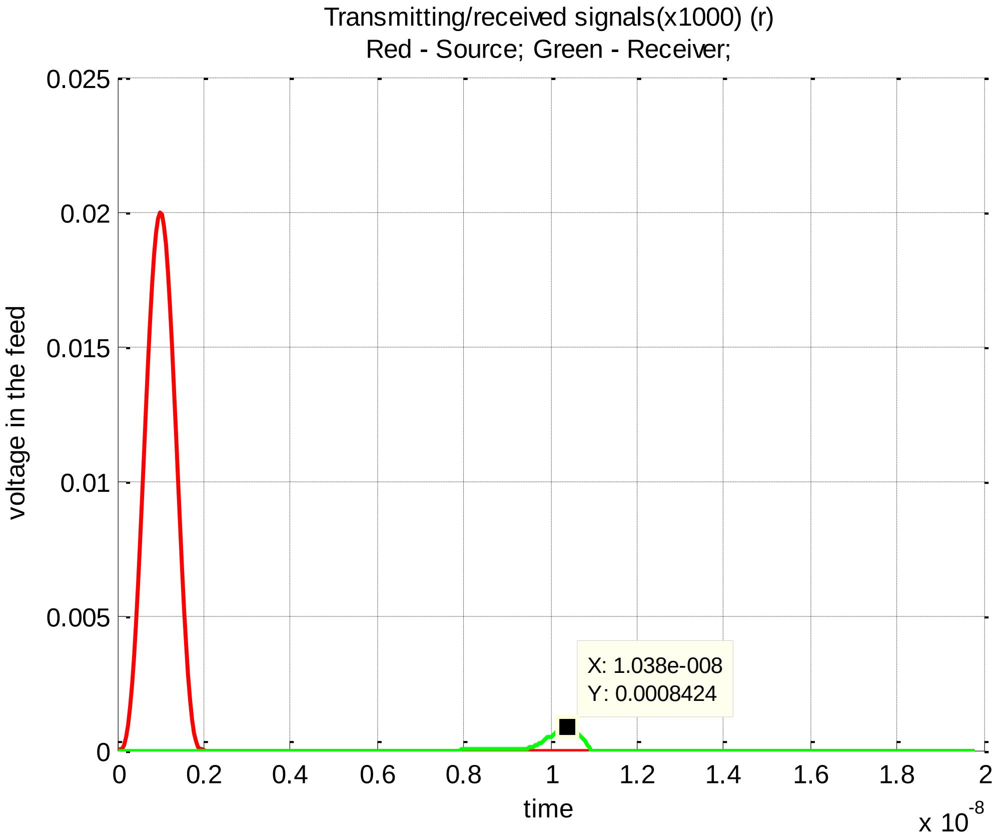

Figure 3.12 Voltage excitation (red) and voltage time-response (green) for closed-door simulation.

To simulate an open-door-frame scenario as shown in Figure 3.8 , the setup was exactly the same as a free-space experiment except that we added a 2D representation of screening walls with a dielectric constant of $\varepsilon_r = 12$ and thickness of 12cm to our configuration. Part of this configuration was the design of the metallic door frame, which we simulated as metallic 2D rectangles with real dimensions of 5 cm widths. During the open-door experiment, we observed very close agreement between free-space simulation and measurement results.

Comparing Figure 3.11 and Figure 3.10 we can conclude that the screening walls in the open-door scenario have no diffraction effect on the first path, which clearly reflects our measurement results shown in Figure 3.5.

Figure 3.12 depicts the simulation result for the closed-door scenario. The results provides 2.81 m distance between transmitter (Tx) and receiver (Rx) antennas. Such a distance reflects a DME of 0.81 m, which is close to what we see from the measurement as well. This DME is as a result of blocking of DP by the conductor screen and diffraction of first path by the edges of metallic door. In Chapter 2 we referred to this phenomena as one of the sources of UDP condition resulted from significant amount of signal attenuation for the DP.

3.5 Summary

The purpose of this chapter was to show the effectiveness of FDTD computational method to analyze the effect of micro-metals on the ranging error. Built upon the scattering theory presented in the previous section for micro-metals provided a brief summary of FDTD method equations. We also presented the discrete differential equations that our FDTD solver uses to compute the electric and magnetic fields within a computational domain. Later we presented the simulation results for free space, open-door (door frame) and closed-door scenarios and compared those results with the actual measurement results. We realized that the simulation provide us with an ideal scenario which the effect of walls that are screening , the walls placed in between antenna pair for door frame and closed-door scenario, but not the surrounding walls are captured in the real-time response of simulation. This is a good condition to investigate the effect of micro-metals on the ranging error. We were also able to have a close estimate of ranging error as a result of effect of micro-metals in present of transmitter and the receiver within our computational domain. To achieve our goal of micro-metal TOA ranging error estimation, we simulated the micro-metal object as a metallic closed-door and compared our result with the actual measurement. We conducted free pace and open-door (door frame) experiment scenarios as a proof of accuracy of our simulation and later closed-door scenario experiment to get a close estimate for ranging errors.

In the next chapter we attempt to analytically analyze the effects of micro-metals on ToA-based indoor localization. We propose UTD ray theory and geometrical ray optics to model DP, and validate the result with UWB measurement.

Chapter 4 Ray Optics and Effects of Micro-Metals

4.1 Introduction

In the previous chapter we explained how TOA-based techniques can suffer large ranging errors, mainly because of the effects of micro-metals and the human body around the transmitter and receiver. We discussed, empirical procedures that were conducted at CWIN lab in WPI to analyze the results of TOA-based measurements with ray-tracing results. Measurements were made with the receiver placed behind a macro-metallic object such as metallic chamber in CWINS lab or the elevator along corridor on the 3rd floor of Atwater building in WPI [10]. The measurement results clearly exhibited a UDP condition due to the blocking of the first path [10]. The large discrepancy that was observed between RT and the conducted measurement led the research team to examine the possible influences of micro-metallic objects such as desks, cabinets, doors or windows in those indoor environments.

The RT is a software that its algorithm operates based on applicability of Ray Optics and was originally designed for analysis of wireless channel profile for telecommunication purpose. In another word, the focus of RT algorithm has been on the average power of channel profile, whereas ToA-based localization strive for modeling and estimate of DP component and its diffraction in the proximity of metallic objects.

To better understand the evolution of RT software, the 2D RT simulation technique was originally developed [12] to analyze the behavior of wireless channels in small indoor areas using the two dimensional reflection and transmission model to trace rays by means of the ray shooting technique [4]. This model offered a low-cost means of propagation analysis for small indoor areas used for wireless local area network (WLAN) applications. Diffraction did not play a major role in most indoor radio propagation scenarios since the diffraction effect would influence propagation significantly only in locations such as corridors when the LoS path is blocked and the received signal involves multiple reflections and transmissions. However, this is not a likely situation for indoor WLAN applications, where terminals are typically used in reasonably open indoor areas. Later, a 3D ray tracing simulation [13] based on a typical residential area was developed to again analyze the behavior of wireless channel in macro-cellular high-rise urban canyons with antennas installed above roof level. This simulation was based on the model that reflections and sharp edge diffraction were the main mechanism for simulation of signal propagation.

As part of studies conducted at CWIN lab in WPI to understand the effect of micro-metals on ToA-based indoor localization systems, although introducing metallic objects, as regular objects, to the ray-tracing map improved the discrepancies in some cases, it did not significantly affect the resolution of 2D ray-tracing.

This led the research team to explore FDTD computational method as a deterministic technique that can provide accurate results while avoiding extensive measurement campaigns. While the FDTD numerical method demonstrated promising results in predicting ranging errors in proximity of metallic objects, the overheads stemmed from complexities and required computational resources (i.e. CPU, memory) associated with EM computation methods, shaped a desire to adopt UTD-based analytical approach substitute. The ultimate goal is to consider this UTD solution as an enhancement to existing RT algorithm to count for effect of diffraction in proximity of edge-shaped micro-metals in ToA-based indoor localization systems.

In the past, Bertoni et al. in [18][89][90][91] have proposed analytical procedures in order to calculate the path-loss in an urban area for communication purposes. The effort involved path-loss computation of RF propagation specific to an operating frequency in a metropolitan areas with hills, houses and large trees. The fundamental principal behind the proposed solution was to calculate the diffraction of rays by the tip of buildings and trees and their reflection by the surrounding objects (i.e. cars) in those environments based on applicability of conductor screen and right-angled wedge UTD approach. A subset of the procedures discussed in [18] entails taking advantage of conductor screen or wedge diffraction coefficients derived from [62][80] combined with a series of geometry skillsets to calculate the path-loss of the received signal based on analytical solution. In majority of cases the author did not have to worry about transition zone effect with the exception of dense cities with high-rises that the effect of multi-edge transition zone diffraction coefficient was important [92].

Since the primary focus of this chapter is to analyze the effect of micro-metals, in a ToA-based indoor localization systems, we plan on adopting the path-loss model proposed in [89] , based on applicability of models offered by [62][80] . The model adopted for the ToA-based localization operates based on center frequency of wireless channel profile instead of calculating the frequency response of wireless profile channel. This approach provides necessary and appropriate resolution [93][94], while helping with expediting the computation time of modeling and saving on computation resources. Compare to the buildings in urban area, the micro-metals are conductor objects in small dimensions positioned in the proximity of antenna pair in an indoor environment that can cause large DMEs resulted from blockage of DP. A generic form of a micro-metal in an indoor environment are conductor objects with sharp edges (i.e. metallic chamber, cabinets, doors etc.) that can be considered as conductor screens or wedges in proximity of transmitter and receiver antenna. Our analysis focuses on thin-shaped micro-metals such as a metallic door to investigate the effect of diffraction of DP by the edges of micro-metals. We introduce the effect of transition zone to the inherited path-loss model as it plays a vital role in accurate calculation of DP power in small-scaled computational domains compare to urban areas. To proceed with an analytical approach and in order to predict the behavior of DP, we leverage the UTD ray theory for conductor screen introduced by [62][80] for the path-loss calculation ,and expand the model by geometrically calculating the ToA for indoor localization purpose. The result of analytical calculation of ToA and path-loss of DP is validated with measurement campaign operating at 3 GHz center frequency and 4 GHz bandwidth. The overall solution is proposed as an enhancement to existing RT algorithm to account for effect of micro-metals for ToA-based localization systems.

The remainder of the chapter is organized as following; section 4.2 provide analysis of diffraction around edges and in particular 4.2.1 describes the measurement campaign followed by proposed analytical approach in section 4.2.2. A comprehensive analysis of analytical result as well as validation with measurement and RT results are provided in section 4.3 .Finally section 4.4 concludes the chapter.

4.2 Analysis of diffraction around the edges

In this section we discuss applicability of UTD ray theory to capture the effects of diffraction by the edges of a micro-metal such as a metallic door. We discuss the measurement campaign as well as the proposed formulation for UTD analytical approach.

4.2.1 Measurement Setup

The measurement set up consists of a UWB cone antenna pair with TE polarization as the front view of the scenario is depicted in Figure 4.1.

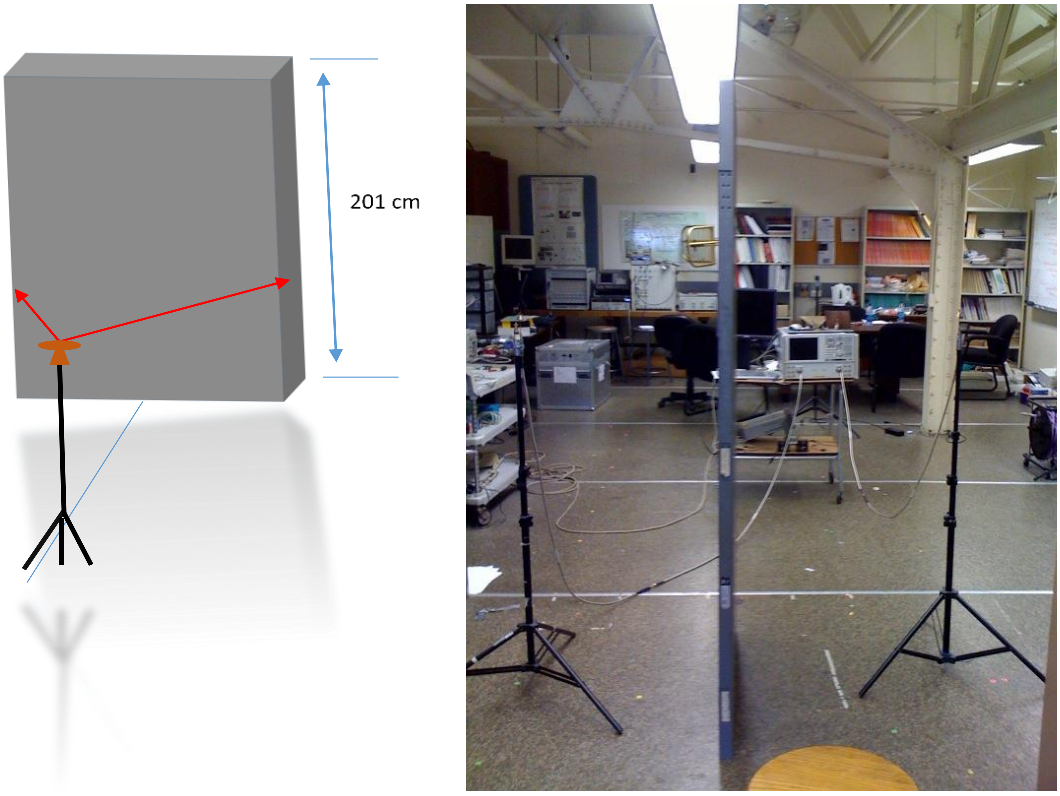

(a) (b)

Figure 4.1 Measurement campaign in proximity of a metallic door: (a) Front view (b) side view .

As shown in Figure 4.2, each one of transmitter and receiver antenna are placed 1 m away from surface of a metallic door in dimensions of 201 by 91 by 4 cm. The orientation of antennas are symmetrical to the edge. The measurement is taken by a vector network analyzer (Agilent E8363) operating at 3 GHz center frequency and sweeping 4 GHz bandwidth. The transmitter antenna is used as reference node and it is attached to tripod with the same height as receiver. During the measurement, S-parameters S_{21}, the transfer function of the channel, is measured by VNA in frequency domain with 1601 sample points. The receiver signal is transferred to time domain by inverse fast Fourier transform with a Hanning window applied to the time domain received channel profile to limit the sidelobe. The first peak can be detected by setting up proper threshold of the time domain signal strength and the propagation time of the first peak can be easily estimated. To guarantee the accuracy of the first path ToA, undesirable effects of cables, the power amplifier, antennas, and other system components are removed through system calibration. The calibration process consist of connecting the test port cables of analyzer to form a thru configuration in order to capture the thru response of the system.

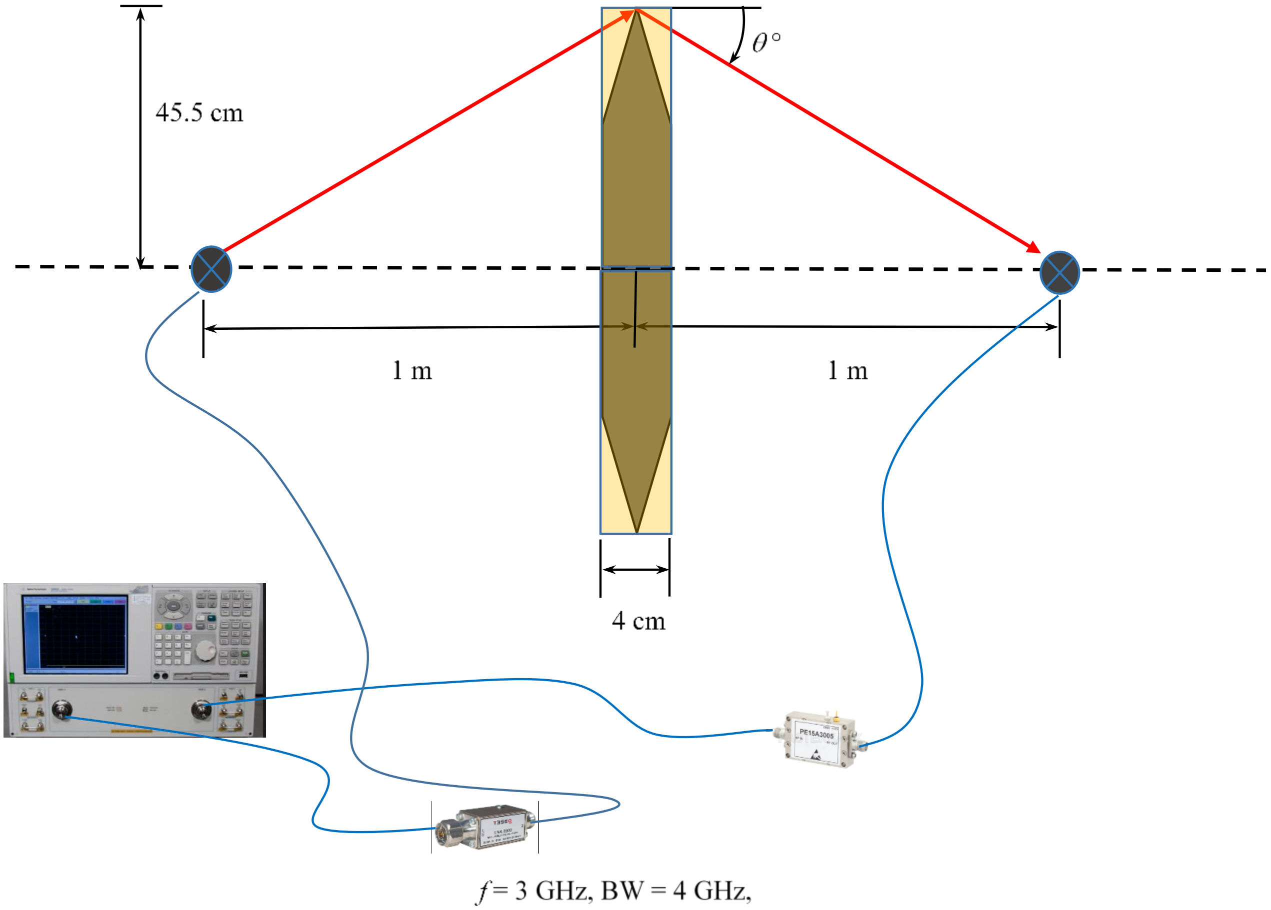

Figure 4.2 Top view of measurement campaign in proximity of a metallic door.

4.2.2 UTD Analytical Approach

The general path-loss model offered by [18][89] for diffraction by the edges of large scaled objects in urban canyons are based on applicability of the wedge

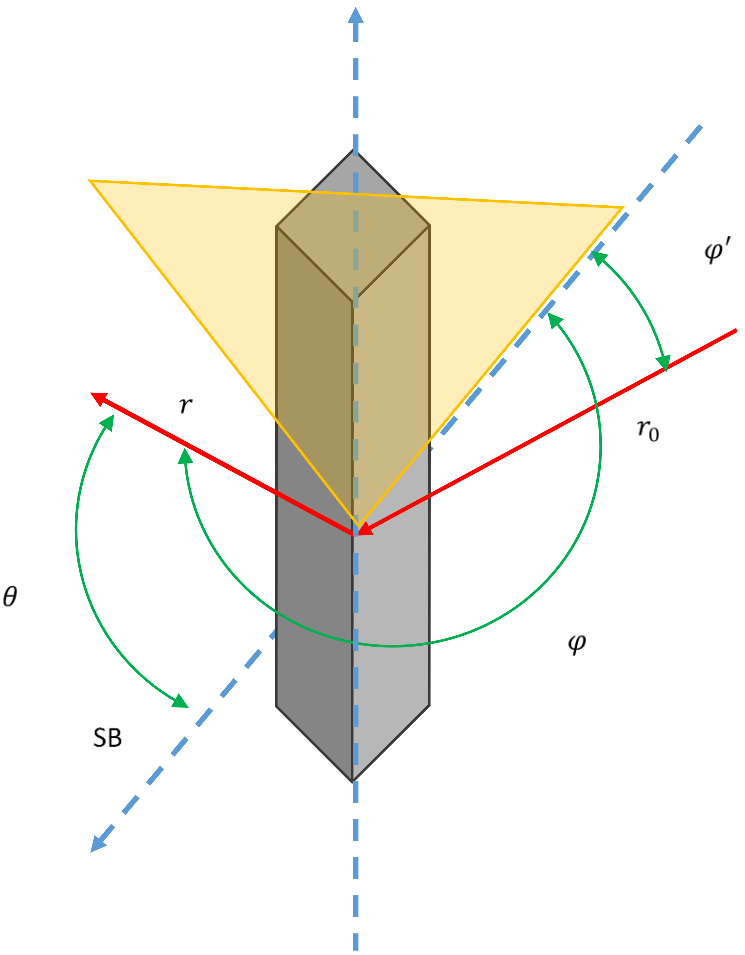

Figure 4.3 Generic edge diffraction scenario using UTD conductor wedge model.

model as shown in equation (4.1) . Figure 4.3 portraits a scenario, in which a cluster of oblique plane waves is incident upon the edge modeled as UTD ray theory of conductor wedge. The rays that illuminate the edge in turn generate cylindrical waves that propagate behind the object.

$$PG = \frac{P_r}{P_t} = \left(\frac{\lambda}{4\pi}\right)^2 \frac{\left|D_{G0}(\theta)\right|^2}{\cos^2\psi} \frac{1}{rr_0(r+r_0)} \qquad (4.1)$$

, where λ is the wavelength, θ is the angle of diffracted waves away from the edge (between the image of the incident wave and the diffracted wave), φ represents the angle of incident ray with the diffracted path, φ' represents the angle incident wave with the incident plane of the wedge, and r and r_0 are the sidelopes of antenna pair from the edge of conductor wedge model. In order to adopt the path-loss model in

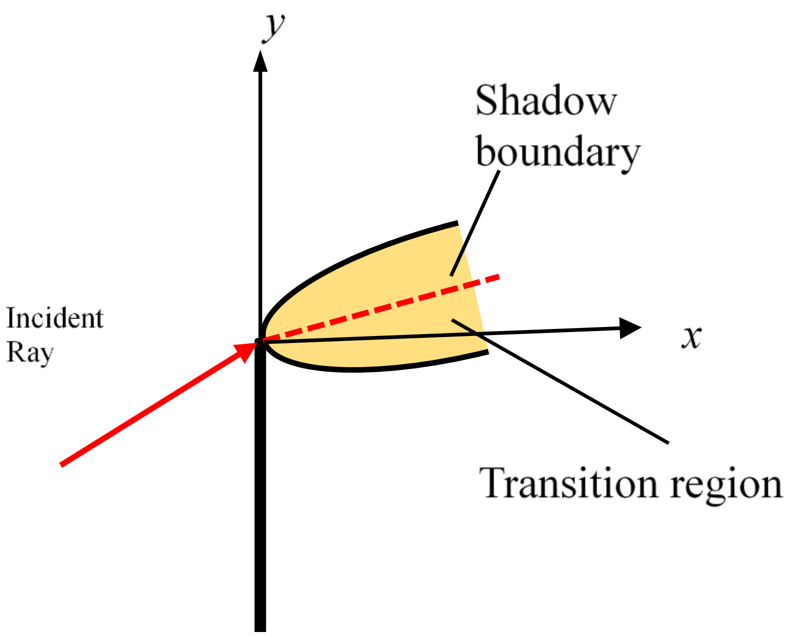

Figure 4.4 Generic diffraction scenario (side view of two edge diffraction) using UTD conductor screen model.

small scaled computational domains and indoor areas for ToA-based localization, we need to apply the effect of transition region properties, shown in Figure 4.4, to the overall path-loss model via Fresnel (transition) function [62].

$$PG = \frac{P_r}{P_t} = \left(\frac{\lambda}{4\pi}\right)^2 \frac{\left|D_{G0}(\theta)F(S)\right|^2}{\cos^2\psi} \frac{1}{rr_0(r+r_0)} \qquad (4.2)$$

The integral form of Fresnel function $F(S)$, used to count the effect of transition region, is given by [18][89] and reaches unity outside the transition region deep in shadow area:

$$F(S) = 2j\sqrt{S}e^{jS} \int_{\sqrt{S}}^{\infty} e^{-ju^2} du \qquad (4.3)$$

In equation (4.3), S varies based on the characteristic of UTD model. For the wedge model discussed here S can be defined as follows :

$$S = 2k\cos\psi \frac{rr_0}{r+r_0} \sin^2(\theta/2) \qquad (4.4)$$

An approximation to the transition function $F(S)$, is given by :

$$F(S) \cong \sqrt{2\pi S}\left[f\left(\sqrt{2\pi/_S}\right) + jg(\sqrt{2\pi/_S})\right] \tag{4.5}$$

, where $f(u)$ and $g(u)$ are defined respectively as [95][96]:

$$f(u) = \frac{1+0.926u}{2+1.792u+3.104u} \tag{4.6}$$

$$g(u) = \frac{1}{2+4.14u+3.492u^2+6.67u^3} \tag{4.7}$$

While the UTD wedge was a good fit to model the diffraction of edges for large scaled objects in [18], the conductor screening model will be adopted to count for sharp edges of micro-metallic objects for ToA-based localization as depicted in Figure 4.5. In the former case it is safe to assume the distance between each edge to another one is relatively large where as in later one we can consider this distance negligible.

Figure 4.5 depicts a scenario antenna pair are position in the proximity of a metallic door. Considering the edge of the metallic door as a conductor screen, It provides a snapshot of incident and diffracted waves by the tip of the conductor screen. The φ represents the angle of incident ray with the diffracted path, φ'

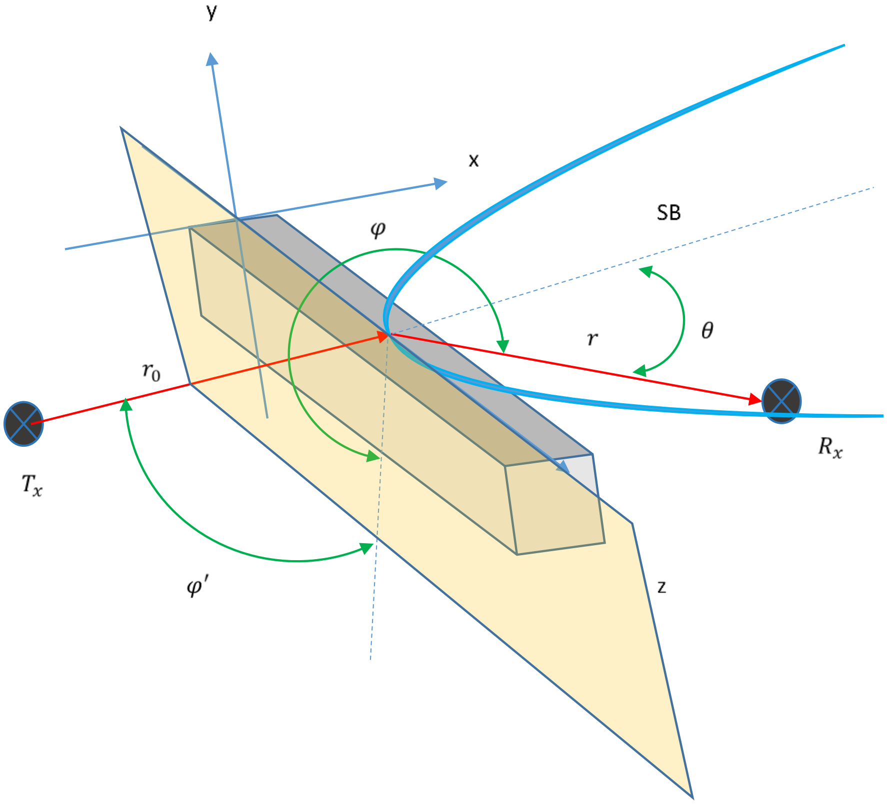

Figure 4.5 edge diffraction of a micro-metal modeled as conductor screen.

represents the angle incident wave with the incident plane of the wedge, and r and r_0 are the sidelopes of antenna pair from the edge of conductor wedge model with the receiver positioned in the transition region. The diffraction coefficient function can then be resented as equation (4.8) for a UTD ray theory of conducting screen [62][80]:

$$D(\varphi, \varphi') = \frac{-1}{2\sqrt{2\pi k}} \left\{ \frac{1}{\cos\frac{\varphi - \varphi'}{2}} + \frac{\Gamma_{E,H}}{\cos\frac{\varphi + \varphi'}{2}} \right\} \qquad (4.8)$$

, where k is the wavenumber, Γ_E = -1 for E parallel to the edge and Γ_H =1 for H parallel to the edge. Using applicability of equation (4.3) and equation (4.8) and applying them to the path-loss model in equation (4.1) , we can derive equation (4.9) , which is an appropriate path-loss model suitable to ToA-based indoor localization in the proximity of micro-metals.

$$PG = \frac{P_r}{P_t} = \left(\frac{\lambda}{4\pi}\right)^2 \frac{\left|D(\varphi,\varphi')F(S)\right|^2}{\cos^2\psi} \frac{1}{rr_0(r+r_0)} \qquad (4.9)$$

Consequently, The τ ,ToA of diffraction of DP by the edge, will be calculated using following equation (4.10) :

$$\tau = {}^{d}/_{c} = \frac{r+r_0}{c} \qquad (4.10)$$

, where c is the speed of free space wave propagation and d is the DP traveling distance from transmitter to the receiver. In this case it is an aggregation of r and r_0 sidelopes for the incident and diffracted rays.

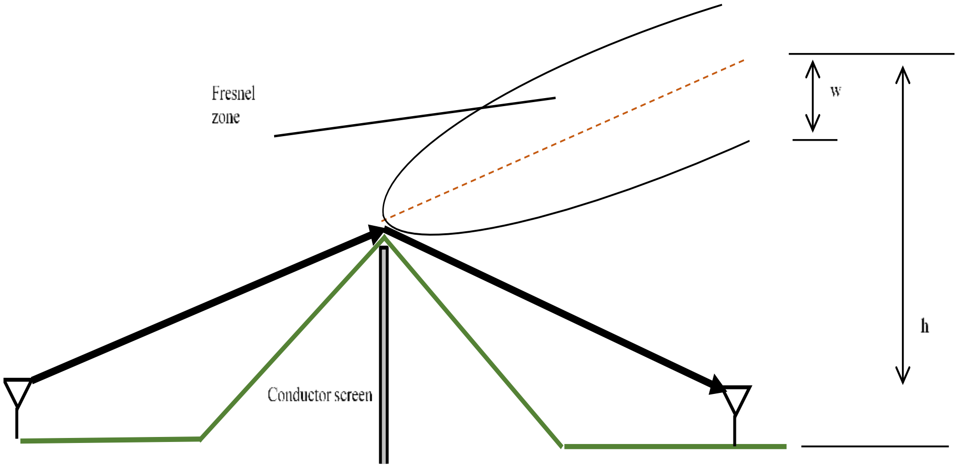

Figure 4.6 description of transition zone in proximity of metallic door edges.

To put the effects of transition zones around the edges of metallic door into some perspective and understand the influence of equation (4.3), we refer to Figure 4.6 , where transmitter and receiver are placed to the sides of a conductor screen edge. Using equation

(4.11**)** [91], we can calculate the half-width of the transition region for a receiver located about the shadow boundary of an imaginary wedge. The half-width is directly proportional to wavelength and the length of antenna sidelope from the conductor screen edge (tip of the wedge) [73]. Comparing *w* (half-width) and *h* (the distance from projection of antenna on the door to the transition zone shadow boundary), we can confirm whether receiver is located in the transition zone or not.

$$w = \sqrt{\frac{\lambda RR'}{R + R'}} \tag{4.11}$$

4.3 Comparison of Analytical with Empirical Results

To proceed with the proposed analytical approach, we start off by calculating the path-loss for the diffracted rays from the edges of the micro-metallic door using equation (4.9). The antenna that is used in the measurement campaign has a TE polarization, E parallel to the edge, calling for utilizing Γ_E = -1 in calculation of diffraction coefficient in equation (4.8). Figure 4.7 depicts the result of analytically calculated path-loss for the DP diffracted by edges of the metallic door for the bandwidth range of 1-5 GHz and it shows the calculated path gain has a reciprocal relationship to the operating frequency and direct relationship to the wavelength that is confirmed by equation (4.8) .

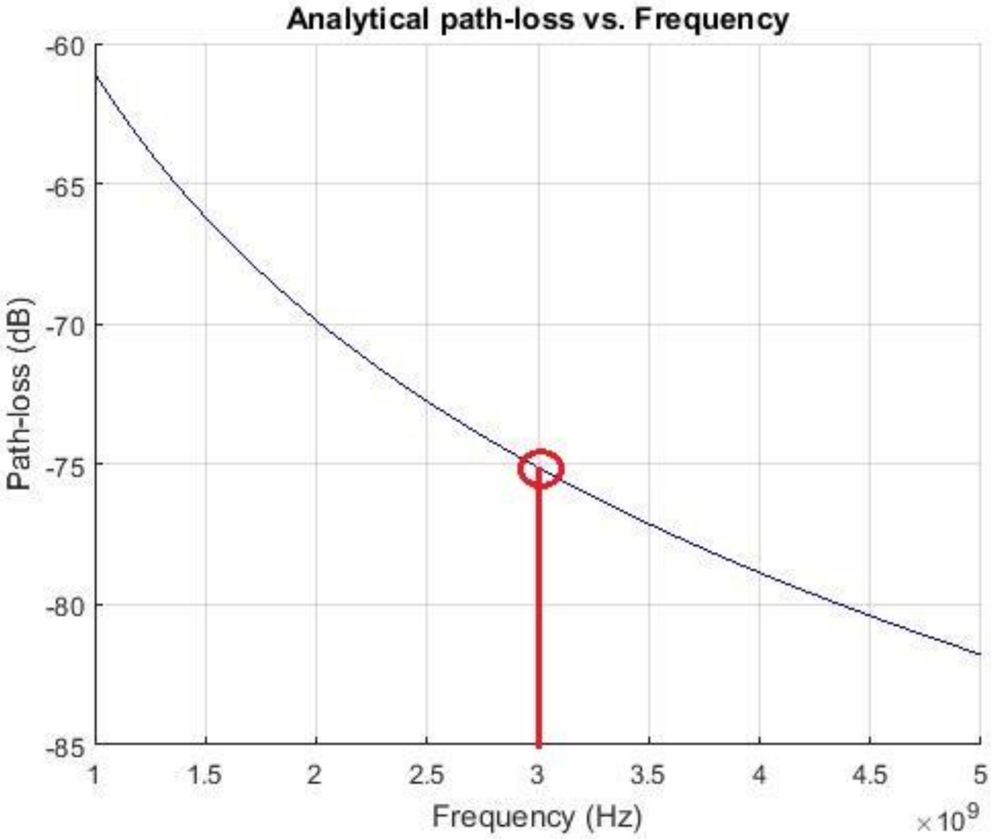

Figure 4.7 Analytically computed path-loss for diffracted DP.

A quick numerical analysis of wavelength (λ), S from equation (4.4) and magnitude of transition function ($|F(S)|$) is provided in Table 1 , where it clearly shows as the frequency is increases, the λ decreases, S grows and $|F(S)|$ reaches unity.

Table 1 Numerical analysis of analytical approach

Frequency	λ	**S**	$\lvert F(s)\rvert$
100 MHz	3	0.03947	0.6832
450MHz	0.6667	1.7760	0.9121
900 MHz	0.33	3.5519	0.9715
1.8 GHz	0.1697	6.9763	≈ 1

The big take away from this analysis is the fact as frequency increases, the effect of transition region on the diffracted rays (DP) becomes negligible. Based on following analysis, and the result of path-loss provided in Figure 4.7 , it is safe to assume the effects of diffraction by the edges of micro-metals would be more aggressive as the frequency increases.

From Figure 4.7, it is clear an adaptation of 3 GHz center frequency of the bandwidth in our analytical calculation, leads to PL = 75 dB. Effect of transition zone plays a vital role in accurate computation of path-loss. Using half-width of transition zone from equation (4.11) and position of receiver antenna from the shadow boundary we can confirm the receiver is located in the transition region.

Later on using equation (4.10), the ToA of diffracted DP can be calculated though in upcoming analysis we leverage the traveling distance. The fact antenna pair are located symmetrically from the edges of the door, it makes it easy to geometrically calculate the traveling distance of first path. The total traveling distance for the DP includes the distance from the transmitter to one edge of the door, and diffraction of that from the edge in to the receiver sensor, which was calculated as 2.19 m.

During the measurement campaign, which its results are depicted in Figure 4.8, we recognized one of the paths at distance ~ 2.2 m (among the paths that were not the strongest ones – in UDP condition) and measured its power. At this point we assumed this specific path is the power of the signal that is diffracted DP from one edge of the door. Later on, using two RF absorber as shown in Figure 4.9, we attempted to block two side edge of the door, which abruptly caused a power reduction in the aforementioned path. Consequently, removing one of the absorbers

Figure 4.8 Measurement campaign – Blocking diffraction path on one side of the metallic door using an absorber.

from the edge of the door (Figure 4.10) we see the path at ~2.2 m again comes to live. This confirms our assumption; the path at ~2.2 m is in fact the diffracted DP.

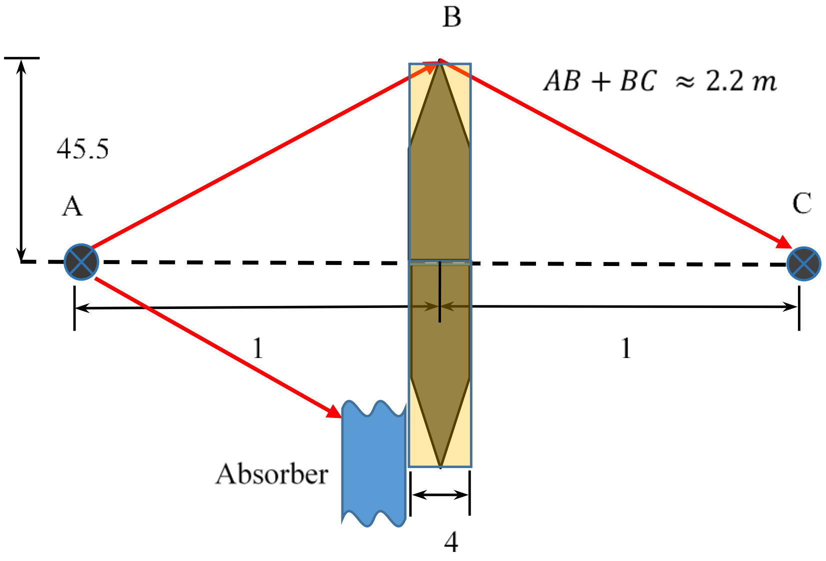

Figure 4.10 Measurement campaign – Blocking diffraction path on one side of the metallic door using an absorber.

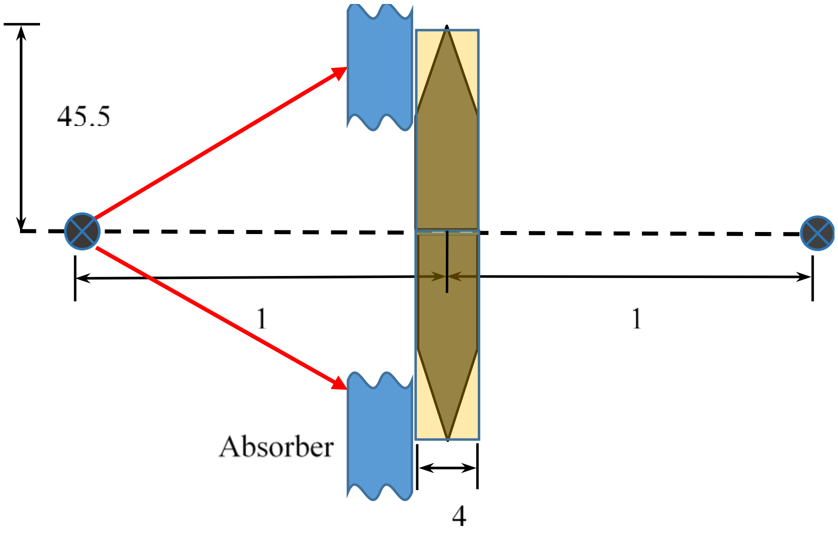

Figure 4.9 Measurement campaign – Blocking diffraction paths on both sides of the metallic door using an absorber.

Comparing analytically calculated path-loss from Figure 4.7 and calculated ToA from equation (4.10), with the empirical results captured in Figure 4.8 , shows that the measurement results and the analytical results are in good agreement. In both cases we see a path-loss of ~ 75 dB for the path at ~2.2 m, which is confirmed as the diffracted DP by the edges of metallic door.

To show the effectiveness of proposed analytical approach as an enhancement to existing RT algorithm, we attempt to make a comparison of proposed analytical approach, and the existing RT algorithm. Figure 4.11 provides a snapshot of the RT simulation for the same measurement scenario which antennas are positioned 1 m away from the surface of a metallic door. The result of RT simulation provides approximately 25 m ranging error relative to the measured diffraction that is provided in Figure 4.8.

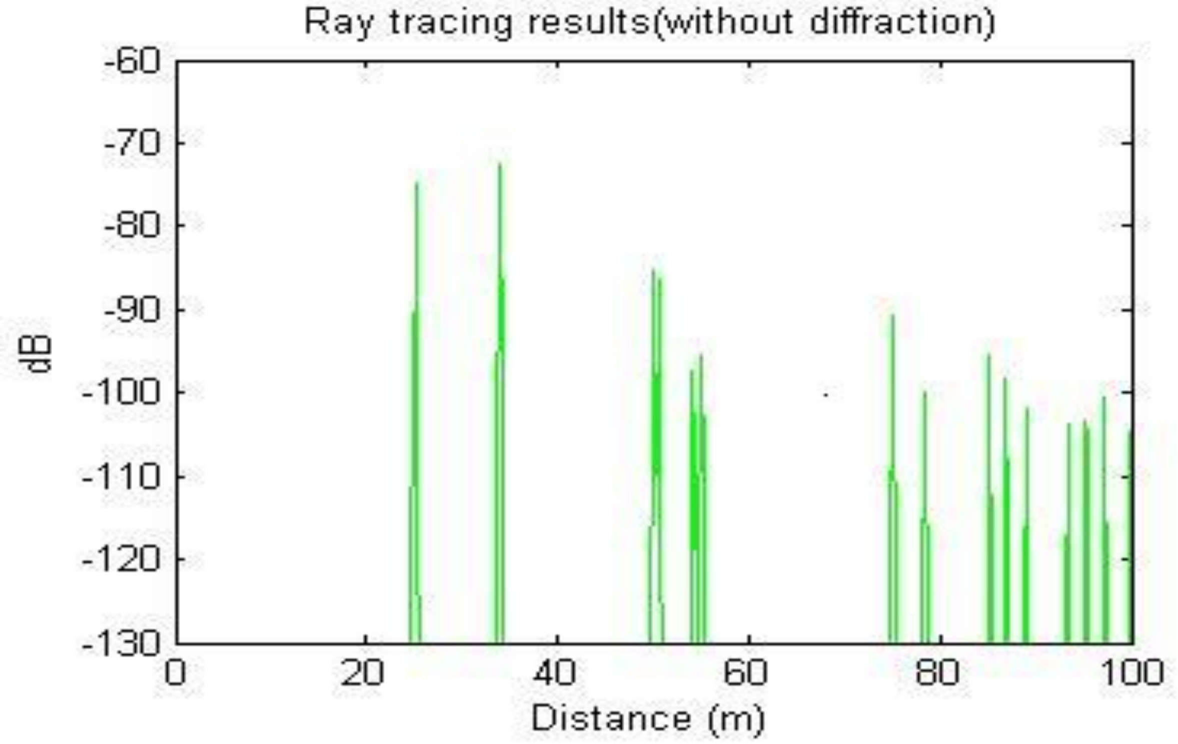

Figure 4.11 RT simulations for 2(m) antenna separation with metallic door in between.

4.4 Summary

The primary focus of this chapter was to analyze the effect of micro-metals, in a ToA-based indoor localization systems. To proceed with an analytical approach in order to predict the behavior of DP in the proximity of micro-metals the path-loss model, originally used for communication purposes in urban areas, is adopted which operates based on center frequency of wireless channel profile. Compare to the buildings in urban area, the micro-metals are conductor objects in small dimensions positioned in the proximity of antenna pair in an indoor environment that can cause large DMEs resulted from blockage of DP. A generic form of a micro-metal in an indoor environment are conductor objects with sharp edges (i.e. metallic chamber, cabinets, doors etc.) that can be considered as conductor screens or wedges in proximity of transmitter and receiver antenna. Our analysis focused on thin-shaped micro-metals such as a metallic door edges and to align with that the diffraction coefficient model is changed from wedge model originally used in urban and large scaled areas to screen model for small scale computational domain. We introduced the effect of transition zone to the inherited path-loss model as it plays a vital role in accurate calculation of DP power in small-scaled computational domains compare to urban areas. To proceed with an analytical approach and in order to predict the behavior of DP, we leverage the UTD conductor screen diffraction coefficient for path-loss calculation, and expand the model by geometrically calculating the ToA for indoor localization purpose. The result of analytical calculation of ToA and path-loss of DP is validated with measurement campaign operating at 3 GHz center frequency and 4 GHz bandwidth. The overall solution is proposed as an enhancement to existing RT algorithm to account for effect of micro-metals for ToA-based localization systems.

In the upcoming chapter, we focus on analytical analysis of effects of human body on ToA-based localization. In particular, the next chapter discusses UTD ray theory and geometrical procedures to model DP for a scattering scenarios.

Chapter 5 Ray Optics and Effects of Human Body

5.1 Introduction

The area of Body Area Network has recently drawn a special attention by the community with the purpose of unveiling propagation phenomena in the proximity of human body [74][75][76][77][78][79]. Specific to human body indoor localization, majority of UTD-based research studies consider the human body as smooth convex surfaces such as a conductor sphere or a cylinder, which does not persist as a uniform approach for different orientation of source and field point in respect to the surface [80]. This scenario can be further categorized into coupling (creeping waves for on and off the surface) and radiation problems in terms of different Fock functions, and scattering problem in terms of Pekeris functions in the proximity of human body. The studies conducted by [80][83][97][98] pay special attention to the effect of transition region in such circumstance, and such prominence plays a vital role in accuracy of human body ToA-based localization systems where it has a dominant effect to the accurate modeling of DP [98]. In the past, [19][22] have applied applicability of [80] for coupling and scattering problems for Body-Area-Networks (BAN). In [22], authors leverage a cylindrical UTD ray theory that utilizes the Fock coupling functions and applies a mechanistic multiplication of UTD coupling coefficients to compute the fields around the surface of human body. The field only assumes the creeping waves and bounds the applicability of the solution in the transition zone for those scenario. Consequently, authors in [99][100] have followed the creeping theory and coupling functions introduced in[97][101], for on-body propagation solutions, when the height of antenna from the body surface are in small fractions of wavelength (~ $\lambda/20$ or less), and [102] based on applicability of [84][97], and [42] based on applicability of [103][104] have investigated scattering scenarios in the proximity of human body. In the scattering cases of [19][42], the validation scenario is purposely chosen such that the receiver sensor avoids the transition zone.

From the above scholarly studies on the human body, [100] seems to be the only one that has truly captured the effect of transition zone in prediction of fields thru utilizing the fundamental coupling work of Paknys [97], which has discussed transition function as a part of unified creeping formula introduction. Koutitas' proposed solution for multi-human body effect in [102] remains limited to analyzing the effect of transition zones based on the approach of providing modification to [80] in accordance to scattering modification of Paknys to [83] in [98]. As a result, the proposal only analyzes the cross-propagation in deep shadow and outside transition zone by assuming transition function reaching unity, or limited to the scenario the receiver is mounted 6 mm ($h = \lambda/10$ for 5 GHz) from surface of the body. Except the studies presented by Lee et al. in [42] and Zhao et al. in [22], the rest of aforementioned studies pay less attention to localization and ranging errors in the proximity of human body, and rather their focus is on the delay spread of wireless channel profile for communication purposes. This highlights the necessity of analyzing ranging errors in the proximity of human body and in transition zone for a BAN scattering scenario.

In this paper, and with consideration of past struggles to take into account the effect of transition function formulation embedded within the UTD ray theory of smooth convex, different UTD scattering approach is followed in the proximity of human body. We plan on computing the creeping wave fields based on fundamental smooth convex surface proposed in [80], and apply it in terms of creeping wave diffraction coefficient to the UTD ray theory of conductor wedge path-loss originally introduced in [73] for the communication purposes in the urban areas. Embedded in the UTD conductor wedge path-loss, the wedge diffraction [62] encapsulates the transition function property that will help with precise prediction of the fields in the transition region and in the proximity of human body. A mechanistic multiplication of the creeping wave diffraction coefficient and the wedge diffraction coefficient is conducted to help with blending the effect of creeping wave into the UTD ray theory wedge model, which can be described in terms of EM field properties in the proximity smooth convex surface. Contrary to the previous approaches that have perused full frequency-response solution, we will apply the center frequency of channel profile, which helps with expediting the simulation time as well as saving on computational responses. To model the ranging errors, a custom geometrical formulation of ToA is adopted. Both the path-loss and the ToA formula are applied to the first path, which correlates to the only shortest diffracted (including the creeping wave) path in the proximity of the human body, and confirmed by statistical models introduced in [34][37] for coupling and scattering, respectively.

Closest to the hybrid approach proposed in this paper for ToA-based localization purpose, Bertoni in [73] applies asymptotic UTD ray theory of creeping wave diffraction coefficient as a substitute to wedge diffraction coefficient in wedge path-loss model over large urban hills and bumpy areas for communication purposes with a focus on delay spread of wireless channel profile. Moreover, since the evaluation of analytical approach occurs in a large scale, the effect of transition zone is simply eliminated. In the past, Wang et al. in [105] have also proposed a three-edge diffraction model to capture the shadowing effect in the proximity of human body, however it bounds the effect of creeping wave and ultimately is not consider as a sound option for an accurate ToA-based localization, which is confirmed by their validation campaign. In this paper, the validation procedure involves comprehensive analysis of creeping and wedge diffraction coefficients along with comparison of analytical calculation of path-loss and ToA with the wideband measurement that is performed by a vector network analyzer operating at 900 MHz, sweeping 100 MHz of bandwidth, and the HFSS simulation (a FEM solver). Compared to the previous scholarly studies that have considered an arbitrary creeping angle for coupling ($e^{-j(\omega/c)d}$) [22] or scattering scenarios ($\xi = m\,\theta$) [98], the evaluation of proposed analytical approach in this paper is conducted in a rather unique way by discovering a range of possible creeping angles that could apply to the specific positioning of transmitter and receiver in respect to the body, and choosing the appropriate one by matching the scenario to the well-known statistical models provided in [63]. The analytical approach discussed in this paper is recommended as a simulation enhancement to existing RT algorithm and for human body ToA-based indoor localization.

This paper is organized as follows: Section 5.2 covers analysis of effect of human body on ToA-based indoor localization systems for a scattering scenario including discussion of measurement setup in section 5.2.1, analytical model for path-loss and ranging error in section 5.2.2 and validation discussion in 5.3. Finally, section 5.4 presents our conclusion.

5.2 Analysis of Effects of Human Body for Scattering Scenarios

In this section, we conduct an analytical approach based on applicability of UTD to calculate first path path-loss and ToA for a scenario that antenna pair placed to the sides of a human torso. The upper portion of human body is considered as a conductor cylinder such that; the overhead view of torso displays as circular cross-section with radius R (Figure 5.1-a and Figure 5.1-b).

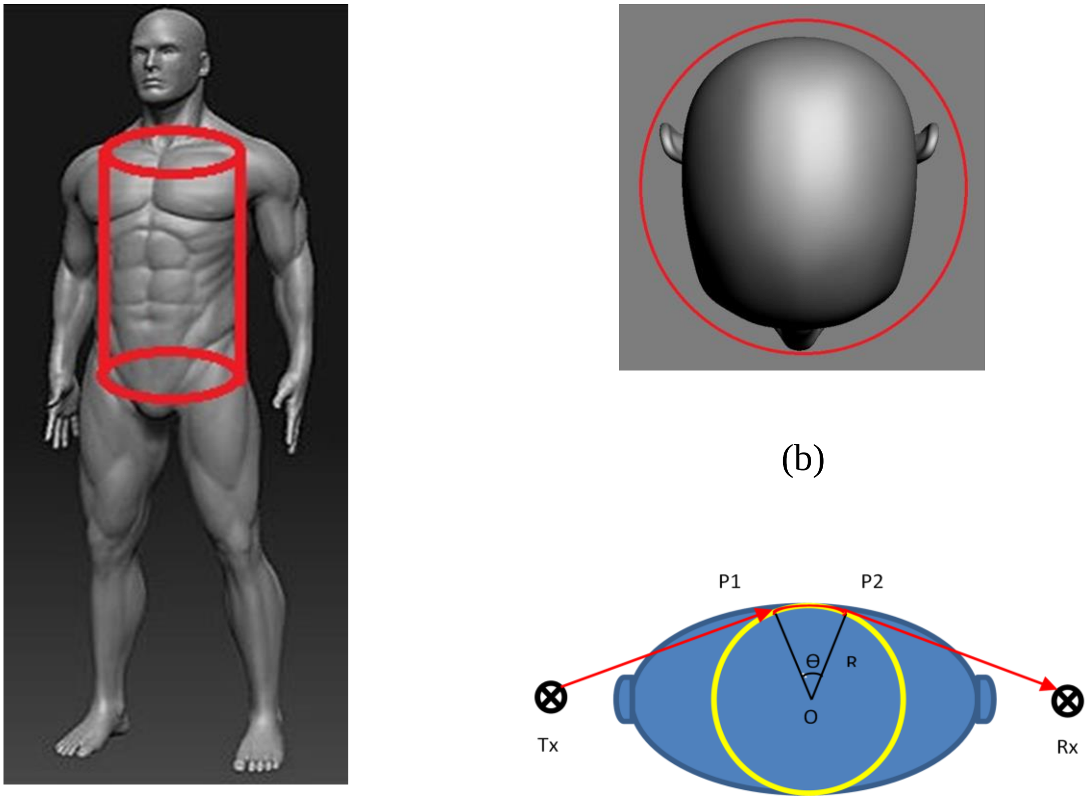

(b)

(a)

(c)

Figure 5.1 (a) Upper section of human body considered as conductor cylinder embedded in human torso (b) Overhead view of cylinder circular cross-section in relationship with human head (c) Overhead view of creeping waves, with angle $\boldsymbol{\theta}$, over cross-section of cylinder embedded within an oval-shaped torso for a scenario Tx and Rx are placed to the side of human body.

In particular, we are interested in behavior of shortest diffracted first path from the time rays emanate from transmitter, hit the side of human body and creeping over body surface to the gazing point toward the receiver. Figure 5.1-c portrays the top view cross-section of a human torso with an embedded conductor cylinder with a radius of R. In a scenario that a human body is located between transmitter (Tx) and receiver (Rx), it is clear that once the radio waves hit the torso at point P1, on the circular cross-section of cylinder, those waves diffract and continue traveling on a curvature path with an angle θ until reach point P2 and leave the body surface toward the receiver. That part of the waves that travels over the body surface and around the circle cross-section referred to as creeping wave and angle θ referred to as the creeping angle.

5.2.1 Measurement Setup

Figure 5.2-a and Figure 5.2-a portrays the measurement scenario used for our analysis. The set up consists of a dipole antenna pair with TM polarization placed at 50 cm separations to the sides of human torso with radius approximation of 10.6 cm. The separation of antenna pair matched to size of human body subject in the measurement to situate the placement of receiver in the transition region. The

measurement is taken by a vector network analyzer (Agilent E8363) operating at 900 MHz, and sweeping 100 MHz of bandwidth**.** The human involved remains standing posture during the measurement. The transmitter antenna is used as reference node and it is attached to tripod with the same height as receiver. During the measurement, S-parameters S_{21}, the transfer function of the channel, is measured by VNA in frequency domain with 1,601 sample points. The receiver signal is transferred to time domain by inverse fast Fourier transform with a Hanning window applied to the time domain received channel profile to limit the sidelobe. The first peak can be detected by setting up proper threshold of the time domain signal strength and the propagation time the first peak can be easily estimated. To guarantee the accuracy of the first path ToA, undesirable effects of cables, the power amplifier, antennas, and other system components are removed through system calibration.

(a) **(b)**

Figure 5.2 (a) Measurement setup (b) Measurement setup with human body placed in between antenna pair.

5.2.2 Modeling of Path-loss and Ranging Error

The basic ray tracing software functions based on two fundamental algorithms; the image method and method of shooting and bouncing (SBR) [12]. The UTD models and geometrical procedures proposed in this paper are targeted for SBR-based RT algorithms, and the focus of algorithm should be on ToA and path-loss of the first path, or shortest diffracted path, in order to leverage those RT methods for human body ToA-based indoor localization systems. The main goal of this paper is to propose an analytical UTD enhancement to the existing SBR-based RT algorithm to calculate ToA and path-loss of the first path for scenarios the receiver sensor is located in the transition region. As discussed in the introduction of this paper, with the consideration of past struggles to take into account the effect of transition function formulation embedded within the UTD ray theory of smooth convex, we are planning to follow a different scattering UTD approach in the proximity of human body. We plan on computing the creeping wave fields based on fundamental smooth convex surface proposed in [80], and will apply it in terms of creeping wave diffraction coefficient to the UTD ray theory of conductor wedge path-loss originally introduced in [73] for the communication purposes in the urban areas. Embedded in the UTD conductor wedge path-loss, the wedge diffraction [62] encapsulates the transition function property that will help with precise prediction of the fields in the transition region and in the proximity of human body. A mechanistic multiplication of the creeping wave diffraction coefficient and the wedge diffraction coefficient will be discussed and described in terms of EM fields in the proximity of torso surface to help with blending the effect of creeping wave into the UTD ray theory wedge model. Figure 5.3 – a displays the upper section of a human torso for a scattering scenario. The torso is presented as a cross-section of a conductor cylinder (in purple) with radius, which encapsulates a conductor wedge (filled in blue). Figure 5.3 – b, provides top view cross-section of human body considered as a conductor cylinder.

In an attempt to proceed with the analytical approach, the overall path-loss will be calculated in three steps. The first step is to calculate the diffraction coefficient of creeping wave using diffraction model around a conductor cylinder [80][91]. The subsequent step would be to transition the problem from a conductor cylinder into a conductor wedge model by considering P_1 and P_2 (Figure 5.3), overlap each other at one point, and compute the diffraction coefficient that brings into consideration the effect of Fresnel zone [62]. The final step would be calculation of total path-loss using total diffraction coefficients. The diffraction coefficient of creeping wave depends on two coefficients of ψ_1 and D_1, which subsequently depend on polarization of electrical (E) and magnetic (H) fields and the ratio of cylindrical radius R to the wavelength (λ). The $\psi_1$coefficient is an important entity in our calculation as its real part denotes the attenuation of creeping wave and losing energy in form of, rays leaving surface along the tangential line at P_2 [80][91].

$$\begin{cases}\psi_1^e \\ \psi_1^h\end{cases} = \left(\frac{\pi R}{\lambda}\right)^{1/3} e^{j\pi/6} \begin{cases}2.338 \\ 1.019\end{cases} \tag{5.1}$$

$$\begin{cases}D_1^e \\ D_1^h\end{cases} = \frac{1}{\sqrt{2\pi}}\left(\frac{\pi R}{\lambda}\right)^{1/3} e^{j\pi/6} \begin{cases}2.034 \\ 3.421\end{cases} \tag{5.2}$$

The superscripts e and h depicted in equations (5.1) and (5.2), denote TE and TM polarization associated with $\psi_1$and D_1 for a conductor cylinder. It is known that, creeping wave field decreases exponentially with angle θ and for:

$$\theta \geq (\lambda/\pi R)^{1/3} \tag{5.3}$$

, the creeping wave diffraction coefficient is perceived by [80][73].

$$D_{T-Creeping} = D_1 e^{-\psi_1 \theta}/\sqrt{k} \tag{5.4}$$

Once the creeping wave diffraction coefficient is calculated, the problem formulation transition into approximation of a conductor wedges scatterer. Subsequently, it is safe to assume P_1 and P_2 overlap each other at one point at the peak of the wedge and rays will intercept the peak of triangle cross-section of the wedge that has an inner angle of $M = {}^{\pi}/_{2}$.

$$(2 - n)\pi = M \tag{5.5}$$

Figure 5.3 provides an illustration to this discussion, and it depicts angles φ' and φ with the incident triangle surfaces for incident and diffracted rays (in green) respectively. The Transition zone presented with the shadow boundary as an extension of incident cylindrical waves, which it's half-width calculated using equation (5.6). The half-width is directly proportional to the wavelength and the length of antenna sidelobe from human torso and can be leveraged to analyze the orientation of receiver in respect to the transition region [73]:

$$w = \sqrt{\frac{\lambda RR'}{R + R'}} \tag{5.6}$$

The total diffraction coefficient is a combination of diffracted and reflected waves from both incident and reflected surfaces of triangle with consideration of polarization of incident wave [73]. For a right-angled conducting wedge, the GTD diffraction apprehended as following [73][80] :

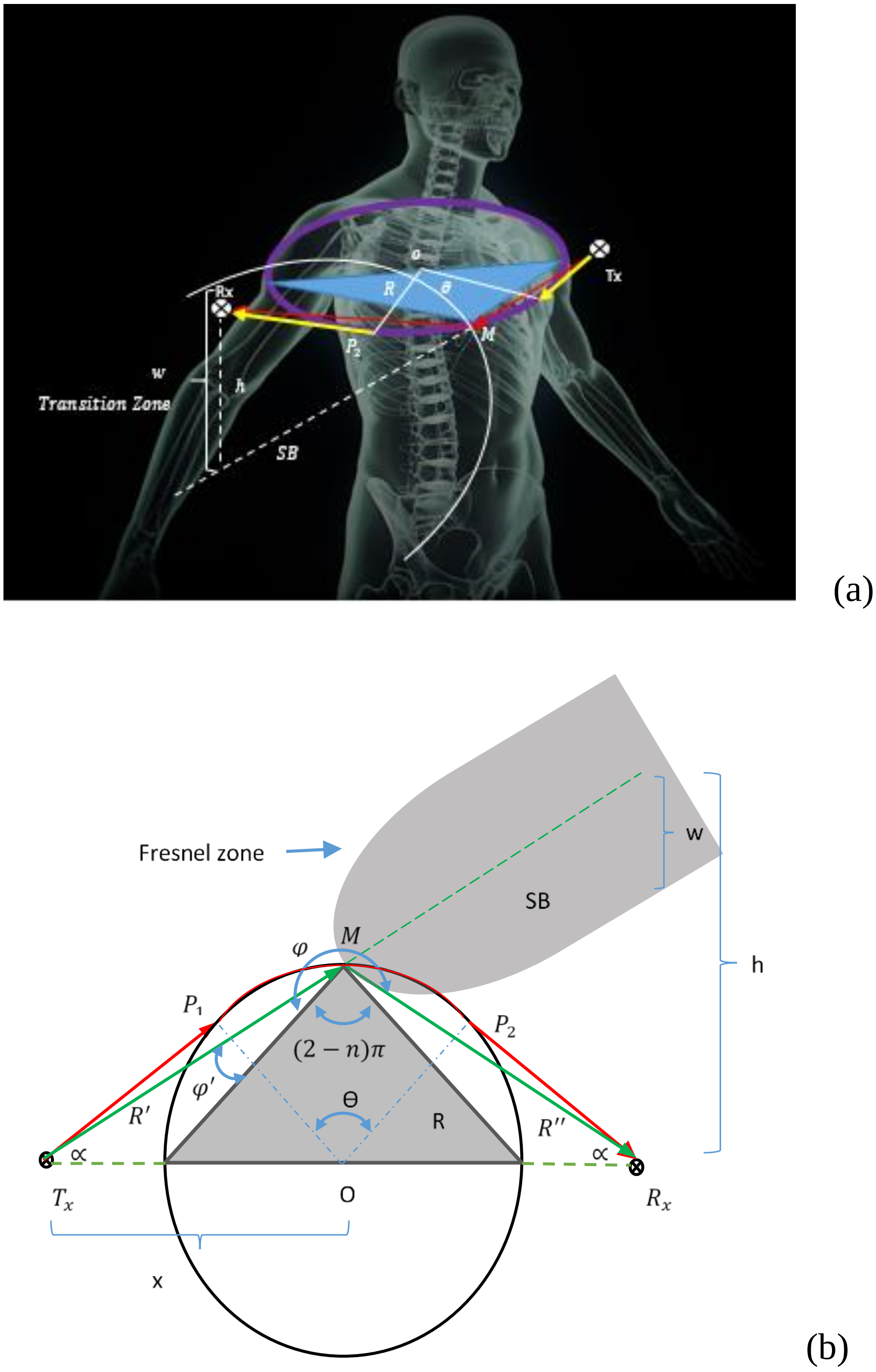

Figure 5.3 (a) scattering by human body (b) top-view scattering by human body.

$$D_{T-Wedge} = D_1 + D_2 + \Gamma_{E,H}(D_3 + D_4) \tag{5.7}$$

Using diffraction coefficient and Fresenl functions introduced in [62], equation (5.7) will become:

$$D_{T-wedge} = \frac{-e^{j\pi/4}}{2n\sqrt{2\pi k}} * \{ \tag{5.8}$$

$$\left[\cot(\frac{\pi + (\varphi - \varphi')}{2n}) F[kL\, a^{+}(\varphi - \varphi')]\right.$$

$$\left. + \cot(\frac{\pi - (\varphi - \varphi')}{2n}) F[kL\, a^{-}(\varphi - \varphi')]\right]$$

$$+ \Gamma_{H,E}\left[\cot(\frac{\pi + (\varphi + \varphi')}{2n}) F[kL\, a^{+}(\varphi + \varphi')]\right.$$

$$\left. + \cot(\frac{\pi - (\varphi + \varphi')}{2n}) F[kL\, a^{-}(\varphi + \varphi')]\right] \}$$

The "$F(x)$" in equation (5.8) is the Fresnel function provided by equation (5.9) used to account for behavior of rays in transition zone, which its approximation is provided by equations (5.10) - (5.12) [73]:

$$F(S) = 2j\sqrt{S}\, e^{jS} \int_{\sqrt{S}}^{\infty} e^{-ju^2} du \tag{5.9}$$

$$F(S) \cong \sqrt{2\pi S}\left[f\left(\sqrt{{2\pi}/{S}}\right) + jg(\sqrt{{2\pi}/{S}})\right] \tag{5.10}$$

$$f(\tau) = \frac{1 + 0.926\tau}{2 + 1.792\tau + 3.104\tau^2} \tag{5.11}$$

$$g(\tau) = \frac{1}{2 + 4.142\tau + 3.492\tau^2 + 6.670\tau^3} \tag{5.12}$$

Considering a perfectly conductivity of the wedge-shaped model, in equation (5.8) $\Gamma_E = -1$ used for waves with E^{inc} polarized parallel to wedge and $\Gamma_H = +1$ for H^{inc} polarized parallel to wedge.

To study a NLoS scenario using wedge model, where human body obstructs the DP, the angles α, φ and φ' are of interest calculated correspondingly:

$$\alpha = \tan^{-1}({R}/{x}) \tag{5.13}$$

$$\varphi' = ({\pi}/{4}) - \alpha \tag{5.14}$$

$$\varphi = ({3\pi}/{4}) - \varphi' \tag{5.15}$$

Associates to the cylindrical incident wave, there is a parameter:

$$L = \frac{RR'}{R + R'} \tag{5.16}$$

, and in calculation of $a^{\pm}\,(\beta)$, $N^{\pm}$ is considered as the closest integer to:

$$(\beta \pm \pi)/2\pi n \tag{5.17}$$

, based on (n) derived from equation (5.5) [62]:

$$a^{\pm}\,(\beta) = 2\,cos\left(n\pi N^{\pm} - {}^{\beta}\!/_{2}\right)^{2} \tag{5.18}$$

The diffraction coefficient over the smooth convex of $\widehat{P_1M}$, at point M as a result of wedge model and over smooth convex of $\widehat{MP_2}$ are represented by D_{P_1M} , $D_{T-Wedge}$, and D_{MP_2}respectively. They can be described in terms of ration of fields of the end point to the beginning point of the domain path they represent, which can help with blending wedge and smooth convex surface diffraction coefficients. A mechanistic multiplication of those diffraction coefficients in terms of the field is depicted in equation (5.19):

$$D_T = D_{P_1M} \times D_{T-Wedge} \times D_{MP_2} = \frac{\overrightarrow{E_M}}{\overrightarrow{E_{P_1}}} \times \frac{\overrightarrow{E_M^{+}}}{\overrightarrow{E_M^{-}}} \times \frac{\overrightarrow{E_{P_2}}}{\overrightarrow{E_M^{+}}} \tag{5.19}$$

,where the negative and positive signs depicts the field state before and after effect of wedge model.

The overall nature of equation (5.19) corespond a linear system that includes diffraction coefficient of two smooth convex surfaces, decreasing exponentially with the angle of creeping based on equation (5.4), and static value of wedge diffraction coefficient for the same positioning of point of $M$and the antenna pairs from the body in accordance to equation (5.8). The linear nature of equation (5.19) give us the ability to proceed with a mechanistic manipulation of ordering of diffraction coefficients multiplication as depicted in equation (5.20):

$$D_T = D_{T-Wedge} \times D_{P_1M} \times D_{MP_2} = \frac{\overrightarrow{E_M^{+}}}{\overrightarrow{E_M^{-}}} \times \frac{\overrightarrow{E_M}}{\overrightarrow{E_{P_1}}} \times \frac{\overrightarrow{E_{P_2}}}{\overrightarrow{E_M^{+}}} \tag{5.20}$$

It is safe to assume the effect of wedge model can be considered an external factor to the linear system of smooth convex surfaces. This assumption helps with excluding the effect of wedge model when we speak in the context of creeping wave and smooth convex surface propagation. Based on this analogy and the fact creeping fields are continuous over a smooth convex surface [81], we can conclude $\overrightarrow{E_M^+}$ and $\overrightarrow{E_M}$ are the same at point M. We can re-write equation (5.20) as:

$$D_T = D_{T-Wedge} \times D_{P_2P_1} = \frac{\overrightarrow{E_M^+}}{\overrightarrow{E_M^-}} \times \frac{\overrightarrow{E_{P_2}}}{\overrightarrow{E_{P_1}}} \tag{5.21}$$

From equation (5.20) we can conclude, the total diffraction coefficient to capture far-field, near-field, and creeping waves behavior of first path in the proximity of human body is the total ratio of diffraction coefficients calculated in equations (5.8) and (5.4):

$$D_T = D_{T-Wedge} * D_{T-Creeping} \tag{5.22}$$

In conclusion, the first path path-loss is derived using equation (5.23), which reflects the effect of creeping diffracting, wedge-shaped diffraction, frequency and antenna pair distance from the human body [107][73]:

$$L = -10log\left(\frac{\lambda\,|D_T|}{4\pi\sqrt{R'R''(R'+R'')}}\right)^2 \tag{5.23}$$

The ToA (τ) of the first path will be computed geometrically using equation (5.24). For what has been shown in Fig. 1, the traveling distance for the first path is calculated from location of the transmitter to P_1 ($\overline{T_X\,P_1}$) , over the curvature of torso

($\overline{P_1\,P_2}$) and from P_2 to the receiver location ($\overline{P_2\,R_x}$) in question (21), c is the speed of wave propagation. The $\overline{P_1\,P_2}$ calculated using $R * \theta$, where R is the radius of torso and θ is the creeping angle.

$$\tau = (\overline{T_X\,P_1} + \overline{P_1\,P_2} + \overline{P_2\,R_x})\left({}^{1}/_{c}\right) \tag{5.24}$$

Following the same analogy that was described for blending UTD ray theory of wedge and smooth convex surface diffraction coefficients, a general propagation model for on and off body can be derived using UTD ray theory of wedge and smooth convex surface for different position of tip of the wedge on the same smooth convex surface (A , B , C) that is depicted in Figure 5.6.

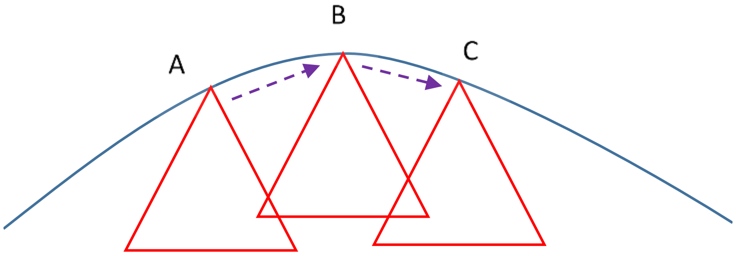

Figure 5.4 General propagation model for on and off human body using UTD ray theory of wedge and smooth convex surface .

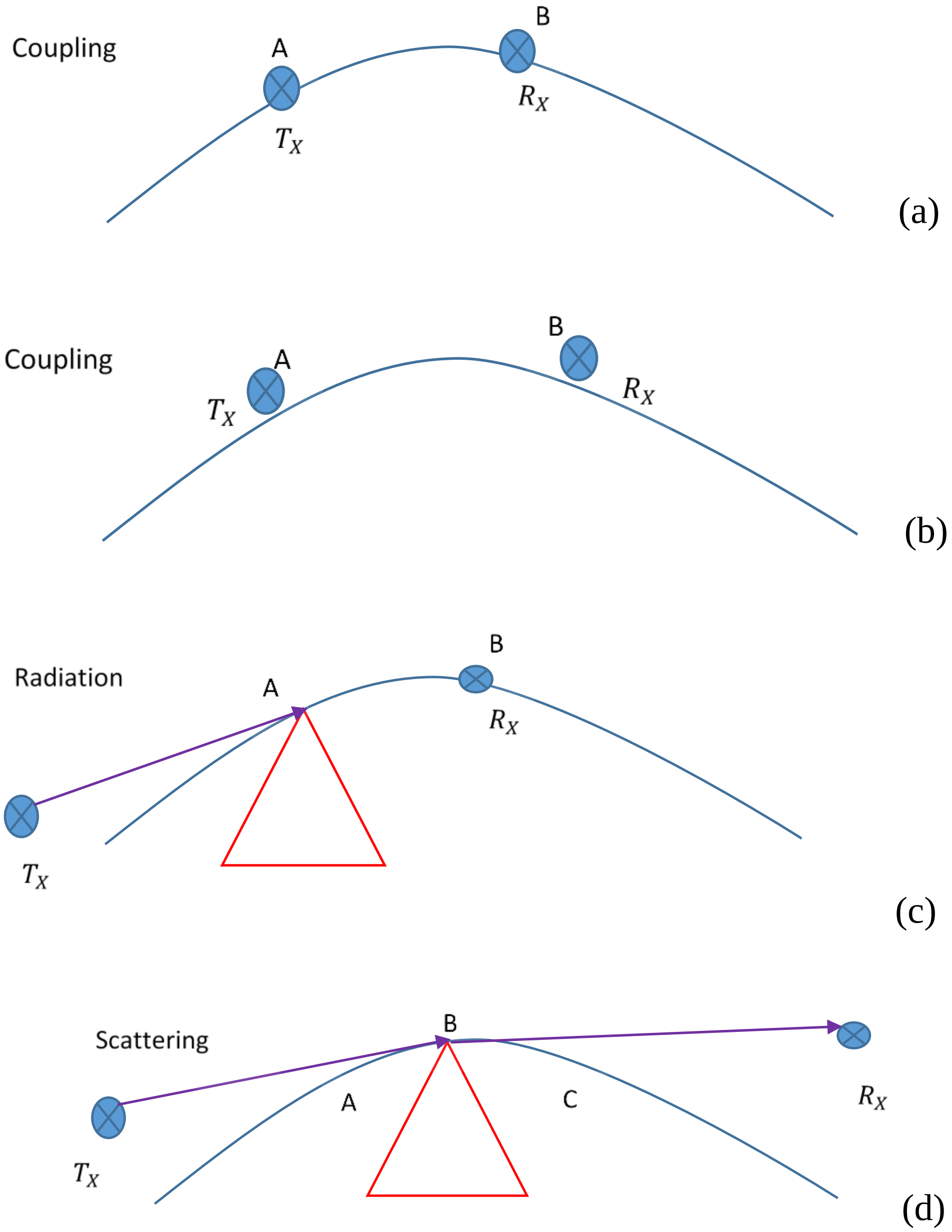

Figure 5.5 (a) coupling both field points on the surface (b) coupling both fields very close to the surface (c) radiation (d) scattering .

The specific form of general model depicted in Figure 5.4 are the coupling, radiation and scattering models that are depicted in Figure 5.5 ,which are extensively described section 2.5.3. Figure 5.5 – d is the scattering solution that we used in this chapter, and in the upcoming chapter we utilized the radiation model that will be described in details.

5.3 Comparison of Computation with Empirical Results

The accuracy and validity of measurement campaign for the scattering scenario discussed in measurement setup in section 5.2.1, in respect to the noise, reflection and scattering from surrounding environment are confirmed by an anechoic chamber. We can verify the receiver positioning within the transition region via calculation of the half-width (w) of transition zone using equation (5.6) and the height of receiver antenna (h) from the shadow boundary (SB) using simple geometry involved (α) from equation (5.13) and the antenna separation. Both (w) and (h) are depicted in Figure 5.3 - b. It is clear the circumstances the receiver antenna falls into transition is directly associated to the operating frequency, antenna pair separation, size of sidelopes from antenna pairs to the torso and the radius of cylinder simulating the torso.

Using equations (5.4) and (5.8), for a TM polarization, we attempt to calculate the diffraction coefficients for creeping and wedge-shaped scenarios, which are depicted in Figure 5.6 for a valid range of creeping angles (θ) with consideration of lower-bound condition of θ = 1.0003 (Rad) derived from equation (5.3). The result of Figure 5.6 shows; while diffraction coefficient value for creeping waves is less than wedge-shaped model, the creeping wave diffraction coefficient decays exponentially with angle (θ) ,which aligns with what has been suggested in [73][106] . To discuss this behavior from localization perspective, as the creeping angle increases, the DP vanishes, resulting in a gradual transition of LoS to NLoS (NDDP or UDP) condition between transmitter and receiver. We also see the diffraction coefficient of wedge-shaped scenario stays independent of creeping angle (θ) , something that is understandable as the pivot of the wedge (peak of triage in Figure 5.3) has a static position for different creeping angles. This analysis of UTD ray theory of wedge and smooth convex surface models was the driving force behind leveraging wedge model as an external factor to the linear system of total diffraction coefficient in equation (5.20).

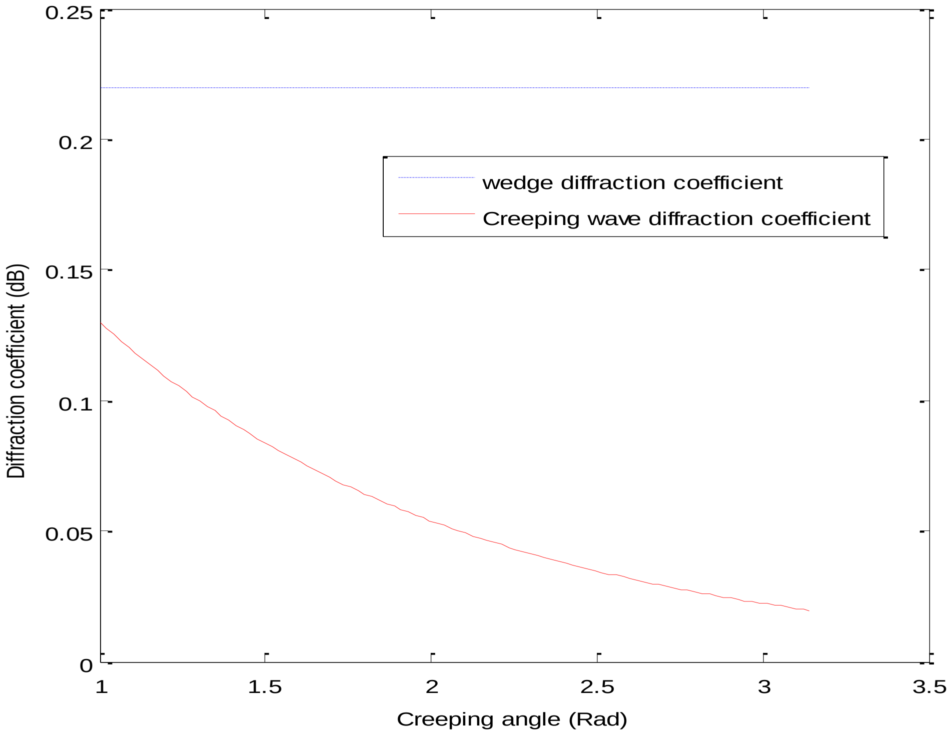

Figure 5.6 diffraction coefficient for creeping wave and wedge-shaped scenarios for a range of creeping wave angles.

Subsequently, Figure 5.7 depicts the first path path-loss around the torso for a range of creeping angles. This is the result of equation (5.23) with consideration of ~10.6 cm cylindrical cross-section radius replacing the torso in the measurement setup. Since in our experiment antenna pair is positioned to the opposite side of human torso with 180 (degree) separations, we should expect a maximum value of total path-loss for the diffracted first path, which indeed confirmed by wideband statistical study of [63] for 900 MHz experimental scenario. It is safe to assume, this maximum path-loss is the result of diffracted rays around the torso and contribution of penetrating waves can be neglected [63]. As a result, the maximum path-loss of 64.84 dB for a creeping angle of 3.142 Rad is derived from Figure 5.7.

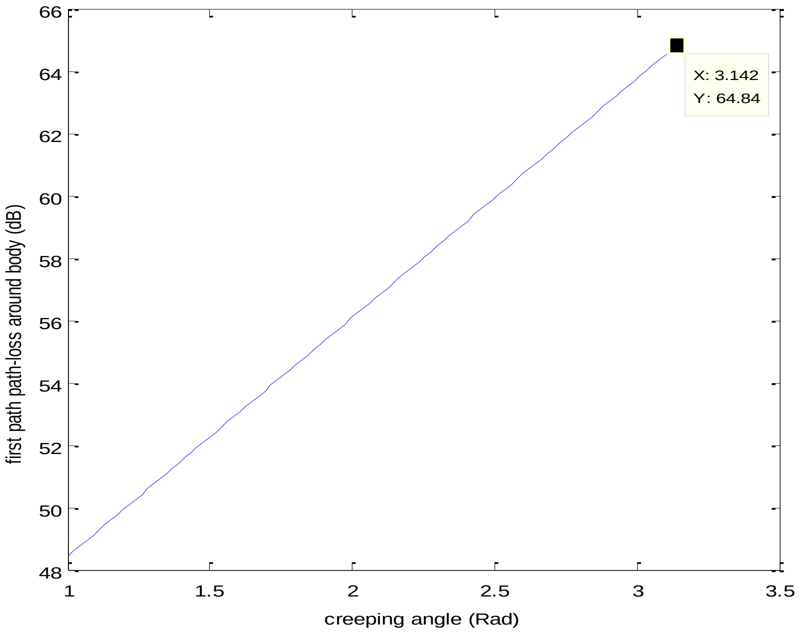

Figure 5.7 first path path-loss for a range of creeping wave angles.

Furthermore, Figure 5.8 depicts first path ToA for a range of creeping angles based on applicability of equation (5.24), in which for a creeping angle of 3.142 Rad, we can capture the first path ToA of 2.07 ns. The corresponding ToA, maps to 0.1210 m ranging error manifested by placement of torso in between the antenna pair for our validation scenario. The size of creeping is also an indication of traveling path on the surface of torso, approximately half the cylinder diameter.

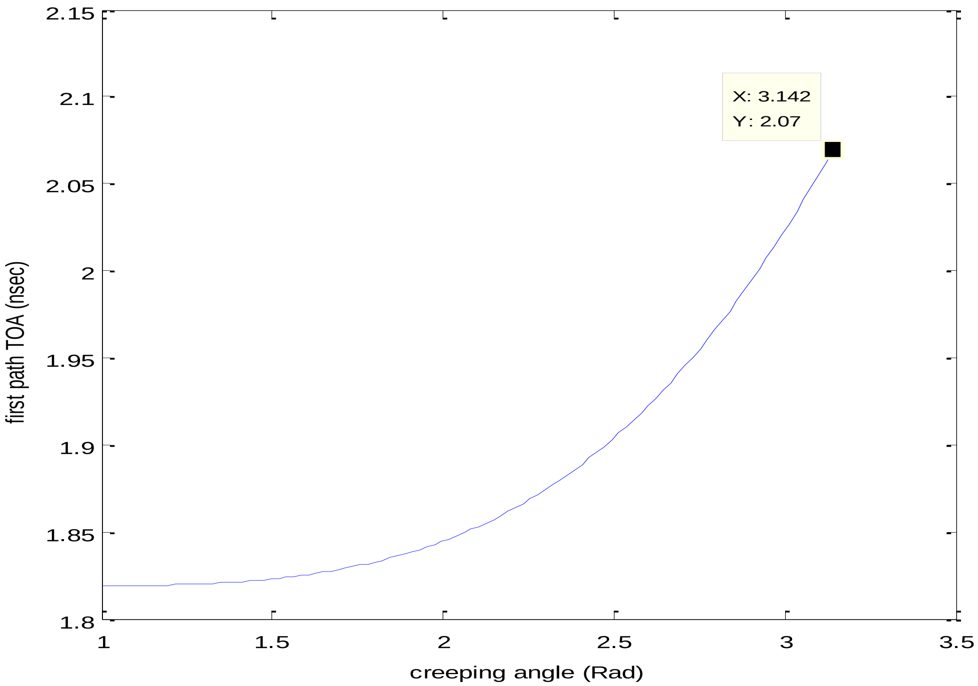

Figure 5.8 first path TOA for a range of creeping wave angles.

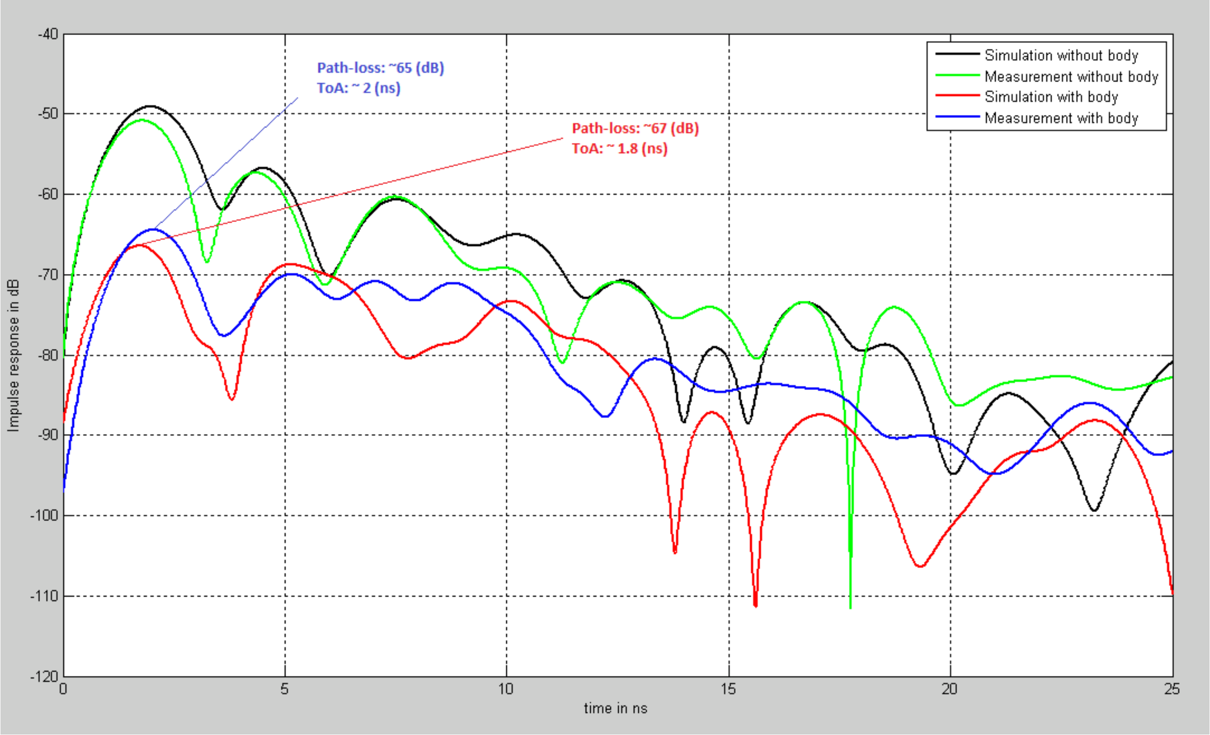

Figure 5.9 Broadband measurement result compared to HFSS simulation (FEM solver) for a scenario that human torso is placed between Tx and Rx.

The path-loss and ToA of the first path derived from the analytical UTD approach (64.84 dB,2.07 ns) shows close agreement with the wideband measurement (65 dB, 2 ns) and HFSS simulation results (67 dB, 1.8 ns) depicted in Figure 5.9. The green and the blue graphs provide the measurement and the black and the red graphs provide HFSS [21] simulation results , which is a FEM solver, before and after human torso placed in between the antenna pair. The blue and red graphs are mainly of interest as the path-loss is a relative measure in our analytical calculation.

5.4 Summary

We proposed an analytical UTD approach to predict the behavior of shortest diffracted path, known as the first path, for ToA-based indoor localization and accurate ranging for a scattering scenario in the proximity of human body and in particular in the transition region. This analytical approach is based on the applicability of UTD conductor wedge path-loss model previously used for communication purposes in an urban area, and a custom geometrical formulation to calculate ToA and DME of the first path. With the consideration of past struggles to take into account the effect of transition function formulation embedded within the UTD ray theory of smooth convex, the UTD ray theory of smooth convex surface is applied to the wedge path-loss model in terms of creeping wave diffraction coefficient. The mechanics happens with a comprehensive analysis of EM fields on the surface of torso to help in blending the smooth convex and wedge diffraction coefficients into the wedge path-loss model. Embedded in the UTD conductor wedge path-loss model, the wedge diffraction encapsulates the transition function, in which it will contribute to the precise prediction of the fields in the transition region and in the proximity of human body. The model introduced spans across a variety of antenna positioning in respect to human body by addressing creeping waves for on-body, far-field and near-field waves for off-body propagations. It shown the analogy and the approach used for the scattering solution proposed in this chapter can be generalized, based on applicability of UTD wedge and smooth convex surface models, to analytically model the coupling and radiation scenarios in the proximity of human body as well.

To validate our approach, we compared the result of the analytically calculated path-loss and ToA of first path with wideband measurement and HFSS simulation (a FEM solver) for a scenario where the receiver is located in the transition region and away from the body $(\sim\lambda/3)$, and provided our prediction for NLoS ranging error manifested by human torso obstructing the LoS. The analytical approach discussed in this paper is proposed as a enhancement to existing RT algorithm for human body ToA-based indoor localization.

In the next chapter of this thesis we discuss an analytical approach to analyze effect of angular motion of human body for a radiation scenario.

Chapter 6 Ray Optics and Effects of Angular Motion of Human Body

6.1 Introduction

Considerting the overheads stemmed from complexities and required computational resources (i.e. CPU, memory) associated with EM computation methods and as an extension to the UTD analytical effort for modeling ranging errors in the proximity micro-metals, has shaped a desire to adopt UTD-based techniques for BAN as a substitute. We can consider this UTD solution as an enhancement to existing RT algorithm to count for effect of diffraction in proximity of human body parts. There has been multiple research studies in Body Area Network (BAN) , that have in the past pursued ray theory based on applicability of a conductor cylinder for coupling, radiation and scattering solutions. The Zhao et al. in [22], Alves et al. in [99] and Zasowski et al. in [100] have followed the creeping theory - diffraction phenomena of rays around shadowed surface of smooth convex body - and coupling functions for on-body propagation solutions introduced by [83][98][84] respectively, when the height of antenna from the body surface are in small fractions of wavelength (~ $\lambda/20$ or less). On the other hand, Ghaddar et al. in [19] based on applicability of [83], Koutitas et al. in [102] based on applicability of

[80][98][84], and Lee et al. in [42] based on applicability of [103][104] have investigated scattering scenarios based on solutions offered for off-body or a hybrid version of off-body and on-body propagation solutions.

In particular the main focus of studies conducted by [19][99][100] is the analysis of channel profile in proximity of human body, and in respect to angle or position of antenna pair. The authors in [22] have followed a UTD approach based on applicability of surface field (*Fock* coupling) functions and coupling coefficients introduced in [80], also, they have compared the result of time-response derived from computed frequency-response with FDTD and measurement for on-body channel characterization. However, there has been less consideration to the diffracted rays around the transition zones. Reference [102] counts for the effect of parallel shadow boundaries on the sides of human body in the deep shadow region and away from shadow boundary, where transition function reaches unity, for a scatterer case. Validation of their approach in scheming the path-loss and the delay derived from frequency-response is rather limited to the scenario the receiver is mounted 6 mm ($h = \lambda/10$ for 5 GHz) from surface of the body. This approach explores the effect of diffracted rays in transition zone for the coupling and the creeping conditions. Alternatively, [42] entertains the idea of validating the ranging base on the time-response derived from frequency-response and based on applicability of [103][104]. Despite uncertainties in the trunk, head and hand geometry and transceiver location in respect to the body in the validation scenarios, it is palpable the primary focus of proposed procedure neglects cross-propagating rays over the cylinder, which bounds the applicability of solution around the transition zones. Additionally, The UTD solutions that are discoursed in aforementioned studies are predominantly based on applicability of conductor cylinder for scatterer or on-body propagation scenarios, leaving this solution inadequate to count for effect of angular motion of human that is confirmed by statistical models provided by [34]. Although [42] has explored an elliptical solution to human body, a static position is assumed for the validation scenarios.

The RT remains as an important simulation tool widely used in indoor to model RF propagation when there are obstacles. In addition to the above references, [108][109][110] in recent years have conducted studies to help with improving the accuracy, computational resources and complexity of RT algorithm for simulations in the proximity of human body, that conclude current state of art for RT algorithm.

In detail, [108] confirms modeling the human body as a cylinder in the RT environment provides more accuracy in some specific scenarios compare to knife-edge, blade and parallel pipe UTD models and absorbing material would require less computation complexity compare to conductor and dielectric. [109] proposes a twin cylinder model for moving head and human body shadowing in 60 GHz WLAN to help with accuracy of human body in RT simulation, and [110] leverages additional statistical models under different settings to help with accuracy of current RT algorithm for modeling effect of human movement on indoor propagation.

In the upcoming sections we explore an alternative UTD approach to above studies applicable to a diverse propagation scenarios such as on-body or off-body propagation solutions in proximity of human body. A comprehensive dive into the technical details of aforementioned proposal will be discussed , that explores the creeping theory introduced by [80][106] along with wedge-shaped conductors model reported in [62] - diffraction phenomena of rays in proximity of a conductor wedges with finite wedge angle - introduced by to account for behavior of far-field and near-field rays in proximity of human body. Particularly, leveraging wedge-shaped diffraction coefficient and Fresnel function, the proposed UTD model can count for cases the receiver is localized in the transition zone and away from the body $(\sim\lambda/3)$, which provides a good accuracy compared to the previous studies that may have experienced instabilities in their validations in that region.

The primary focus would be to calculate the path loss, ToA and Distance-Measurement-Error (DME) of the first path in OLoS condition, when LoS blocked by the human body and the receiver orientation falls within the transition region. While [102][42] leverage a subjective creeping angle in their calculations for on-body propagation, in this paper, a creeping angle is analytically calculated, which appropriately suits the experimental scenario. The analytical UTD approach operates based on applicability of desired center frequency to compensate for limitations associated to computational resource of large and complex environments. The validation procedure consists of wideband measurements performed by a vector network analyzer operating at 900 MHz, sweeping 100 MHz of bandwidth, and HFSS simulation.

Soon after, leveraging creeping theory and wedge model from above discussion with an addition of screen conductor solution - diffraction phenomena of rays in proximity of a screen made of a thin conductor , based on applicability of elliptical geometry for human torso in angular motion is investigated, which is the focus of this paper. The validation scenario consists of static positioning of a transmitter antenna placed 5 m away from a receiver mounted on the human torso and in rotational motion$[0^0, 360^0]$. UWB measurement conducted at 30^0 intervals used to validate the analytically calculated ToA and path-loss of first path for 3-8 GHz of bandwidth.

Potential adjustments to the aforementioned model are proposed to compensate for path-loss oscillations in transition regions in proximity of human torso. The proposed model is leveraged to model path-loss, DMA and ToA for various positioning of transmitter antenna in the same scenarios - in respect to human torso in angular motion and mounted receiver on its chest.

The reminder of this chapter is organized as following; Section 6.2 covers analysis of effect of angular motion of human torso on ToA-based indoor localization systems when a transmitter has a static position in respect to the receiver that is mounted on the human chest including discussion on modeling LoS in section 6.2.1, OLoS in section 6.2.2 and results and discussion in section 6.3 respectively. Section 6.4 discussed proposed enhancements to the model to overcome some instability in the aforementioned model and section 6.5 explores various position of antenna. Finally section 6.6 concludes the chapter.

6.2 Analysis of Effect of Angular Motion of Human Torso

In this section, analysis of effect of angular motion of human torso will be investigated. To proceed with an analytical UTD ray theory and geometrical ray optics formulation to compute the path-loss, DME and ToA of the first path around human torso in angular motion, calls for geometrical improvements from a circular cylinder model to an elliptical cylinder. The solution helps to account for a realistic geometry of torso that brings into consideration the effect of hands and shoulders as depicted by Figure 6.1-a. Two cylinder with radius R are considered crossing each other at points, M and N , resulting in an overlapped elliptical cross-section area that is depicted by Figure 6.1-b. This elliptical cross-section is considered the overhead view of the torso in respect to the human head such that, d represents the width of human torso (shoulder-to-shoulder size) and x captures the depth of human torso (size of chest to back). Using d and x, the radius of the overlapping cylinders can be calculated using equation (6.1) , which further has a vital role in calculation of creeping waves in equations (5.1) (5.2) and (5.3):

$$(R - {}^{x}/_{2})^2 + ({}^{d}/_{2})^2 = R^2 \tag{6.1}$$

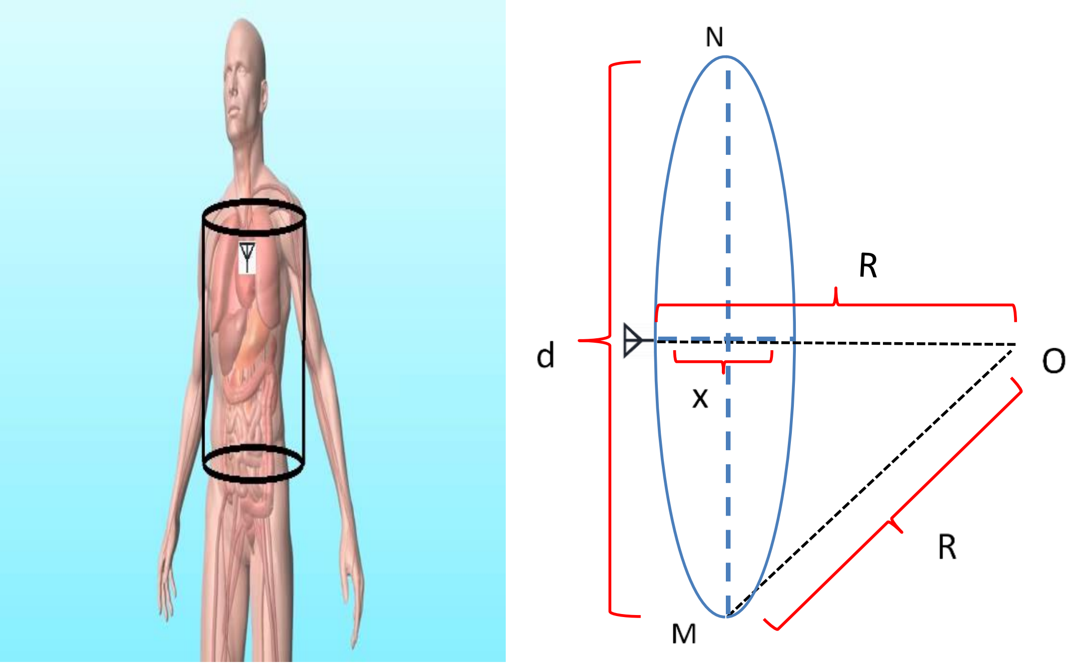

(a) (b)

Figure 6.1 (a) Human torso as an elliptical cylinder with mounted antenna on the chest. (b) overhead view of human torso geometry with elliptical cross-section.

The overall UTD ray theory and geometrical ray optics properties previously introduced for scattering cases are expanded and employed in a new fashion for radiation scenarios. The experimental scenarios involve a receiver antenna mounted on a human chest (over the torso) facing the transmitter that is positioned at the same

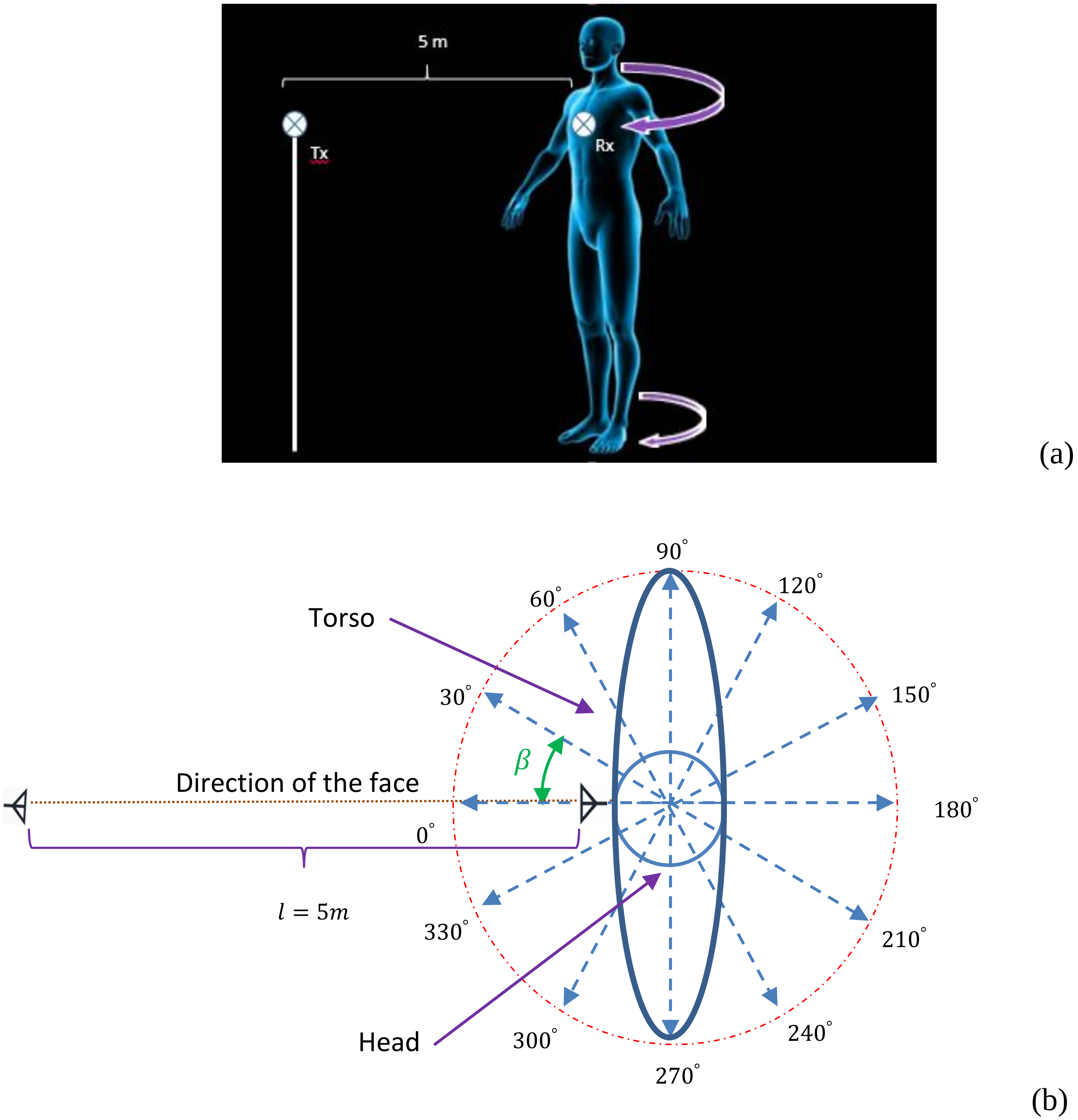

Figure 6.2 (a) Radiation scenario by human body in angular motion (b) top view cross section of torso depicting angle β between direction of the face/torso and the original transmitter/receiver reference line.

height as human torso and 5 m away (Figure 6.2 - a and Figure 6.2 - b) operating at 5.5 GHz operating frequency with 5 GHz bandwidth. Analytically calculated path-loss, ToA, and DME of the first path is validated with the empirical measurements using UWB signal as the human torso rotates in a clockwise angular motion (as β increases in Figure 6.2-b). The same measurement system discussed in section 5.2.1 will be adopted for validation of new proposed analytical UTD ray theory and geometrical ray optics procedures for the experimental scenario depicted in Figure 6.2 – a. The empirical measurement incdes a pair of UWB antenna (Skycross SMT-3TO10M) with TM polarization, which implies addition of a power amplifier (3 – 8 GHz, 30dB) connected to the VNA (Agile E8363). The width and the depth of subject human torso considered for validation process are 40 cm and 16 cm respectively. There are 50 measurements attempts at intervals of 30^o spanning a complete ration of torso for $\beta = [0° , 360°]$. This is done as the subject human and mounted antenna on its torso (chest) rotate clockwise in respect to the transmitter. The average path-loss, DME , and ToA at each interval will be used to validate the result of proposed analytical approach.

$$\beta = \{0° , 30°, 60°, 90°, 120°, 150°, 180°, \ldots , 360°\} \qquad (6.2)$$

Measurement scenarios are divided into LoS or OLoS conditions provided the human body blocks the LoS between transmitter and receiver. The angular rotation (β) can further classify to scenarios (S) depicted as :

$$S = \begin{cases} LoS, & \beta \in [\,0°\,,90°]\ and\ \beta \in [\,270°\,,360°] \\ NLoS, & \beta \in (90°, 270°) \end{cases} \tag{6.3}$$

6.2.1 Modeling for LoS Condition

Analytical calculation of the path-loss and ToA of the first path for a LoS condition ($\beta \in [\,0°\,,90°]\ and\ \beta \in [270°\,,360°]$) depicted in Figure 6.3 are rather straight forward, as the Friis free space depicted in equation (6.4) , can be leveraged.

$$PL = G_t G_r (\frac{\lambda}{4\pi r})^2 \tag{6.4}$$

In this equation, $G_t$and G_r are transmitter and receiver gains, respectively, and it is safe to assume them as unity. The r is the direct path between the transmitter and the receiver, which can easily be calculated for any β. For these two scenarios, the ToA derived from equation (6.5), where c is the speed of wave propagation:

$$\tau = {}^{r}/_{c} \tag{6.5}$$

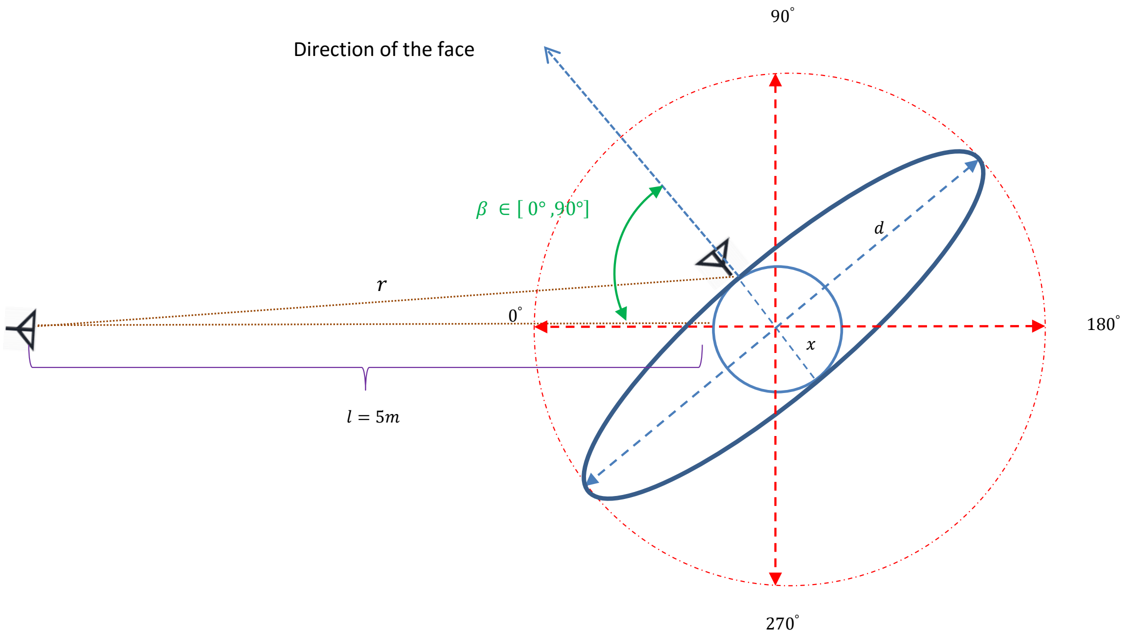

Figure 6.3 LoS conditions for β ∈[0° ,90°], where free space model can be used to calculate the direct path path-loss and ToA.

6.2.2 Modeling for OLoS Condition

Analytical calculation of the path-loss and ToA of first path, for an OLoS condition ($\beta \in (90°, 270°)$), is rather complex. Figure 6.4 depicts a scenario, in which the clockwise angular rotation of human torso localizes position of the mounted receiver on the chest, in an angle of $\beta \in (90°, 270°)$, in respect to the transmitter antenna. For these scenarios, the human body blocks the DP between antennas pair resulting in diffraction of first path. Upon diffraction of the first path, creeping waves fashion in different direction over the body, but as [34] reflects, the creeping waves around the shoulder and the human torso reach the receiver fastest. These rays are referred to as first path around human torso in this paper.

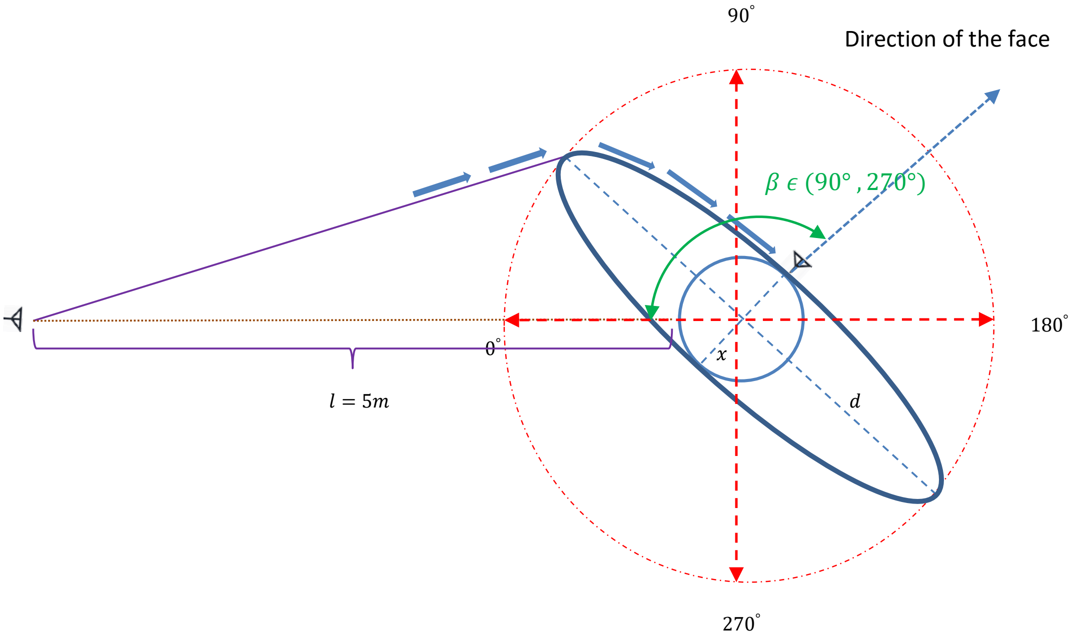

Figure 6.4 OLoS condition for β ∈(90°,270°), where human body blocks the DP.

As depicted in Figure 6.5, to proceed with our analytical approach to calculate the path-loss and ToA of first path around the torso for scenarios of $\beta \in (90°, 180°)$ and $\beta \in (180°, 270°)$, the portion of body that blocks the DP is replaced with a wedge model that has isosceles triangle cross-section,. The right leg of triangle lies on the line representing the width of the torso (d in Figure 6.1-b) and base of triangle (l in Figure 6.5) lies between transmitter and receiver at angle $\beta = 0$. The same equations (5.1) - (5.23) previously used for scattering by the conductor cylinder model will be deployed with the exception of redefinition of angles α , φ and φ' in equations (5.5), (5.13) - (5.15) :

$$M = \begin{cases} \pi - 2\beta, & \beta \in (90°, 180°) \\ 2(\beta - \pi), & \beta \in (180°, 270°) \end{cases} \tag{6.6}$$

$$J = \begin{cases} {}^{d}/_{2} \, sin \, (\beta - {}^{\pi}/_{2}) \, , & \beta \in (90°, 180°) \\ {}^{d}/_{2} \, sin \, ({}^{3\pi}/_{2} - \beta) \, , & \beta \in (180°, 270°) \end{cases} \tag{6.7}$$

$$T = \begin{cases} (l + {}^{x}/_{2}) - \left({}^{d}/_{2} \; cos(\beta - {}^{\pi}/_{2})\right), & \beta \in (90°, 180°) \\ (l + {}^{x}/_{2}) - \left({}^{d}/_{2} \; cos({}^{3\pi}/_{2} - \beta)\right), & \beta \in (180°, 270°) \end{cases} \tag{6.8}$$

$$\alpha = tan^{-1}({}^{J}/_{T}) \tag{6.9}$$

$$\varphi' = \begin{cases} \beta - {}^{\pi}/_{2} - \alpha, & \beta \in (90°, 180°) \\ {}^{3\pi}/_{2} - \beta - \alpha, & \beta \in (180°, 270°) \end{cases} \tag{6.10}$$

$$\varphi = 2\pi - M - tan^{-1}({}^{x}/_{d}) \tag{6.11}$$

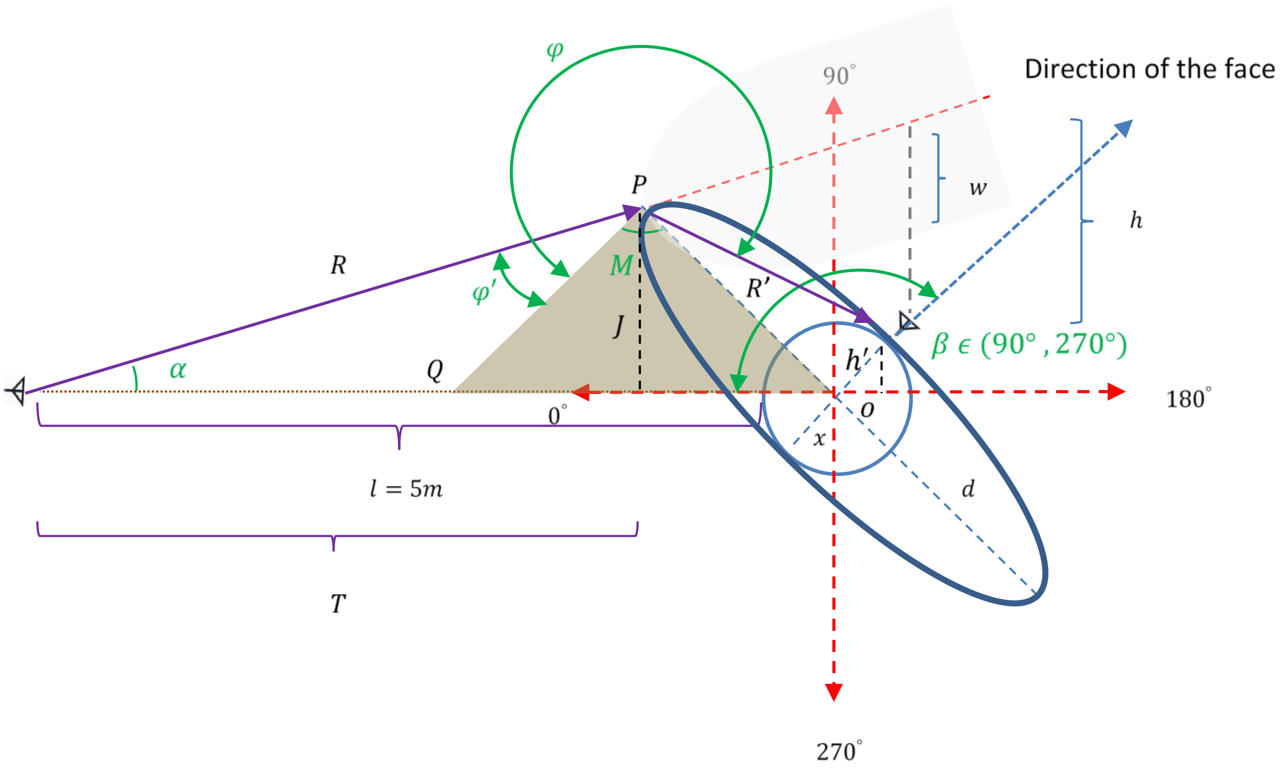

Figure 6.5 Conductor wedge model to calculate path-loss and ToA of the first path.

To discuss equation (5.22) in terms of electromagnetic fields, it is known the wedge and creeping diffraction coefficients are the electric field ratio of the diffracted rays to the incident rays in proximity of the wedge and the torso respectively. The total diffraction coefficient corresponds to the electric field ratio of the rays diffracted by the wedge and creeping over the torso into the receiver with consideration of the incident rays traveling over the torso are the same as diffracted rays by the wedge ($\overrightarrow{E_W^+} = \overrightarrow{E_T^-}$) and rays received at the receiver are the diffracted (creeping) rays from the torso) ($\overrightarrow{E_T^+} = \overrightarrow{E_R}$). The subscripts W, T and R correspond to the wedge , smooth convex surface of torso models and the receiver antenna respectively. The negative and positive signs corresponds to rays incident and diffracted by the wedge and the smooth convex surface at point P and over the torso respectively.

$$D_{Total} = \frac{\overrightarrow{E_R}}{\overrightarrow{E_W^-}} = \frac{\overrightarrow{E_W^+}}{\overrightarrow{E_W^-}} \times \frac{\overrightarrow{E_T^+}}{\overrightarrow{E_T^-}} = D_{T-Wedge} * D_{T-Creeping} \qquad (6.12)$$

The creeping angle (θ), which is the angle of creeping wave from one side of human torso to the mounted antenna on the chest is $\frac{\pi}{2}$. This angle stays constant throughout the NLoS computations as the torso and the mounted antenna on the chest rotate clockwise. The R and R' are the sidelopes to the peak of the wedge calculated as following:

$$R = \sqrt{T^2 + J^2} \qquad (6.13)$$

$$R' = \sqrt{{x/2}^2 + {d/2}^2} \tag{6.14}$$

Once the $D_{T-Wedge}$ and $D_{T-Creeping}$ are calculated using equations (5.7) and (5.4), it is safe to assume, that R' can replace the curvature of human torso in the formulation to proceed with modeling the path-loss of the first path. Consequently, equation (6.15) will be used to calculate the ToA of first path. It is the duration of first path traveling the direct distance from the transmitter to the point that human body blocks it and creeping over the curvature of torso to reach the receiver.

$$\tau = (R + R_C\,\theta)\left({1}/{c}\right) \tag{6.15}$$

The R is the free space distance DP travels from transmitter to the point of intersection, where body blocks it. R_C is the curvature radius of torso derived from the equation (6.1), θ is the creeping angle and c is the speed of wave propagation.

As we transition to $\beta = 180°$, one of experimental scenario's depicted in Figure 6.2-b, it is safe to assume the two legs of isosceles triangle that is cross section of the wedge in Figure 6.5 ($\overline{QP}$ and $\overline{PO}$) overlap each other resulting in $\widehat{M}$ reaching 0°, and the wedge-shaped model transitioning to a conductor screen model as depicted in Figure 6.6.

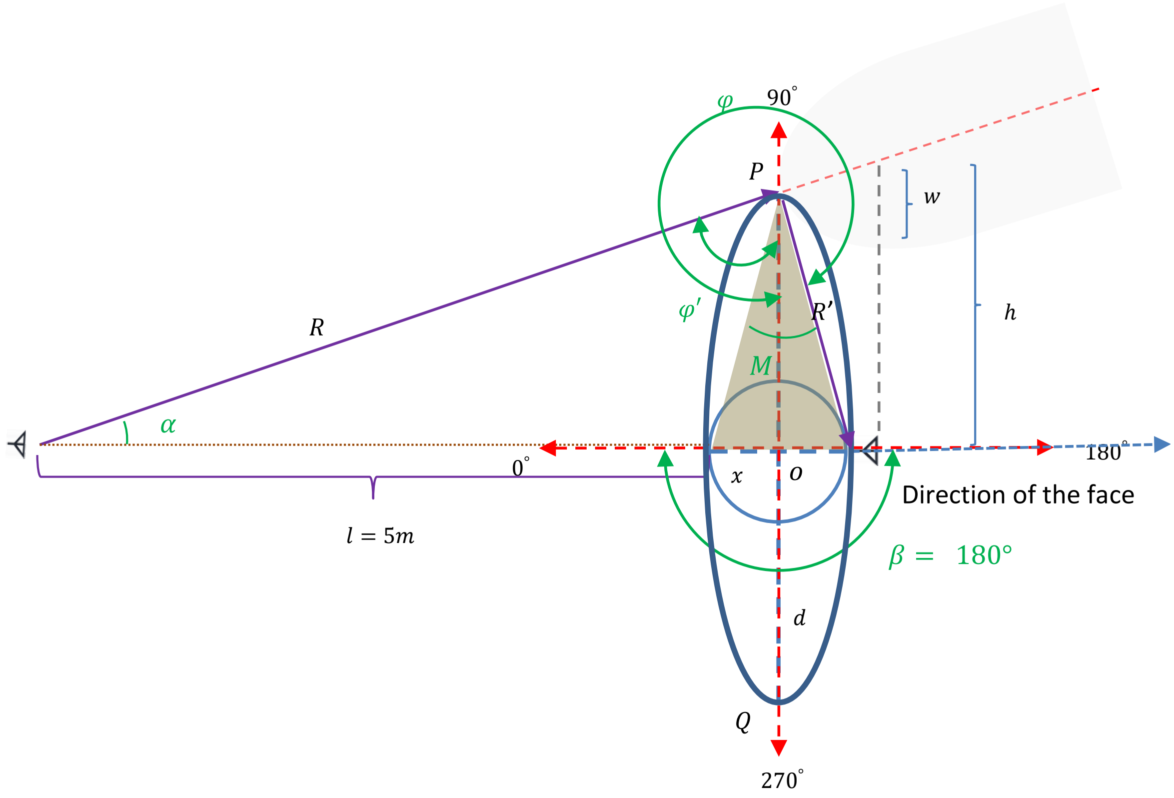

Figure 6.6 Conductor screen model to calculate path-loss and ToA of the first .path for β=180°.

The changes required to proceed with conductor screen are related to angles M , φ and φ' and replacing conductor screen diffraction coefficient ($D_{T-Screen}$) definition with wedge diffraction coefficient ($D_{T-Wedge}$).

$$M = 2\tan^{-1} {}^{x}/_{d} \tag{6.16}$$

$$\varphi' = {}^{\pi}\!/_{2} - \alpha \tag{6.17}$$

$$\varphi = 2\pi - {}^{M}\!/_{2} \tag{6.18}$$

$$D_{T-Screen} = \frac{-1}{2\sqrt{2\pi k}} \left\{ \frac{1}{cos\,\frac{\varphi - \phi'}{2}} + \frac{\Gamma_{E,H}}{cos\,\frac{\varphi + \phi'}{2}} \right\} \tag{6.19}$$

6.3 Results and Discussions

This section provides the result of analytical approach derived from applicability of free-space, conductor wedge and screen models discussed in sections 6.2.1 and 6.2.2, and their validation with the measurement scenarios discussed in the early section of 6.2. While the measurement results are discretized for intervals of $30°$ scenarios, the analytical solution is rather continuous (intervals of $1°$) spanning across a complete rotational motion for $\beta \in [0°, 360°]$ scenarios. Figure 6.7, Figure 6.8, and Figure 6.9 depict the result of analytical calculation of ToA, DME and the path-loss of first path, and their comparison with the measurements respectively. In those figures, there are two instances of free space measured data at angle $\beta = 0°$, one of which includes the effect of human body when the receiver is mounted on the human chest facing the transmitter.

6.3.1 First Path ToA

Figure 6.7 depicts the result of analytical calculation of ToA for the first path as the human torso and mounted receiver on the chest rotate clockwise in an angular motion for $\beta \in [0°, 360°]$. For angles involved in LoS scenarios ($\beta \in [0°, 90°]$ and $\beta \in [270°, 360]$), the equation (6.5) is used to calculate the ToA of the first path. As depicted in Fig. 3a, for scenarios of $\beta \in [0°, 90°]$, the ToA increases as the torso rotates clockwise in respect the transmitter imposing longer distance between the antenna pair. In case of $\beta \in [270°, 360]$however, the ToA value decreases as torso and mounted antenna rotates clockwise toward the transmitter resulting in a shorter distance between antenna pair. As the torso rotates from $90°$ to $91°$ scenario, a jump in ToA value is observed. This is due to a transition from LoS to NLoS condition, calling for NLoS condition equation (6.15) at $91°$. A comparison of Fig. 3a and 3b, testifies to the fact the distance first path travels in a NLoS scenario is longer than LoS scenario, which is indeed confirmed by equations (21) and (36). The same analogy applies when the torso rotates from $270°$ to $271°$, but this time there is a transition of NLoS to LoS resulting in degradation of ToA.

For a NLoS condition with $\beta\ \in (90°, 270°)$ scenarios depicted in Figure 6.4, the equation (6.15) is used to analytically calculate the first path. In these scenarios, ToA captures the time the first path travels a distance (R) until blocked by human torso and diffracted rays travel a creeping distance ($R_c\theta$) over the curvature of torso to reach the receiver. As we discussed in the previous sections, the creeping distance stays constant for the duration of the time torso rotating in a NLoS condition with $(\theta = \frac{\pi}{2})$. As a result, while $R_c\theta$ stays constant as the torso rotate for $\beta \in (90°, 180°]$, ToA of the first path increases with R. The same analogy applies to $\beta\ \in [180°, 270)$ scenario but this time the ToA decreases with R.

There are two instances of free space measured ToA at angle $\beta = 0°$. The one with the larger ToA corresponds to the effect of human body when the receiver is mounted on the human chest facing the transmitter.

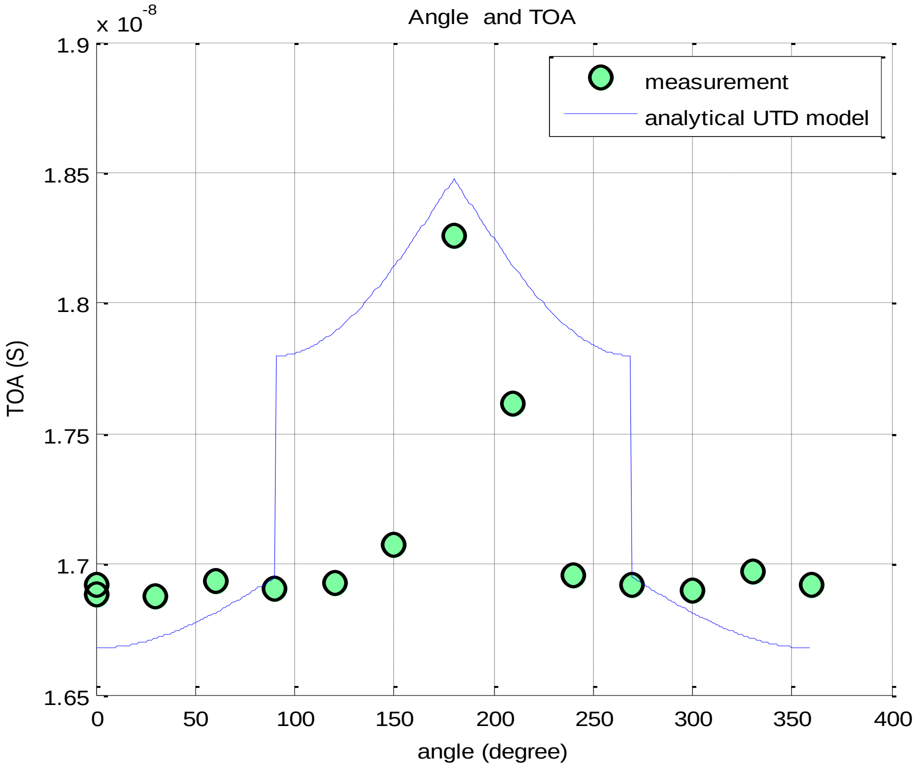

Figure 6.7 Comparison of analytical model and measured ToA of first path for β ∈[0°,360°] scenarios.

6.3.2 First Path DME

The DME presents the difference between expect and actual distance that first path would travel. Figure 6.8 depicts the result of analytical calculation of DME for the first path as the system rotate clockwise for $\beta \in [0°, 360°]$. In the analytical calculation, the expected travel distance of first path is the direct path between transmitter and the receiver independent of any objects blocking the path while the actual distance of first path simply derived from ToA depicted in Figure 6.7 for LoS and NLoS scenarios. As a result, the DME results provided in Figure 6.8 follows the same pattern as ToA graph in Figure 6.7.

For a LoS scenario of $\beta \in [0°, 90°]$ and $\beta \in [270°, 360]$ the expected and actual distance are the same and as a result graphs shows a flat horizontal line. For scenarios system transitions from LoS to NLoS (from $90°$ to $91°$angle) continues in NLoS condition ($\beta \in (90°, 270°)$) , and transitioning back from NLoS to LoS (from $270°$ to $271°$) we observe the same behavior as ToA , which follows the same analogy described for ToA calculation.

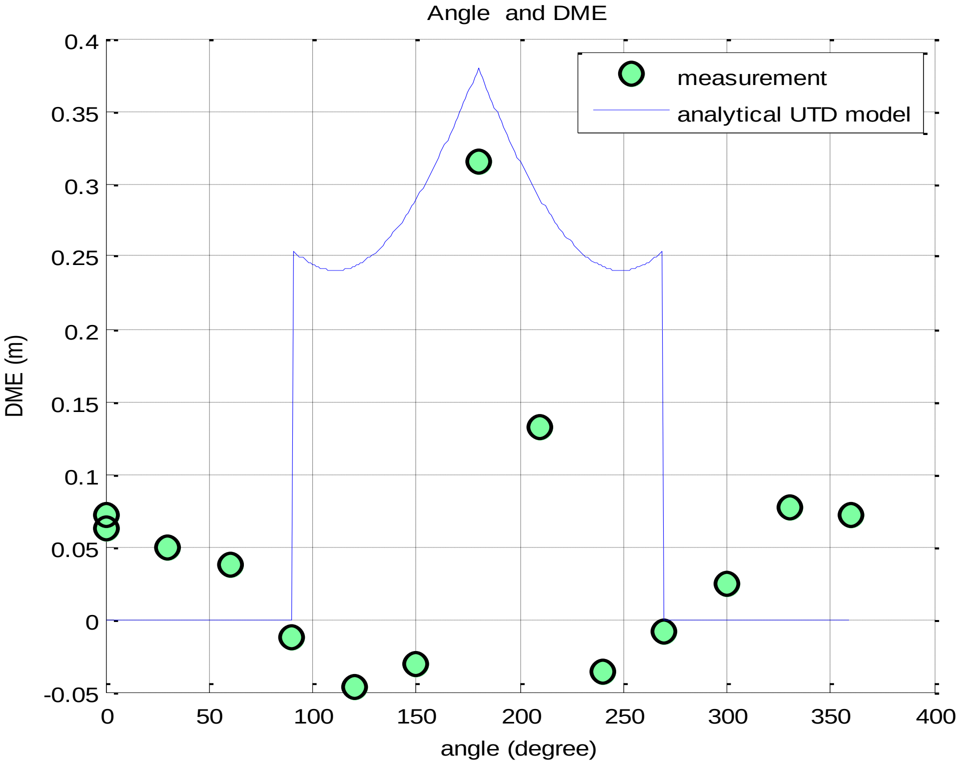

Figure 6.8 Comparison of analytical model and measured DME of first path for β∈[0°,360°] scenarios.

6.3.3 First Path Path-loss

Figure 6.9 depicts the result of analytical calculation of path-loss and validates the results with the actual measurement. For LoS condition with $\beta \in [0°, 90°]$ and $\beta \in [270°, 360]$ scenarios, the result of analytical approach - based on applicability of equation (6.4) - appears as a straight line. In reality, as the torso rotates clockwise, for $\beta \in [0°, 90°]$ scenarios the path-loss increases slightly with the antenna pair distance increasing. For the scenarios involved $\beta \in [270°, 360]$, the path-loss slightly decreases as the distance between antenna pair declines.

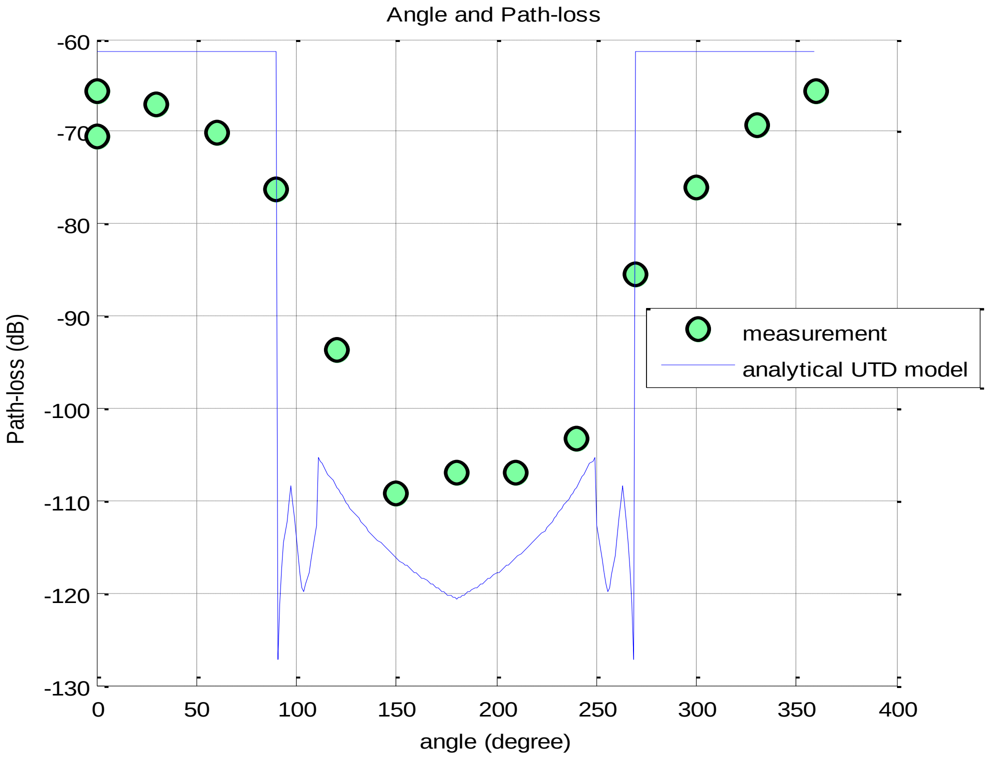

Figure 6.9 Comparison of analytical and measured path-loss for β∈[0°,360°] scenarios.

A strong degradation in path–loss is observed as torso rotates from $90°$ to $91°$angle. This is due to the fact the first path between transmitter and the receiver is blocked by the torso resulting in transitioning from a LoS to a NLoS condition. At $90°$, the free space path loss model provided in equation (6.4) is used, while the total path-loss at $91°$ is based on applicability of equations (5.22) and (5.23) , which counts for diffraction of first path around the torso, and creeping over torso curvature to reach the receiver antenna. The condition is rather different for the case torso rotates from $270°$ to $271°$ as the torso transition from NLoS to a LoS condition, resulting in a large improvement of the path-loss. The NLoS scenarios $\beta \in (90°, 270°)$ are further divided in two categories. While calculation of path-loss is based on applicability of equation (5.23), for $\beta = 180°$, the conductor screen diffraction coefficient derived from equation (6.19) will substitute the wedge diffraction coefficient in equation (5.22).

To further analyze the NLoS scenarios, with a simple geometrical calculation and based on applicability of equation (5.6), the half-width of transition region (w), distance of receiver antenna from the shadow boundary (h) , and current position of receiver from the 180°-axis (h') depicted in Figure 6.5 and Figure 6.6, can be considered with the goal of unveiling scenarios (specific β angles) that receiver antenna falls into the transition region. This condition correlates to experimental scenarios of $\beta \in [91°, 140°]$ and $\beta \in [220°, 269°]$, which the transition function specified in equation (5.9) has a maximum effect leading to the oscillations observed with the path-loss for $\beta \in [91°, 111°]$ and $\beta \in [249°, 269°]$. The effect of transition function diminutions as the receiver moves away from the shadow boundary and its magnitude approaches unity outside the transition zone for $\beta \in (140°, 220°)$, resulting in an overall smooth path-loss pattern for $\beta \in (111°, 249°)$ as depicted in Figure 6.9. For $\beta \in [91°, 111°]$, an average increase in path-loss is observed, that it can be described in the contexts of transition zone properties. If a reflective object is near the shadow boundary, the signal will experience a $180°$ phase shift and cancel the direct wave at the receiver. If a reflective object is tangent to transition zone, the electromagnetic waved will be shifted because of the increase in path length, undergo an additional $180°$ phase shift due to reflection, and reinforce the direct wave at the receiver. A transition from shadow boundary to the tangential area results in an increase in the wave power. In this experiment, as the torso rotates in an angular motion for $\beta \in [91°, 111°]$, the portion of chest that is positioned near the shadow boundary of transition region, manifest itself as reflective object, and as the torso curvature moves away from the shadow boundary, results in degradation of the path-loss. Using the same analogy, as the torso rotates for $\beta \in [249°, 269°]$ the chest curvature moves toward the shadow boundary, resulting in a growth of path-loss. The measurement data did not reveal such a behavior as those have been conducted at $30°$ intervals. Consequently, the magnitude of $D_{T-Wedge}$ and $D_{T-Screen}$ (diffraction coefficients of wedge and screen models) follow a gradual growth for angles $\beta \in (140°, 180°]$ and a reduction for $\beta \in [180°, 269°)$ and since, they are the dominant parts of path-loss model in equation (5.23), result in an increase of path-loss for $\beta \in (140°, 180°]$ and a degradation path-loss for $\beta \in [180°, 269°)$ respectively.

There are two instances of free space measured path-loss at angle $\beta = 0°$. The one with the smaller path-loss corresponds to the effect of human body when the receiver is mounted on the human chest facing the transmitter.

6.4 Proposed Enhancements to the UTD Model

Potential adjustments can apply to existing wedge model to compensate for oscillations observed with $\beta \in [91°, 111°]$ and$\beta \in [249°, 269°]$. To proceed with that, the effect of reflection waves from the incident plane ($\overline{QP}$ leg in Figure 6.5), correlated to the last term of equation (5.8), can be neglected to better match the model to the geometry of human torso. To be more specific, equation (5.8) , is a derivative of equation (6.20) that is approximation is provided in equation (5.7) [62][73][107] .

$$D_{T-Wedge} = D_1 + D_2 + \Gamma_n D_3 + \Gamma_o D_4 \tag{6.20}$$

Another enhancement to existing path-loss model could be to expand the conductor screen model used for $\beta = 180°$ (depicted in Figure 6.6) across all NLoS $\beta \in (90°, 269°)$ scenarios. To proceed with the proposed enhancement, a small modification to equations (6.10) and (6.11) is employed by adding $\widehat{M}$ from equation (6.6), which implies to overlapping of triangle legs in the wedge to simulate a conductor screen.

$$\varphi' = \begin{cases} \beta - {}^{\pi}/_{2} - \alpha + M, & \beta \in (90°, 180°) \\ {}^{3\pi}/_{2} - \beta - \alpha + M, & \beta \in (180°, 270°) \end{cases} \tag{6.21}$$

$$\varphi = 2\pi - tan^{-1}\left({}^{x}/_{d}\right) \tag{6.22}$$

The proposed enhancements provide a slight growth in the computed path-loss compare to the original wedge and screen models, which is due to deprivation of reflected waves from the incident plane of the wedge model. The path-loss comparison of original model versus the proposed enhancement models is depicted in Figure 6.10. One interesting observation is the fact the wedge model without incident plane and the conductor screen model for $\beta \in (90°, 269°)$ introduces a slightly larger path-loss than original wedge model, which is due to excluding the effect of reflected waves from the incident plane of the wedge-shaped model. Furthermore, for wedge model without the incident plane the path-loss stays intact for $\beta = 180°$ as we had always used a conductor screen model for this scenario.

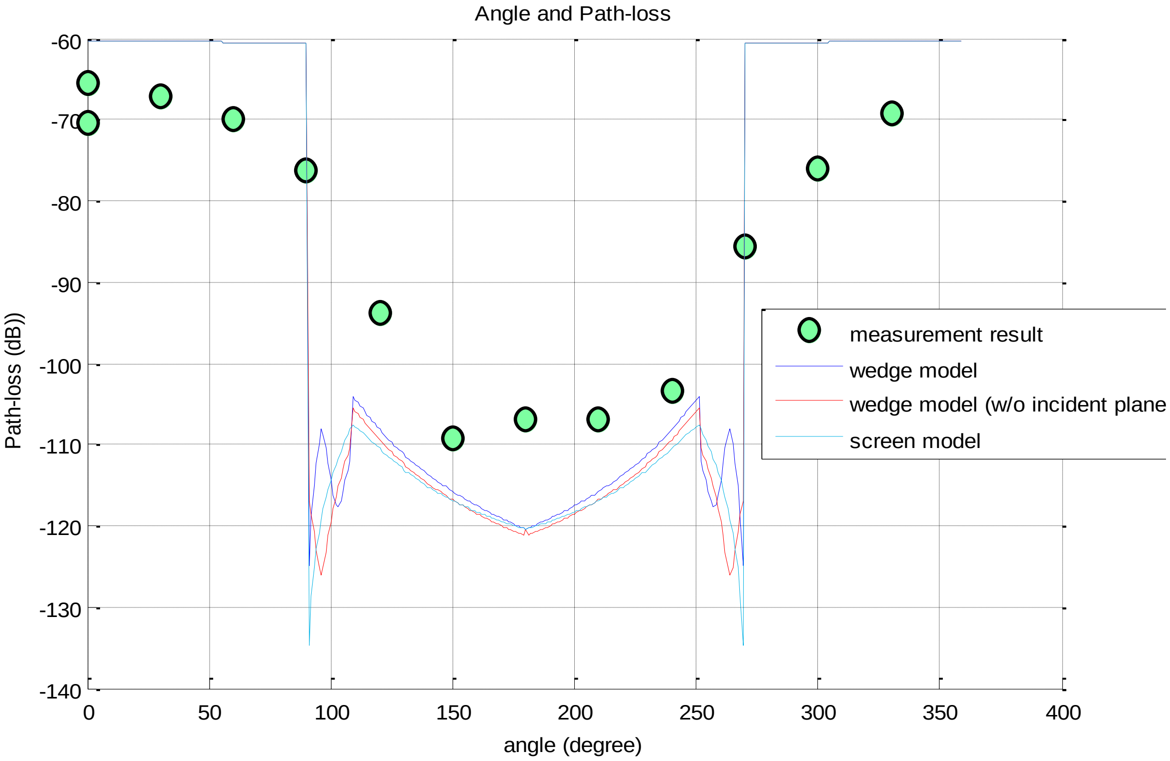

Figure 6.10 Path-loss using three different models.

6.5 Variable Positioning of Transmitter Antenna

The previous sections of this chapter provides discussion on analysis of shortest first-path ToA , DME and path-loss in proximity of human torso in angular motion and for a static positioning of transmitter placed 5 m away from a receiver mounted on the human chest.

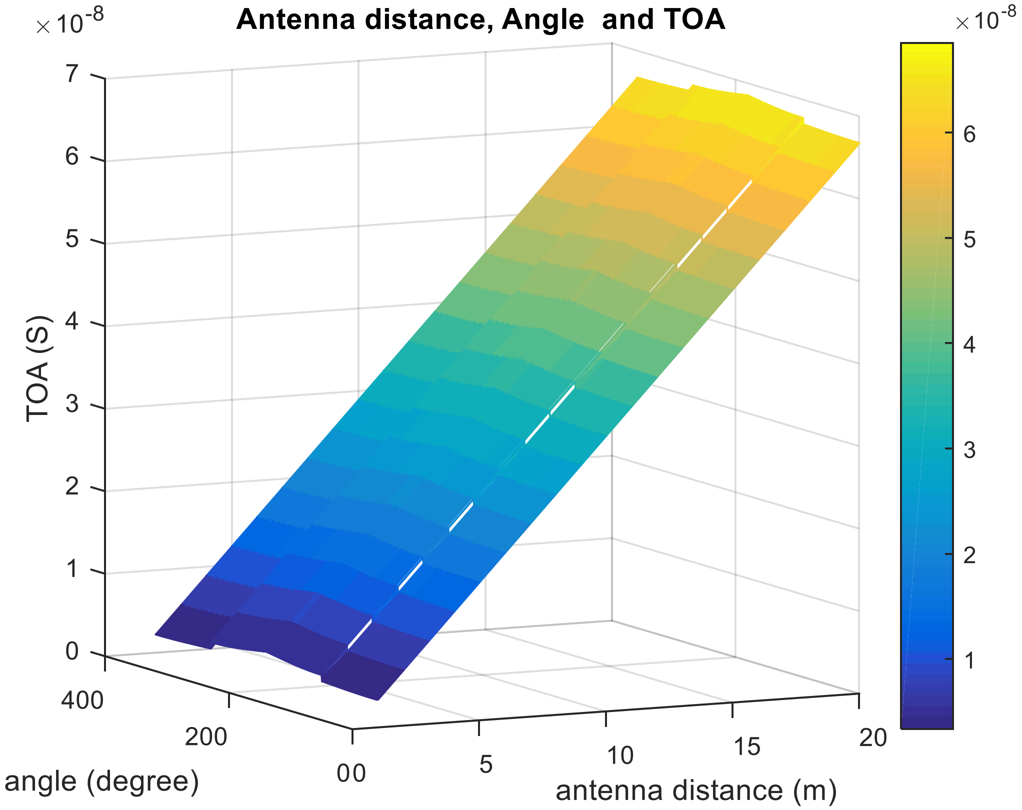

Figure 6.11 Shortest first path ToA; for variable transmitter antenna distance and angular rotational motion of human torso.

In this section, as an expansion to the previous study, variable positioning of transmitter antenna will be investigated, when human torso is in angular motion. Figure 6.11, Figure 6.12 and Figure 6.13 provide an illustration t to this analysis for ToA, DME and path-loss respectively.

Figure 6.11 provides the 3D model depiction of first path ToA in the proximity of a human torso in angular motion for variable positioning of transmitter in respect to the received mounted on human chest. The ToA/angle cross-section of this figure is similar to the 2D first path ToA provided in Figure 6.7 for static positioning of transmitter antenna. Figure 6.11 depicts an average inclination of shortest first path ToA as the distance of transmitter varies from 1 m to 20 m, which is due to an increase in the free space distance of transmitter antenna from the human torso in an angular motion from the equation (6.4). The model can certainly handle transmitter distances beyond 20 m, we are just limiting the computation to 20 m to save one computation time and resources.

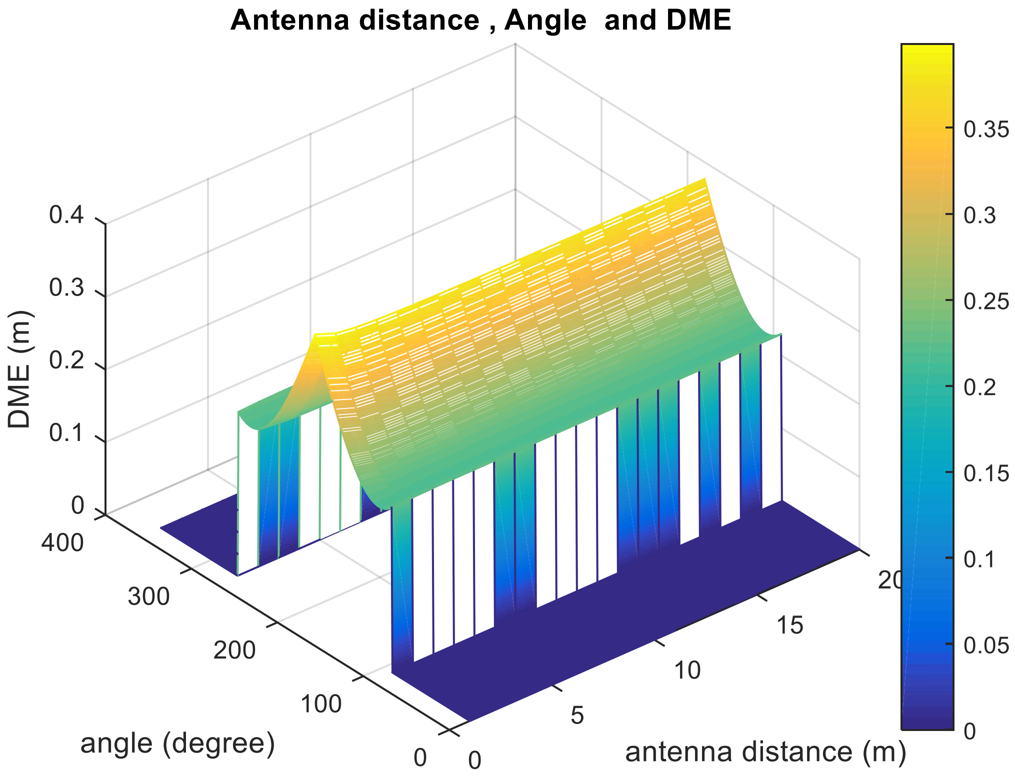

Figure 6.12 Shortest first path DME; for variable transmitter antenna distance and angular rotational motion of human torso.

Figure 6.12 provides the 3D model depiction of first path DME in the proximity of a human torso in angular motion for variable positioning of transmitter in respect to the received mounted on human chest. The DME/angle cross-section of this figure is similar to the 2D first path DME provided in Figure 6.8 for static positioning of transmitter antenna. Figure 6.12 illustrates a degradation of DME behavior of shortest first path as the distance of transmitter move from 1 m to 20 m.

It is understood the DME and effect of diffraction of first path around human body becomes negligible as the distance between transmitter and the torso increases (value of DME approaches zero in Figure 6.12). This aligns with our diffraction discussion in section 2.5.1 and Figure 2.8 , which confirms the DME decreases as the distance between antenna pair increases due to elimination of effect of diffraction around an edge-shaped metallic objects. The model can certainly handle transmitter distances beyond 20 m, we are just limiting the computation to 20 m to save one computation time and resources.

Consequently, Figure 6.13 provides the 3D model depiction of first path path-loss in the proximity of a human torso in angular motion for variable positioning of transmitter in respect to the received mounted on human chest. The Path-loss/angle cross-section of this figure is similar to the 2D first path path-loss provided in Figure 6.9 for static positioning of transmitter antenna. Figure 6.13 depicts a slight degradation of shortest first path path-loss as the distance of transmitter move from 1 m to 20 m, which is due to the free space path-loss between transmitter antenna and the human torso in angular motion from the equation (6.4).

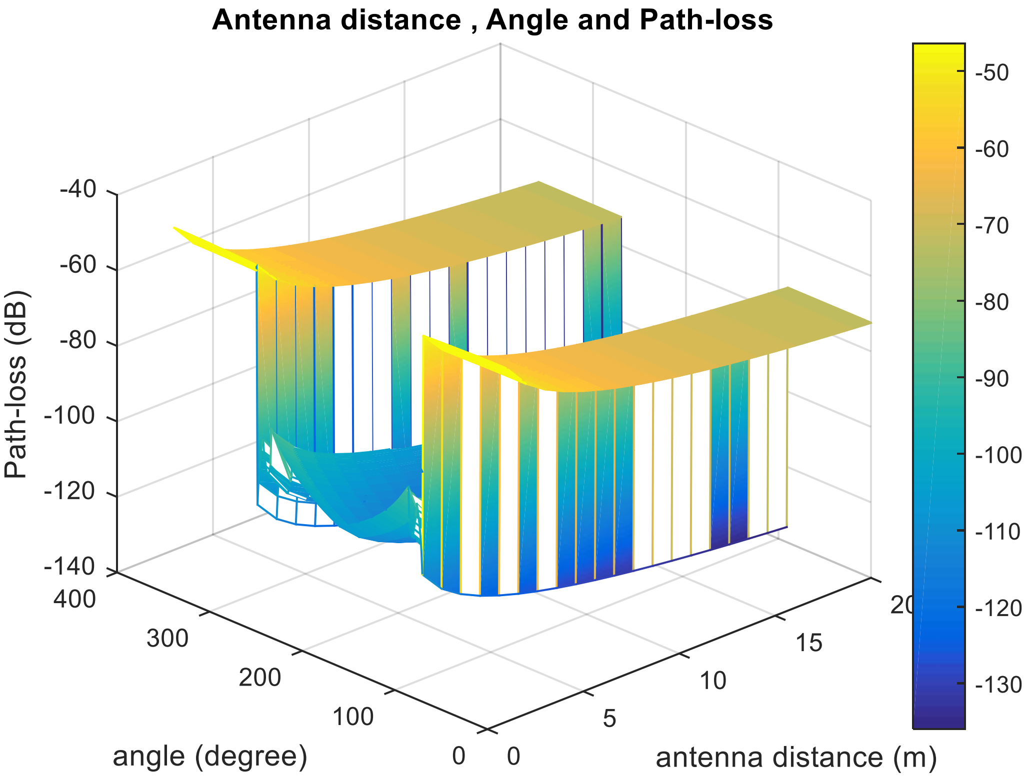

Figure 6.13 Shortest first path path-loss; for variable transmitter antenna distance and angular rotational motion of human torso.

As mentioned before, The model can certainly handle transmitter distances beyond 20 m, we are just limiting the computation to 20 m to save one computation time and resources.

6.6 Summary

We proposed an analytical UTD approach to predict the behavior of shortest diffracted path, known as the first path, for ToA-based indoor localization and accurate ranging for radiation scenario by the human body in an angular motion. This analytical approach is based on the applicability of UTD conductor wedge path-loss model previously used for communication purposes in an urban area, and a custom geometrical ray optics formulation to calculate ToA and DME of the first path. The UTD ray theory of smooth convex surface is applied to the wedge path-loss model in terms of creeping wave diffraction coefficient. The mechanics happens with a comprehensive analysis of EM fields on the surface of torso to help in blending the smooth convex and wedge diffraction coefficients into the wedge path-loss model (an exception to this is using UTD ray theory of conductor screen diffraction coefficient instead of conductor wedge diffraction coefficient for angular motion $\beta = 180^o$). Embedded in the UTD conductor wedge path-loss model, the wedge diffraction encapsulates the transition function, in which its effect in the transition region in the proximity of human torso in angular motion is comprehensively analyzed. The validation scenario entailed static positioning of a transmitter antenna placed 5 m away from a receiver mounted on the human chest in angular rotation. The UWB measurements used to validate manually calculated ToA, DME and path-loss of first path sweeping 3-8 GHz of bandwidth. Two potential adjustments to the proposed model discussed to compensate for path-loss oscillations in transition regions in proximity of human torso. A 3D model was provided based on analytical calculation of first path ToA, DME and path-loss of for various separation of the transmitter antenna from the human body, when torso and the receiver antenna mounted on the chest are in angular motion. The overall solution was proposed as an enhancement to existing RT algorithm.

In the next chapter of this thesis, we discuss the conclusion of the thesis and provide recommendation on the future direction of research conducted in the thesis.

Chapter 7 Conclusions and Future Directions

This chapter provides an overall conclusion and discussion of some possible directions for the research that has been the focus of this dissertation.

To conclude, this thesis provided modeling solutions as a mitigation to the limitation of existing propagation tools and models to computationally capture the effects of micro-metals and human body on ToA-based indoor localization. Solutions for each computational technique were validated by empirical measurements using UWB signals. Related to the two problem areas of ToA-based indoor and human body localization, there were four solutions proposed to the aforementioned problem areas. EM computational method, and a combination of analytical UTD and geometrical procedures offered to model the effects of micro-metals on ToA-based indoor localization. Analytical UTD ray theory and geometrical procedures were used to model the effects of human body on ToA-based human body systems for scattering and radiation scenarios. In particular, FDTD numerical method was used to estimate the ranging errors, and a combination of UTD ray theory and geometrical ray optics properties were utilized to model the path-loss and the ToA of the DP obstructed by micro-metals. Analytical UTD ray theory and geometrical ray optics properties are exploited to model the path-loss and the ToA of the first path obstructed by the human body for the scattering scenarios. The proposed scattering solution expanded to analytically model the path-loss and ToA of the DP obstructed by human body in angular motion for the radiation scenarios.

For future directions, I would like to recommend analysis of effects of bandwidth on the analytical UTD rays theory models introduced in this dissertation, which operate based on center frequency of bandwidth, to estimate the path-loss for the DP obstructed by the micro-metals and the human body. The same approach was previously conducted in the empirical analysis provided by [34][35] in the proximity of human body. A more complex experimental scenarios which encompasses misaligned elevation of antenna pair could be analyzed to understand their effects on the UTD models introduced in the thesis as the models developed throughout this dissertation assume the same height for transmitter and receiver. As part of this effort it is recommended to analyze vertical motion of the human body in addition to the angular motion of torso that is discussed in this dissertation. It is recommended to analyze the effects of different orientation of carrying tag mounted on human body on the proposed UTD models, in the same fashion that [34] has evaluated statistical models for the mounted sensors on the human chest or attached to the wrist.

Lastly, the models introduced in this dissertation operate based upon the assumption the conductivity, permittivity and permeability of human tissues are analogous to a conductor material. It is recommended to analyze the effects of different human tissue type on proposed models in this thesis in the same fashion [108] has analyze effects of absorbent, conductor and dielectric material on proposed UTD model for communication purposes.

Bibliography

[1] Yunxing Ye , “Bounds on RP Cooperative Localization for Video Capsule Endoscopy” , Ph.D. Dissertation, Worcester Polytechnic Institute, May 2013.

[2] Guanqun , Bao , “On Simultaneous Localization and Mapping inside the Human Body (Body-SLAM)” , Ph.D. Dissertation, Worcester Polytechnic Institute, May 2014.

[3] Alavi, Bardia. "Distance measurement error modeling for time-of-arrival based indoor geolocation." PHD Dissertation, Worcester Polytechnic Institute, Worcester: April (2006).

[4] K. Pahlavan and A. H. Levesque, *Wireless Information Networks,* 2nd ed., New York: John Wiley and Sons, 2005.

[5] H. Hatami and K. Pahlavan, “Performance Comparison of RSS and TOA Indoor Geolocation Based on UWB Measurement of Channel Characteristics,” *IEEE International Symposium on Personal, Indoor and Mobile Radio Communications,* September, 2006.

[6] Catovic and Z. Sahinoglu, “The Cramer-Rao Bounds of Hybrid TOA/RSS and TDOA/RSS Location Estimation Schemese,” *IEEE Communication Letters,* vol. 8, no. 10, pp 626-628, October, 2004.

[7] Y. Qi, H. Kobayashi, and H. Suda, “Cramer-Rao Bound for Geolocation in non-line-of-sight Environment,” *IEEE Transactions on Wireless Communications,* vol. 5, no. 3, pp 672-681, March 2006.

[8] S. Gezici et al., “Localization via Ultra-Wideband Radios: A look at Positioning Aspects for Future Sensor Networks,” *IEEE Signal Processing Magazine,* vol. 22, no. 4, pp 70-84, July 2005.

[9] H. Sayed, N. Tarighat, and N. Khajehnouri, “Network-Based Wireless Location: Challenges faced in Developing Techniques Accurate Wireless Location Information,” *IEEE Signal Processing Magazine,* vol. 22, no. 4, pp 24-40, July 2005.

[10] N. Alsindi, X. Li, and K. Pahlavan, “Analysis of Time of Arrival Estimation using Wideband Measurements of Indoor Radio Propagations,” *IEEE Transactions on Instrumentation and Measurement,* vol. 56, no. 5, pp 1537-1545, October 2007.

[11] S. Howard and K. Pahlavan, “Measurement and Analysis of the Indoor Radio Channel in the Frequency Domain,” *IEEE Transactions on Instrumentation and Measurement,* vol. 39, no. 5, pp 751-755, October 1990

[12] T. Holt, K. Pahlavan, and J. F. Lee, “A Graphical Indoor Radio Channel Simulator using 2D Ray Tracing,” *IEEE International Symposium on Personal, Indoor, and Mobile Radio Communications,* pp 411-416, October 1992

[13] G. Yang, K. Pahlavan, and J. F. Lee, “A 3D Propagation Model with Polarization Characteristics, in Indoor Radio Channel,” *IEEE Global Telecommunication conference,* vol. 2, pp 1252-1256, November-December 1993.

[14] N. Alsindi, “Indoor Cooperative Localization for Ultra-Wideband Wireless Sensor Networks” Ph.D. Dissertation, Worcester Polytechnic Institute, 2008.

[15] Yishuang Geng , “Radio Propagation for Localization and Motion Tracking in Three Body Area Network Applications” Ph.D. Dissertation, Worcester Polytechnic Institute, 2016.

[16] Lawton, Michael C., and J. P. McGeehan. "The application of a deterministic ray launching algorithm for the prediction of radio channel characteristics in small-cell environments." *IEEE Transactions on Vehicular Technology* 43.4 (1994): 955-969.

[17] Mametsa, H. J., F. Rouas, A. Berges, and J. Latger. "Imaging radar simulation in realistic environment using shooting and bouncing rays technique." In *Proceedings of SPIE,* vol. 4543, pp. 34-40. 2002.

[18] Henry L. Bertoni, “Radio Propagation for Modern Wireless Systems”, Prentice Hall, Inc. New Jersey, pp.120 – 125 , 1999.

[19] M.Ghaddar, L. Talbi, T. Denidni, A. Charbonneeau, “Human body modeling for prediction of effect of people on indoor propagation channel”, Electronics letters, December 2004, vol.40, No.25.

[20] U. Khan, K. Pahlavan and S. Makarov " Computational Techniques for Wireless Body Area Networks Channel Simulation Using FDTD and FEM" the Proceedings of the 33rd IEEE Annual International Conference of the Engineering in Medicine and Biology Society (EMBC), August 30-September 3, 2011, Boston, MA.

[21] Ansoft H. F. S. S. “ver. 11.” Ansoft Corporation, Pittsburg, PA, July 2007.

[22] Y. Zhao, Y. Hao, A. Alomainy, C. Parini, “UWB On-Body Radio Channel Modeling Using Ray Theory and Sub-band FDTD Method”, IEEE Trans.s on Mic. Theory and Tech., Vol. 54, No.4, April 2006.

[23] F. Askarzadeh, M. Heidari, S.Makarov , K. Pahlavan, “Analysis of Effect of Micro-Metalic Objects on Ranging Errors Using Finite Difference Time Domain Method”, IWCMC, 2008.

[24] F. Askarzadeh, Y. Ye, Kaveh Ghaboosi, S. Makarov, K.Pahlavan, “A New Perspective on the Impact of Diffraction in Proximity of Micro-Metalic for Indoor Geolocation”, PIMRC, 2011.

[25] F. Askarzadeh, Y. Ye, U. Khan, F. O. Akgul, K. Pahlavan, S. N. Makarov, “Computational Methods for Localizations” Chapter for “HANDBOOK of POSITION LOCATION THEORY, PRACTICE, AND ADVANCES”, By S. Zekavat and M. Beuhrer, Wiley Publication , 2012 .

[26] F. Askarzadeh, K. Pahlavan, S. Makarov, Y. Ye, U. Khan "Analyzing the effect of human body and metallic objects for indoor geolocation." *2016 10th International Symposium on Medical Information and Communication Technology (ISMICT)*. IEEE, 2016.

[27] Askarzadeh, Fardad, Kaveh Pahlavan, Sergey Makarov, Yunxing Ye, and Umair Khan. "Analyzing the effect of human body and metallic objects for

indoor geolocation." In *Medical Information and Communication Technology (ISMICT), 2016 10th International Symposium on*, pp. 1-5. IEEE, 2016.

[28] Q. Wang , T. Tayamachi, I. Kimura, J. Wang “An On-body Channel Model for UWB body are communications for various postures”, IEEE Transactions on Antenna and Propagation , 57 (4): 991-998 , 2009.

[29] H. Heidari, F.O. Akgul , K. Pahlavan “ Identification of the absence of direct path in indoor localization systems”, International Journal of Wireless Information Networks , 15 (3-4): 117-127, 2008.

[30] S. Li, Y. Geng, K. Pahlavan, “Analysis of Three-dimensional Maximum Likelihood Algorithm for Capsule Endoscopy Localization,” 5th International Conference on Biomedical Engineering and Informatics (BMEI), 2012.

[31] X. Zheng , G. Bao. The Performance of Simulated Annealing Algorithms for Wi-Fi Localization using Google Indoor Map”, IEEE 76th Vehicular Technology Conference (VTC) , 2012.

[32] K. Pahlavan , Li Xinrong , J.P. Makela “Indoor Geolocation Science and Technology” , IEEE Communication Magazine , 40(1):112 – 118, 2002.

[33] Y. Geng, J. Chen, K. Pahlavan, “Motion Detection Using RF Signals for the First Response in Emergency Operations: A Phasor Project.”, IEEE 21nd International Symposium on Personal Indoor and Mobile Radio Communication (PIMRC), 2013.

[34] Yishuang G., Jie He, Kaveh P., “Modeling of Effect of Human Body on TOA Based Indoor Human Tracking”, Int J Wireless Inf Net., 2013.

[35] Geng, Yishuang, and Haokun Deng. "Modeling the effect of human body on TOA ranging for indoor human tracking with wrist mounted sensor." In *Wireless Personal Multimedia Communications (WPMC), 2013 16th International Symposium on*, pp. 1-6. IEEE, 2013.

[36] Geng, Yishuang, Yadong Wan, Jie He, and Kaveh Pahlavan. "An empirical channel model for the effect of human body on ray tracing." In *Personal Indoor*

and Mobile Radio Communications (PIMRC), 2013 IEEE 24th International Symposium on, pp. 47-52. IEEE, 2013.

[37] Jin Chen, Yunxing Ye, Kaveh Pahlavan, “UWB Characteristics of Creeping Wave for RF Localization around the Human Body”, IEEE *23rd Int. Symp. on Pers.,Ind. and Mobile Radio Comm – (PIMRC), 2012*

[38] B. Alavi, K. Pahlavan, X. Li, and N. Alsindi, “Indoor Geolocation Distance Error Modeling With UWB Technology,” in *Proceedings of IASTED 2nd International Conference on Communication and computer networks CCN 2004*, November 2004.

[39] Kamya Yekeh Yazdandoost, Kamran Sayrafian-Pour, Wen-Bin Yang, John Hagedorn and Judith Terrill, “*A Statistical Path Loss Model for Medical Implant Communication Channels”*, IEEE 20th Int Symposium on Personal, Indoor and Mobile Radio Comm. , 2009.

[40] Takahiro Aoyagi, Jun-ichiTakada, Kenichi Takizawa, Norihiko Katayama, TakehikoKobayashi, Kamya Yekeh Yazdandoost, Huan-bang Li and Ryuji Kohno, *Channel models for wearable and implantable WBANs*, July 2008.

[41] Umair I. Khan, “Computational Techniques for Comparative Performance Evaluation of RF Localization inside the Human Body”, MS Thesis, Worcester Polytechnic Institute, 2011.

[42] J. Lee, C. Kim, D. Ha, S. Sangodoyin, R. Dong, “UWB Propagation Measurements in BAN Scenario”,8th IEEE, IET Int. Symposium on Communication Systems, Networks and Digital Signal Processing,2012.

[43] Spencer, Quentin H., Brian D. Jeffs, Michael A. Jensen, and A. Lee Swindlehurst. "Modeling the statistical time and angle of arrival characteristics of an indoor multipath channel." *IEEE Journal on Selected areas in communications* 18, no. 3 (2000): 347-360.

[44] Molisch, Andreas F., Jeffrey R. Foerster, and Marcus Pendergrass. "Channel models for ultrawideband personal area networks." *IEEE wireless communications* 10, no. 6 (2003): 14-21.

[45] T. S. Rappaport, *Wireless Communications:Principles and Practice*, 2nd ed., Prentice Hall, Upper Saddle River, NJ, 2002

[46] M. Ghavami, L. B. Michael, and R. Kohno, *Ultra-wideband Signals and Systems in Communication Engineering*, Wiley, Hoboken, NJ, 2004.

[47] I. Oppermann, M. Hamalainen, and J. Iinatti, *UWB Theory and Applications*, Wiley, Hoboken, NJ, 2004.

[48] D. Porcino and W. Hirt, "Ultra-wideband radio technology: potential and challenges ahead," *IEEE Communications Magazine*, Vol. 41, No. 7, July 2003, pp. 66 - 74.

[49] N. Alsindi, "Indoor Cooperative Localization for Ultra-Wideband Wireless Sensors Networks," Ph.D. Dissertation, Worcester Polytechnic Institute, 2008.

[50] Ferit Ozan Akgul, "Modeling the behavior of Multipath Components Pertinent to Indoor Geolocation" Ph.D. Dissertation, Worcester Polytechnic Institute, 2010.

[51] Pahlavan, Kaveh, and Prashant Krishnamurthy. *Networking fundamentals: wide, local and personal area communications*. John Wiley & Sons, 2009.

[52] Yunxing Ye, Umair Khan, Kaveh Pahlavan, "Accuracy Bounds of RSS and TOA based RF localization in capsule endoscopy" the Proceeding of 33rd IEEE Annual International Conference of Engineering in Medicine and Biology Society (EMBC), 2011,August.

[53] Y. Ye, U.Khan, N. Alsindi, Rujun Fu, K.Pahlavan, "On the Accuracy of RF positioning in multi-Capsule Endoscopy", 22nd IEEE Int Symp. on Personal, Indoor and Mobile Radio Comm.(PIMRC), 2011,September.

[54] Pranay Swar, Yunxing Ye, Kaveh Ghaboosi, Kaveh Pahlavan, "On Effect of Transmit Power Variance on Localization Accuracy in Wireless Capsule Endoscopy", Proc. of the IEEE WCNC, 2012, April.

[55] Ye, Yunxing, Pranay Swar, Kaveh Pahlavan, and Kaveh Ghaboosi. "Accuracy of rss-based rf localization in multi-capsule endoscopy." *International Journal of Wireless Information Networks* 19, no. 3 (2012): 229-238.

[56] K. Pahlavan, P. Krishnamurthy and J. Beneat, Wideband radio channel modeling for indoor geolocation applications, IEEE Communication. Mag., 36(4), 60-65(1998).

[57] B. Alavi, K. Pahlavan, N. Alsindi, and X. Li, "Using UWB Measurements for Statistical Analysis of the Ranging Error in Indoor Multipath Environment," accepted for publication in *International Journal of Wireless and Optical Communications (IJWOC)*, 2006.

[58] B. Alavi and K. Pahlavan, Modeling of the TOA based Distance Measurement Error Using UWB Indoor Radio Measurements, *IEEE Communication Letters*, Vol. 10, No. 4, pp: 275-277, April 2006. X. Li and K. Pahlavan, Super-resolution TOA estimation with diversity for indoor geolocation, IEEE Trans. Wireless Communication., December. 2003.

[59] C. A. Balanis, *Advanced Engineering Electromagnetics*, John Wiley & Sons, 1999..

[60] Keller, Joseph B. "Rays, Waves and Asymptotics1." *Classical and Modern Diffraction Theory* (2016): 67.

[61] Coulson, John, G. G. Becknell, N. G. Van Kampen, R. N. Buchal, J. B. Keller, Robert G. Kouyoumjian, Prabhakar H. Pathak et al. "Foundations of Modern Diffraction Theory." In *Classical and Modern Diffraction Theory*, pp. 213-301. Society of Exploration Geophysicists, 2016.

[62] Kouyoumjian, R. G., and P. H. Pathak. "A uniform GTD approach to EM scattering and radiation." *Low and High Frequency Asymptotics: Acoustic, Electromagnetic and Elastic Wave Scattering* (2013): 265.

[63] J. Ryckaert, P. De Doncker, R. Meys, A. de Le Hoye and S. Donnay, "Channel model for wireless communication around human body", in Electronic Letter, April 2004, Vol 40, No 9

[64] R. Chaves-Santiago, K. Sayrafian, A. Khaleghi, K. Takizawa, J. Wang, I. Balasingham, H. Li “ Propagation models for IEEE 802.15.6 standardization for implant communication in body area net-works”, IEEE Communications Magazine, 51(8):80-87,2013.

[65] S. S. Ghasemzadeh, R. Jana , C. W. Rice, W. Turin and V. Tarokh “Measurement and Modeling of an Ultra-wide Bandwidth Indoor Channel”, IEEE Transaction on Communication , Vol. 52, no.10, pp.1786-1796, Oct. 2004.

[66] C.C. Chong, S.K. Yong, “A Generic Statistical-based UWB Channel Model for High-rise Apartments”, IEEE Transaction on Antenna and Propagation, Vol. 53, no. 8, pp. 2389-2399 , Aug. 2005.

[67] Rylander, Thomas, Pär Ingelström, and Anders Bondeson. *Computational electromagnetics*. Springer Science & Business Media, 2012.

[68] Sadiku, Matthew NO. *Numerical techniques in electromagnetics with MATLAB*. CRC press, 2011.

[69] Jin, Jian-Ming. *The finite element method in electromagnetics*. John Wiley & Sons, 2015.

[70] Baker, Bevan B., and Edward Thomas Copson. *The mathematical theory of Huygens' principle*. Vol. 329. American Mathematical Soc., 2003.

[71] L. B. Felsen, Leopold B., and Nathan Marcuvitz. *Radiation and scattering of waves*. Vol. 31. John Wiley & Sons, 1994.

[72] Born, Max, and Emil Wolf. *Principles of optics: electromagnetic theory of propagation, interference and diffraction of light*. Elsevier, 2013.

[73] Henry L. Bertoni, “Radio Propagation for Modern Wireless Systems”, Prentice Hall, Inc. New Jersey, pp 189-194, 1999.

[74] Hall, Peter S., and Yang Hao. "Antennas and propagation for body centric communications." In *Antennas and Propagation, 2006. EuCAP 2006. First European Conference on*, pp. 1-7. IEEE, 2006.

[75] Nadeem, Adnan, Muhammad Azhar Hussain, Obaidullah Owais, Abdul Salam, Sarwat Iqbal, and Kamran Ahsan. "Application specific study, analysis and classification of body area wireless sensor network applications." *Computer Networks* 83 (2015): 363-380.

[76] Werner, Douglas H., and Zhi Hao Jiang, eds. *Electromagnetics of Body Area Networks: Antennas, Propagation, and RF Systems*. John Wiley & Sons, 2016.

[77] Cavallari, Riccardo, Flavia Martelli, Ramona Rosini, Chiara Buratti, and Roberto Verdone. "A survey on wireless body area networks: Technologies and design challenges." *IEEE Communications Surveys & Tutorials* 16, no. 3 (2014): 1635-1657.

[78] Movassaghi, Samaneh, Mehran Abolhasan, Justin Lipman, David Smith, and Abbas Jamalipour. "Wireless body area networks: A survey." *IEEE Communications Surveys & Tutorials* 16, no. 3 (2014): 1658-1686

[79] Hu, Bin, Guo-Ping Gao, Le-Le He, Xiao-Dong Cong, and Jin-Ning Zhao. "Bending and on-arm effects on a wearable antenna for 2.45 GHz body area network." *IEEE Antennas and Wireless Propagation Letters* 15 (2016): 378-381.

[80] D. A. McNamara, C. W. I. Pistorius, and J. A. G. Malherbee, “Introduction to the Uniform Geometrical Theory of Diffraction”, Artech House, Norwood, Mass., Chap.8. 1990.

[81] Jakobus, U., and F. M. Landstorfer. "Application of Fock currents for curved convex surfaces within the framework of a current-based hybrid method." In *Computation in Electromagnetics, Third International Conference on (Conf. Publ. No. 420)*, pp. 415-420. IET, 1996.

[82] Wait, James R. *Electromagnetic Waves in Stratified Media: Revised Edition Including Supplemented Material*. Vol. 3. Elsevier, 2013.

.

[83] Rousseau, Paul R., Prabhakar H. Pathak and Hsi-Tseng Chou. "A time domain formulation of the uniform geometrical theory of diffraction for scattering from a smooth convex surface." *IEEE Transactions on Antennas and Propagation* 55, no. 6 (2007): 1522-1534.

[84] G. Koutitas, C. Tzaras, "A UTD Solution for Multiple Rounded Surfaces", IEEE Trans.on Antenna and Prop., Vol. 54, No.4, April 2006.

[85] E. M. A. Oliveira, Tao Li, V. Iyer, and S. Makarov, "A 2D FDTD/MoM Simulator in MATLAB and Its Applications," *2008 Antenna Applications Symposium Proc.*, Monticello, IL, Sep. 2008.

[86] Makarov, Sergey N. Sergey N. *Antenna and EM Modeling with MATLAB*. Wiley-Interscience,, 2002.

[87] Yee, Kane S., and Jei S. Chen. "The finite-difference time-domain (FDTD) and the finite-volume time-domain (FVTD) methods in solving Maxwell's equations." *IEEE Transactions on Antennas and Propagation* 45, no. 3 (1997): 354-363.

[88] A. Taflove, *Computational Electrodynamics, The Finite Difference Time Domain Approach*, Artech House, Norwood, MA, 2001, second ed.

[89] Henry Bertoni, "09MoreDiff.pdf" http://eeweb.poly.edu/faculty/bertoni/docs/ September 2003.

[90] Henry Bertoni, "08Diffraction.pdf" http://eeweb.poly.edu/faculty/bertoni/docs/ September 2003.

[91] Henry Bertoni, "12Terrain&Veg.pdf" http://eeweb.poly.edu/faculty/bertoni/docs/ September 2003

[92] Andersen, J. Bach. "UTD multiple-edge transition zone diffraction." *IEEE Transactions on Antennas and Propagation* 45, no. 7 (1997): 1093-1097.

[93] Mudhafar Hassan-Ali , "Using Ray-Tracing Techniques in Site-Specific Statistical Modeling of Indoor Radio Channels" , Ph.D. Dissertation, Worcester Polytechnic Institute, April 1998.

[94] Ganning Yang, “Performance Evaluation of High Speed Wireless Data Systems Using a 3D Ray Tracing Algorithm”, Ph.D. Dissertation, Worcester Polytechnic Institute, June 1994.

[95] McCormick, Michael E., and David RB Kraemer. "Polynomial approximations for Fresnel integrals in diffraction analysis." *Coastal Engineering* 44, no. 3 (2002): 261-266.

[96] Mielenz, Klaus D. "Computation of Fresnel integrals. II." *Journal of research of the National Institute of Standards and Technology* 105, no. 4 (2000): 589.

[97] Robert Paknys, “Uniform Asymptoptic Formulas for Creeping Wave Field On or Off a Cylinder” , IEEE Transaction on antenna and propagation , Vol 41, No 8. Aug.1993.

[98] R.Paknys, “On the accuracy of the UTD for the Scattering by the Cylinder”,IEEE transactions on Antenna and Propagation , Vol. 42, No. 5, May 1994.

[99] T. Alves, B.t Poussot, J. Laheurte, “Analytical Propagation Modeling of BAN Channels Based on the Creeping-Wave Theory”, IEEE Transaction on antenna and propagation, vol.59,no.4, April 2011.

[100] Zasowski, Thomas, Gabriel Meyer, Frank Althaus, and Armin Wittneben. "UWB signal propagation at the human head." *IEEE Transactions on Microwave Theory and Techniques* 54, no. 4 (2006): 1836-1845.

[101] J. R. Wait, “The ancient and modern history of EM ground-wave propagation” , IEEE Ant. Prop. Mag.,Vol 40, no.5, pp.7-24, Oct 1998.

[102] G. Koutitas, “Multiple Human Effect in Body Area Network”, IEEE Antennas and Wireless Propagation Letters, Vol.9 ,2010.

[103] Holmes, Mark H. *Introduction to perturbation methods*. Vol. 20. Springer Science & Business Media, 2012.

[104] Ancey, S., A. Folacci, and P. Gabrielli. "Exponentially improved asymptotic expansions for resonances of an elliptic cylinder." *Journal of Physics A: Mathematical and General* 33, no. 16 (2000): 3179.

[105] Wang, Ting, Masahiro Umehira, Hiroyuki Otsu, Shigeki Takeda, Teruyuki Miyajima, and Kenichi Kagoshima. "A twin cylinder model for moving human body shadowing in 60GHz WLAN." In *Communications (APCC), 2015 21st Asia-Pacific Conference on*, pp. 188-192. IEEE, 2015.

[106] Mavridis, Theodoros, Luca Petrillo, Julien Sarrazin, David Lautru, Aziz Benlarbi-Delai, and Philippe De Doncker. "Creeping wave model of diffraction of an obliquely incident plane wave by a circular cylinder at 60 GHz." *IEEE transactions on antennas and propagation* 62, no. 3 (2014): 1372-1377.

[107] Schneider, Michael, and Raymond J. Luebbers. "A general, uniform double wedge diffraction coefficient." *IEEE Transactions on Antennas and Propagation* 39, no. 1 (1991): 8-14.

[108] A. D. C. de Queiroz , L. C. Trintinalia, " An analysis of human body shadowing models for ray-tracing radio channel characterization" , SBMO/IEEE MTT-S International Microwave and Optoelectronics Conference (IMOC), 2015.

[109] T. Wang, M. Umehira, H. Otsu, S. Takeda, T. Miyajima, K. Kagoshima, "A Twin Cylinder Model for Moving Human Body Shadowing in 60GHz WLAN", 21st Asia-Pacific Conference on Communications (APCC) , 2015.

[110] Z. Junhui, L. Xu , "Characteristics of the 60 GHz indoor wireless propagation based on ray tracing with human body movement" , 9th International Conference on Communications and Networking in China, 2014.